MODELING AND CONTROL OF PHYSICAL HUMAN-ROBOT INTERACTIONS WITH APPLICATIONS TO ASSISTIVE ROBOTS FOR CONSTRUCTION WORKERS

By

SIYU CHEN

A dissertation submitted to the

School of Graduate Studies

Rutgers, The State University of New Jersey

In partial fulfillment of the requirements

For the degree of

Doctor of Philosophy

Graduate Program in Mechanical and Aerospace Engineering

Written under the direction of

Jingang Yi

And approved by

_____

_____

_____

_____

_____

New Brunswick, New Jersey
January, 2022

© 2022

Siyu Chen

ALL RIGHTS RESERVED

ABSTRACT OF THE DISSERTATION

Modeling and Control of Physical Human-robot Interactions with Applications to Assistive Robots for Construction Workers

by SIYU CHEN

Dissertation Director:

Jingang Yi

The construction industry is one of the highest-risk private sectors in the US, contributing to 21.6% of all work related fatal injuries in 2019. Work-related musculoskeletal disorders (WMSDs) are among the most prevalent occupational health problems affecting manual work in construction industry. Construction workers (e.g., bricklayers and roofers) are frequently exposed to high physical risk hazard, such as repetitive motions (lifting/lowering), awkward postures and lifting weights, and this work environment potentially causes WMSDs. Additionally, construction workers often carry or handle heavy objects/materials and these manual work can potentially cause injuries and back pains. Construction workers also regularly perform tasks with locomotion and gaits that include walking, repetitive kneeling down and standing up on level or inclined

surfaces. For example, roofing leads among construction trades in fatal injuries and has the fourth-highest fatal work injury rate among all occupations. Assist robotic device is deemed as a useful tool to help workers generate the target motions in certain tasks. The main goal of this dissertation is to develop new robotics and automation technologies that can potentially reduce and alleviate WMSDs for construction workers. To achieve the goal, we need to understand the human muscular and postural model, and design robot control system to provide necessary assistance to finish physical tasks in human-robot interactions for construction workers. The topics of this dissertation try to focus on two types of physical human robot interactions in construction: one is the use of robotic manipulator for upper limb assistance and the second for wearable sensor and robot for human walking assistance.

The first part of this dissertation mainly focuses on human-manipulator interaction and presents an assist-as-needed framework to control robotic manipulators. Collaborative robotic manipulators are used to assisting human workers in performing physically intensive tasks. Robotic manipulators augment human upper limb capability (e.g., strength and accuracy), provide necessary assistive forces and help humans perform certain tasks (e.g., move or lift weights and weighted tools). Assist-as-needed control is one of the main concepts to design assistive robotic systems in human-robot interactions. One basic requirement in designing assist-as-needed controllers is the knowledge of human physical strength capacity (e.g., the maximum limb forces) to achieve the desired locomotion. With proper human strength capacity estimation, we design a controller for robotic assistance under changing environments and external disturbances. We take advantage of the muscle synergy model and estimate human physical strength and effort without using electromyography (EMG) sensors. Muscle synergy represents a group of relationship-fixed muscle activities during a particular human limb motion. Human limb motions and their forceful interactions with the environment can be captured as sets of muscle synergy combinations. With these estimations, we design a muscle synergy-

based robotic controller to assist human motion and reject unknown disturbance. The control robustness performance and effectiveness of disturbance rejection are demonstrated through extensive experiments that are performed by multiple human subjects.

The second half of this dissertation mainly focuses on human kneeling and walking gaits and the development of a wearable exoskeleton system to assist construction workers during kneeling tasks. It is critical to model and analyze human performance for kneeling, standing and walking on level and sloped surfaces to understand and capture musculoskeletal injury risks of construction workers. We conduct a human postural balance study on standing and kneeling gaits on inclined and high elevated surfaces. To simulate the high elevation, an immersive mixed reality environment is built with an actual inclined roof surface to create somatosensory haptic feedback. We quantify and model postural balance during kneeling and standing through measurements of the center of pressure and sway motion of the upper body under various inclined angles and heights. A mathematical model is also developed to help understand the experimental results and also to provide design guidance for the prevention and mitigation of the fall risk for construction workers. These developments are validated and demonstrated by experiments.

Based on human model during standing and kneeling, a lightweight, wearable sensing and knee assistive device is developed for construction workers during kneeling and standing tasks. Wearable assistive knee exoskeleton provides an enabling tool to reduce and alleviate WMSD risks for construction workers when performing kneeling tasks on level and sloped surfaces. Analysis of kneeling on level and sloped surfaces is performed for single- and double-leg kneeling tasks and extensive experimental results demonstrate the feasibility of using wearable assistive devices to reduce knee contact loads and muscle activations during kneeling tasks. Human subject testing results validated the devices' effectiveness in reducing muscle activity and knee contact pressure when performing kneeling tasks.

Finally, a real-time gait detection and pose estimation method is developed to monitor workers' walking gaits on level and sloped surfaces. We propose a single wearable inertial measurement unit (IMU)-based walk gait detection and pose estimation method for human subjects on level and sloped surfaces. The gait detection algorithm is based on a recurrent neural networks and its outcome is then used in the full-body pose estimation. Due to the periodic nature of biped walking gaits, a learned Gaussian process dynamic model (GPDM) and a phase variable that parameterizes the GPMD model are used to predict human arm and leg joint angles in real-time. Extensive experiments of different walking patterns and speeds on level and sloped surfaces are conducted to validate and demonstrate the design.

Acknowledgments

My deep and sincere gratitude goes to my Ph.D. advisor Professor Jingang Yi. I'm always impressed by his profound knowledge, insightful visions and enthusiasm on the research work. I would thank Professor Yi for inspiring me to explore the unknowns and supporting me to develop new ideas. I cannot finish this dissertation without his help.

I would like to thank my dissertation committee members: Professor Qingze Zou, Professor Haym Benaroya, Professor Hao Su and Professor Mitja Trkov for their valuable feedback to my work. Special thanks go to Professor Mitja Trkov for his valuable ideas and his support in my experimental studies and research projects.

I also want to thank my colleagues, Dr. Kuo Chen, Tarik Yigit, Yongbin Gong, Marko Mihalec, Kyle Hunte, Merrill Edmonds, Dr. Kaiyan Yu, Dr. Pengcheng Wang, Dr. Fei Liu, Jiaxing Yu, Chaoke Guo, Dr. Aliasghar Arab for providing valuable help and suggestions in my research. In addition, I would like to thank all my friends at Rutgers for the wonderful time that we spent together.

I would like to express my love to my wife, Wenyan Wu, and to my daughter, Alina Chen. I thank them for always being with me and supporting me. This dissertation would not be possible without their endless support. Last but not least, my deepest love goes to my parents for their unconditional love, support and encouragement.

Dedication

To my wife, my daughter and my parents.

Table of Contents

List of Tables

List of Figures

Chapter 1

Introduction

1.1 Background and Motivations

Construction industry is one of the highest-risk private sectors in the US, contributing for 21.6% of the fatal injuries in all industry in 2019 [1]. For the construction workers, work-related musculoskeletal disorders (WMSDs) are among the most prevalent occupational health problems [2]. Construction workers perform repetitive motions frequently, such as lifting, walking, standing and kneeling. They are also exposed to high risk physical activities such as awkward postures and weights lifting, which could potentially lead to WMSDs. Construction workers also regularly perform repetitive kneeling down and standing up motions on inclined surfaces. Roofers perform more than 66% of their work in kneeling, crouching, stooping, crawling postures at high elevation and inclined surface [3]. Among construction trades, roofing leads in fatal injuries and has the fourth-highest fatal work injury rate among all occupations [4]. Occupational activities such as kneeling and squatting are associated with an increase in knee pain, knee injuries and knee osteoarthritis [5]. Robotics and automation technologies are promising tools for assisting human workers in construction activities. To enable robotic assistance for many above-mentioned manual work, it is critical to understand and model human upper limb strength and estimate its performance during routine lifting of heavy tools for construction workers. It is also important to understand and develop models for kneeling, standing and walking during construction activities for roofers. Finally, light-weight, flexible wearable sensors and assistive devices should be developed to integrate with the

human activity recognition and gait estimation schemes.

Human modeling is one of the key factors in estimating human performance and designing assistive devices during human-robot interactions to reduce WMSD risks for construction workers. As human behavior is inherently complex, simplified representations of human model are essential to the success of applying the models to construction applications. There are many approaches to modeling the human performance. Muscle synergy model is used as an enabling tool for estimating human limb force [6] and it has the potential to model forceful interactions between human upper limb and robots. Dynamic models of human movement are proved to be extraordinarily useful for studying human musculoskeletal system, understanding neural circuits, and simulating humanoid balancing movements. Gaussian process dynamic model (GPDM) is used to construct human motion manifold [7], then used to estimate whole body human motion. These physics-based human movement analysis methods provide critical guidance in designing control system for human-robot interactions. Sensing systems are usually designed to capture the performance of human movement, such as using motion capture system, virtual reality system or human-in-the-loop robotic system.

With the knowledge of human models, we can design robotic assistive device system to assist human finish construction tasks. Many of these tasks are involved with physical human-robot interactions. Physical human-robot interaction is one of the most challenging topics in robotic research. Physical human-robot interaction discusses what happens when humans and robots share the same workspace and come into contact with one another [8]. Enhancing the performance and extending the capabilities of human in the physical human-robot interaction systems are critical for deploying useful robotic systems for construction work. Based on human capability, robotic systems are designed and developed, which render compliant behavior with human, plan motions with human preferences and generate interactions along with human intentions. However, research into these topics, especially in terms of theory and implementations for the modeling

and control of these interactions, is sparse due to the complexity of human systems and their dynamic interactions with environment.

In this dissertation, we cover several emerging topics in robotics and automation with applications to construction industry. The development of these topics are aimed to advance the robotics and automation technologies to reduce WMSDs in the common construction activities. The topics of this dissertation include human strength capacity estimation of human upper limbs, muscle synergy-based control of human-manipulator interactions, a human postural balancing model for kneeling gaits, control of a wearable device, and machine learning based walking gait estimation in real-time. These topics center around the two main areas: one in robot-assisted human upper-limb manual work and the other related to human activity and gait estimation and wearable sensing and assistive devices for human lower-limb walk in construction. The main goal of this dissertation is to develop engineering approaches that would lead to reducing and alleviating WMSDs for construction workers. More specifically, the dissertation focuses on: (i) analyzing and modeling human performance during different activities for construction workers, (ii) develop human performance estimation and prediction algorithms based on human models, and (iii) design and develop control system of assistive device in human-robot interactions. In the following section, we will give a brief review for each of the above-mentioned topics.

1.2 Physical Human-robot Interaction Systems in Construction

1.2.1 Human-Manipulator Interactions based on Muscle Synergy Model

Construction workers regularly lift and handle heavy tools, which are the potential major causes of WMSDs. Assistive robotic manipulators can provide necessary assistance to construction workers and have the potential to reduce WMSD risks. Assist-as-needed control is one of main concepts to design assistive robotic systems [9]. The amount of assistance needed is commonly calculated as the capability gap between what is needed

to achieve the required task and human intention or capability [10]. To achieve proper assistance in human-manipulator interaction tasks, it is desirable to obtain human force and intention motion. To estimate human force, one direct way is to build limb muscle model and use the model to analyze the force generation. Various approaches were proposed to identify muscle model such as optimization method [11] and adaptive neural network [12]. However, human force estimation in human-manipulator interaction applications are not presented in the above-mentioned work. Muscle synergy represents a group of relationship-fixed muscle activities during a particular human limb motion, and it has the potential to be used to estimate human upper limb force [13, 14, 15, 16]. Electromyography (EMG) measurements are commonly used to construct muscle synergies [13]. However, wearing EMG probes to monitor muscle activities in the human-robot interactions is not convenient. In this dissertation, we take advantages of the physical human-robot interactions and use interaction forces information to identify these muscle synergies without using EMG.

For human intention motion estimation, neural networks method is particularly suitable due to its capability to handle highly uncertain and nonlinear system [17]. The neural network design can be combined with muscle synergy model [18] and accurately predict interaction force during human-robot interaction. Based on the knowledge of muscle synergy model, a robust control system for human-manipulator interactions can be developed to further assist construction workers with human-manipulator interaction tasks. Impedance/admittance control [19, 20] and learning control [21] are among the most popular control designs for physical human-robot interactions in recent years. The manipulator controller should also be robust to the changing environment and have the ability to reject known disturbances. A combined feed-forward and compensatory control was designed in [22] to achieve disturbance rejection. However, the external disturbance forms are usually unknown and the approaches in the above-mentioned studies cannot be applied directly. In this dissertation, we focus on the human force estimation

using muscle synergy model and control system design for disturbance rejection in the human-manipulator interactions.

1.2.2 Human Postural Balancing in Kneeling Gaits

Construction workers regularly stand and kneel down at high elevation and inclined surfaces [3]. Investigating human balancing performance in different construction scene is critical in preventing and mitigating fall risks, as well as in reducing WMSD risks.

Although study of human quiet stance has been reported extensively (e.g., [23, 24]), limited research exist on postural control of kneeling gaits on elevated or inclined surfaces. In [25], quiet kneeling was studied and compared with the stance with eye-open and eye-closed. Center of pressure (COP) motion and power spectral density (PSD) were used as a means to identify the difference between kneeling and stance gaits. The results in [25] concluded that PSD under kneeling showed significant difference with stance and visual feedback plays a significant role on the COP motion under kneeling gaits. However, neither elevation nor inclined kneeling surface was considered.

The study in [26] reported human stance postural balancing on elevated and inclined surface. Human subject experiments were conducted in real environment and the elevation is only 61 cm above the ground. Virtual reality (VR) was a useful tool to generate high elevation environment and it is a popular tool to study human behaviors in elevation [27]. There are minimal difference among the experimental results in studying height difference for human balancing between real and VR environments. Virtual reality becomes an emerging technology for construction safety and trade skills training [27, 28]. Comparing with the kneeling studies in [25], we mainly focus on the influence of elevation and inclined surfaces on balance performance in this dissertation. The outcomes of this work would potentially provide guidance to further design knee or hip robotic assistive intervention for kneeling gaits [29, 30, 31, 32].

1.2.3 Wearable Knee Assistive Devices for Kneeling Gaits

Construction workers regularly perform tasks such as repetitive kneeling down and prolonged stationary kneeling, especially on inclined surfaces. Roofers, HVAC mechanics and concrete workers perform more than 66% of their work in kneeling, crouching, stooping, or crawling postures or gaits [3]. Occupational activities such as kneeling and squatting are associated with increase in knee pain, knee injuries and knee osteoarthritis (KOA) [5]. KOA among workforce is a significant concern and socioeconomic burden. For example, in 2013 the US medical expenditures attributable to osteoarthritis were $139.8 billion [33] with KOA as the highest incidence that are likely to increase due to obesity and aging of population [34]. Wearable knee assistive devices have the potentials to prevent the WMSDs such as KOA in the construction [35].

Using wearable robotics during kneeling has a potential intervention to reduce the WMSD risks. Metabolic reduction were shown in the tests of Young's group using bilateral knee exoskeleton during incline walking in recent years [36]. However, real-time control of the wearable robotic devices is challenging because of difficulty to predict human dynamics during kneeling motions [37, 38]. Impedance control is commonly used for human-robot interactions and quasi-direct drive (QDD) actuation was recently developed to meet the high-torque, high-backdrivability, and high-bandwidth requirements [39].

It is challenging to design a lightweight exoskeleton and its control system for real-time kneeling tasks due to large knee flexion and required high assistive power. To enable real-time gait detection in kneeling tasks, a set of wearable inertial measurement units (IMUs) are used to identify various kneeling events, types of kneeling (i.e., single- or double-leg), and kneeling with changes in trunk posture. In this dissertation, the main focus is on the control of the wearable device for construction workers on sloped and level surface and evaluate and demonstrate its performance and efficacy through reduction of the muscle activations and knee contact pressures during the kneeling gaits. The

kneeling event detection is based on measurements of the thigh, shank and knee angles that includes the aforementioned events. Control of the exoskeleton device is based on the gravity compensation of the trunk and thighs to assist subject during kneeling down, standing up from kneeling position, or stationary kneeling.

1.2.4 Walking Gaits Estimation with LSTM based Recurrent Neural Networks

Walking is one of the most common locomotions in construction activities. Construction workers regularly perform walking tasks on leveled and inclined surfaces. It is critical to monitor workers' gaits and body poses in real-time for safety and health conditions. However, human walking is a complex task involving hundreds of muscles, bones and joints working together and it is hard to monitor their gaits in real-time. Visual cameras, inertial measurement units and motion sensors are among the most widely used activity tracking, monitoring and sensing systems [40] in construction. In recent years, Young's group presented results in human walking activities detection and slope angle estimation using multiple sensors that are including IMUs, EMGs and goniometers [41]. Wearable IMUs are particularly attractive for gait detection and posture estimation in construction because they are small-size, low-cost and non-intrusive [42]. Comparing with vision cameras, IMUs do not need much infrastructure support and can perform under various weather conditions.

Wearable inertial sensors were widely used for lower-limb kinematics [43, 44]. Inertial sensor-based gait classification and detection were also applied to human kneeling, squatting and foot slip activities (e.g., [45, 46]). In [47], IMUs were attached to the back of the helmet and the worker's back for head, neck and trunk inclination estimation. A similar development was reported In [48] to detect and identify worker activity using machine learning techniques.

However, human body pose estimation using IMU measurements are not extensively studied. Moreover, the detection for real-time applications were not systematically dis-

cussed. In [49], a real-time gait event detection was presented to capture walking gait events (i.e., heel strike, toe-off, etc.) over level and inclined surfaces and staircases using one single IMU. Similar types of real-time walking gaits detection were also reported in [50, 51, 52] for periodic movement using machine learning methods.

To monitor workers' gaits and high dimensional body poses in real-time, GPDM is a useful tool to reduce data space dimensions for biped walking activities and machine learning is a useful tool for human motion estimation. Machine learning techniques for human activity detection were reported in recent years. In [53], recurrent neural network (RNN) with long short-term memory (LSTM) cells were used to reconstruct human poses during various motions in real-time. A hierarchical multivariable hidden Markov model was employed in [54] for full-body locomotion reconstruction of human walking, running, jumping, and hopping motion on a flat floor using one IMU attached to the subject's shank. Considering the periodic walking gait, a phase-functioned neural network model was presented in [55]. We focus on the GPDM based machine learning frameworks for human gaits and full body pose estimation in this dissertation.

1.3 Dissertation Outline and Contribution

There are seven chapters in this dissertation. Chapter 1 presents the introduction and background. In Chapter 2, we propose a human strength capacity estimation method based on muscle synergy model during human-manipulator interaction. In Chapter 3, we develop and implement real-time man-manipulator interaction control and motion planning. Human intention force and motion are estimated by supervised learning. In Chapter 4, human balancing model is proposed for construction workers. In Chapter 5, a novel real-time controller is proposed and a mechatronic assistive device system is designed for assisting construction workers with bilateral knee exoskeleton. In Chapter 6, a machine learning based approach is proposed to detecting human motion and gait in construction site. Chapter 7 concludes the dissertation and discusses the future research

directions.

The modeling and control of physical human-robot interactions are challenging because human system is often difficult to predict. In construction, there are many human-robot interaction applications, such as lifting and transporting heavy bricks, installing drywall, and welding. Assistive robotic devices are important in assisting muscle strength of a human upper extremity in these construction activities. However, for many physical human-robot interaction activities, high dimensional human muscles are coordinated to achieve simple tasks and human system can be modeled by dimension reduction. In Chapter 2, a muscle synergy based human force estimation scheme is proposed for physical human-robot interactions. We take advantages of the physical human-robot interactions and use the interactions forces information to identify these muscle synergies without using the EMG sensors.

In Chapter 3, we extend the muscle synergy model and use it in the force control of human-manipulator interactions. With muscle synergy models, supervised neural networks are used to predict human force and intention motion during the interactions. With the prediction of human motion and force, the disturbance force is estimated and an observer based controller is developed to compensate the disturbance force during the real-time human-robot interaction applications. Extensive experiments are conducted.

In Chapter 4, we focus on human system modeling especially human postural balancing of kneeling gaits on sloped surface for construction workers. A mixed reality setup is designed to construct high elevation and visual scenes and wearable IMUs are used to obtain human trunk motion. We also use the inverted pendulum model and neuro-controller to analyze the human balance performance. Multi subjects experiments are conducted.

In Chapter 5, we present a wearable mechatronic system that consists of active knee exoskeletons and a wearable sensing suite to assist construction workers in kneeling tasks. We design an lightweight exoskeleton system which can provide large assistive

torques without increasing additional weights and modified to wearable, nontethered configuration. We develop the control of the exoskeleton device based on the gravity compensation of the trunk and thighs to assist subject during kneeling down, standing up from kneeling position, or stationary kneeling. The feasibility demonstration of wearable assistive devices to reduce knee contact loads and muscle activation during kneeling tasks is presented for construction workers on sloped and level surface during single- and double-leg kneeling.

In Chapter 6, we present a real-time gait detection and pose estimation scheme for human walking on flat and sloped surfaces using one single IMU. An LSTM based recurrent neural network approach is first used to detect the human walker gaits and the slope angle. A learned motion manifold is then constructed using the gait activity information. We use GPDM to construct the human motion manifold and predict walking joint angles in real-time for construction workers walking motions.

Finally, we conclude this dissertation in Chapter 7 and also discuss the potential outcomes with the human modeling and assistive device systems applied in construction applications. The results demonstrate that the physical principle-based human models can be the enabling tool in estimating human performance in construction activities. This property is also verified by multi-subjects experiments. We also discuss possible improvements of the proposed work and other potential applications to reduce WMSDs for the construction workers.

The main contributions of this dissertation are the human modeling, dynamic system analysis, and control system design of physical human-robot interactions. The detailed contributions of this dissertation are listed as follows:

1. We build a muscle synergy-based estimation scheme for physical strength capacity of human limbs. The estimation design is attractive for real-time applications of physical human-robot interactions and assistance-as-needed control design.

2. Muscle synergy-based human force scheme is developed and disturbance re-

jection control system is designed for physical human-manipulator interactions. The proposed method does not need the EMG sensors in the control system design and the proposed controller compensate for unknown disturbance, which is attractive for real-time construction applications,

3. Human analytical models for postural balancing is studied for kneeling gaits on elevated and inclined surfaces. Mixed Reality system is used to providing immersive experimental environment for high elevation scenes. The proposed balancing model complements the existing work by providing new results in kneeling gaits on elevated and inclined surface.

4. We design and evaluate the lightweight wearable sensing devices and knee exoskeletons for construction workers. We develop the control system of the wearable device for construction workers on sloped and level surface during single- and double-leg kneeling and prove the feasibility of wearable assistive devices to reduce knee contact loads and muscle activation during kneeling tasks. Comparing with existing exoskeletons, our system provides high torque and power in the kneeling tasks, and remains lightweight and non-tethered configuration in the meantime.

5. Novel GPDM based gait detection and pose estimation frameworks are developed for real-time applications using one single IMU. The design can be integrated with wearable robotic systems to reduce the workers' WMSD risks in construction.

Chapter 2

Muscle Synergy Modeling for Human-Robot Interaction

2.1 Introduction

Construction workers perform repetitive motion like lifting and handling heavy tools. Assistive robotic manipulators can augment human upper limb capability and provide necessary assistive, and have the potential to reduce WMSDs in these tasks. Assist-as-needed control is one of main concepts to design the assistive robotic systems [9, 10]. In these human-robot interactions, workers try to conduct certain tasks, such as move or lift weights, etc., and the robotic devices provide necessary assistance to deliver the needed forces. To design assist-as-needed controllers for collaborative robot manipulators, one basic requirement assist-as-needed controllers is the knowledge of human physical strength capacity (e.g., the maximum limb forces) to achieve the desired locomotion. The goal of this chapter is to present a computational scheme to estimate physical capacity envelopes using muscle synergy model and physical human-robot interactions.

Without extensively probing limit conditions, estimation and obtaining of the physical strength capacity of human limbs are challenging due to several reasons. First, human musculoskeletal systems are complex and it is difficult, if not impossible, to identify each muscle's physical envelopes without extensively experiments to probe these limits. Second, multiple muscles are involved in one physical activity and contributions of each muscle in these motion activities are different, which is difficult to be identified and estimated. Finally, the physical capacity of human limbs also depend on the limb pose and

the estimation scheme must provide a systematic way to compute the envelopes at any given poses.

The Hill-type muscle model is commonly used to define muscle properties [56, 57]. To identify the muscle activation model, various approaches were proposed in the past, such as optimization method [58], adaptive neural network [59]. Adaptive or robust control designs were also used to compensate for un-modelled dynamics or model uncertainties in muscle activities [60] or human-robot interactions [17, 61]. However, all of the above-mentioned work do not address the estimation of the physical strength capacity for biomechatronic or human-robot interactions applications.

Muscle synergy model was used as an enabling tool for human effort estimation [62, 6]. An individual time-varying muscle synergy can be viewed of as a fixed motor program [63, 64]. We present an estimation scheme that is built on the muscle synergy model for human limb motion. We capture the limb motion and its forceful interactions with the robot as a set of combination of the synergies. For example, using four synergies can reconstruct approximately 90% of the total muscle activities and variability [65]. To estimate and obtain the strength capacity, we use the identified musculotendon model [66] to compute their physical limits. Electromyography (EMG) measurements are commonly used to construct muscle synergies [13]. However, it is not convenient to wear EMG probes in many human-robot interactions to monitor and obtain muscle activation in practical applications. Unlike the most studies that use EMG measurements, we take advantages of the physical human-robot interactions and use the interactions forces information to identify these muscle synergies without using EMG.

The main contribution of the work lies in the muscle synergy-based estimation for physical strength capacity of human limbs. The estimation design is also attractive for real-time applications such as physical human-robot interactions and assistance-as-needed control design. Furthermore, the proposed estimation does not need the experiments to physically probe the limbs' capability limits extensively. We apply and

demonstrate the approach to upper-limb interactions with a five degree-of-the-freedom (DOF) manipulator. The experiments confirm the design performance.

The rest of the chapter is organized as follows. We present the muscle synergy-based force model in Section 2.2. The physical strength capacity estimation is discussed in Section 2.3. We present the experiments in Section 2.4 and the results in Section 2.5. Finally, we summarize the concluding remarks in Section 2.6.

2.2 Muscle Synergy-based Force Model

We consider the human-robot system as shown in Fig. 2.1(a). A robotic manipulator is used to assist human for certain tasks, such as lifting a weight, etc. Fig. 2.1(b) represent the schematic of human upper-limb interacting with a robotic manipulator. In our application, manipulator has three rotational joints and human arm has two rotational joints in the vertical plane. To design an assist-as-needed strategy for the robotic manipulator, it is critical to estimate human physical strength capacity in real time.

Each upper-limb joint is driven by a group of muscles and the relative ratio of all muscle excitation in the group is assumed fixed, namely, a muscle synergy. The muscle activation is expressed as a linear summation of spatial and temporal patterns of muscle synergies as

$$\boldsymbol{M}(t) = \boldsymbol{W}\boldsymbol{C}(t) = \sum_{i=1}^{n} \boldsymbol{w}_i c_i(t),$$

where $\boldsymbol{M}(t) \in \mathbb{R}^N$ is the muscle activation vector, N is the number of muscles, $\boldsymbol{W} = [\boldsymbol{w}_1, \cdots, \boldsymbol{w}_n] \in \mathbb{R}^{N \times n}$ is the spatial pattern of the muscle synergy matrix, n is the number of muscle synergies, and $\boldsymbol{C}^T(t) = [c_1(t), \cdots, c_n(t)]^T \in \mathbb{R}^n$ is temporal pattern matrix of the muscle synergy. $\boldsymbol{w}_i$ and c_i denote the ith muscle synergy pattern and activation level, respectively. The activation level is related to the muscle force model and the musculoskeletal model.

Using the Hill model [56, 57], muscular force F is captured as output of a contractile

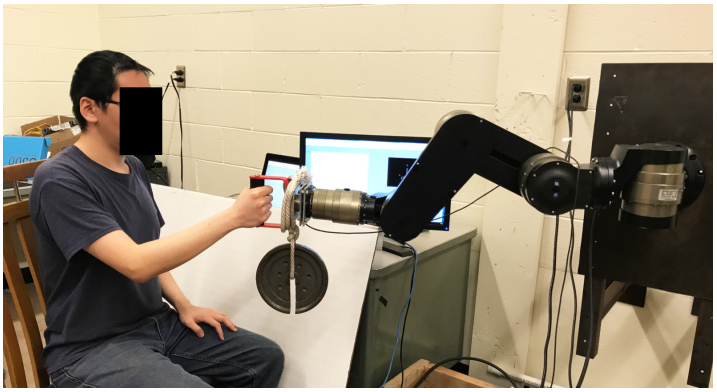

(a)

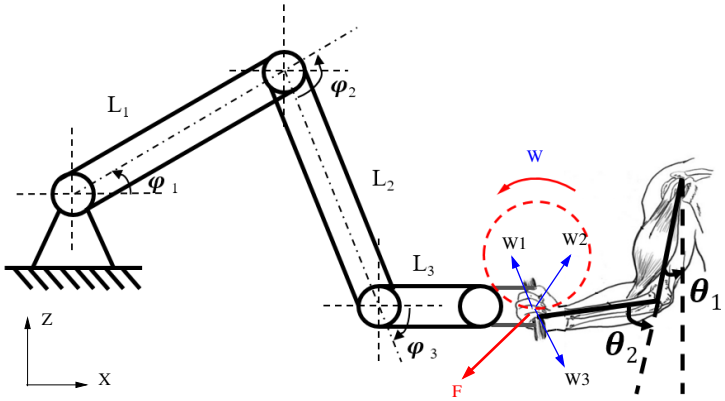

(b)

Figure 2.1: (a) An example of robot-assistive weight lifting task with a robotic manipulator. (b) The schematic of the human upper-limb model and its interaction with a robotic manipulator in planar motion.

element and a parallel element,

$$F = a(t)F_0^{\max} f_l(q) f_v(\dot{q}) \cos(\alpha),$$

where q represents the joint angle, $a(t)$ is a muscle activation factor, $F_0^{\max}$ is the maximum force that can be generated from the muscle. Functions $f_l(q)$ and $f_v(\dot{q})$ capture the force-length and force-velocity relationships, respectively. Variable α is the pennation angle that alters muscle force and for simplicity, is assumed as a constant value.

As described in [67], the joint torque T is represented as

$$\sum_{i}^{n_T} a_i h_i(q, \dot{q}) = T, \tag{2.1}$$

where $h_i(q, \dot{q}) = F_i^{\max} f_l(q) f_v(\dot{q}) \cos(\alpha) r_i(q)$, $r_i(q)$ is the moment arm length for force F_i, and n_T is the number of muscles involved in generating the torque T. The muscle activation factors a_i in (2.1) are chosen to minimize $J = \sum_{i=1}^{n_T} a_i^2(t)$ and the solutions are obtained as

$$a_i^* = \frac{h_i(q, \dot{q})}{\sum_j^{n_T} h_j^2(q, \dot{q})} T. \tag{2.2}$$

We arrange the representation of a_i as a linear combination of flexor synergy ratio w_i^f (for positive joint torque) and extensor synergy ratio w_i^e (for negative joint torque) as

$$a_i = a_f w_i^f + a_e w_i^e, \tag{2.3}$$

where the synergy ratios are introduced as $w_i^f = \frac{a_i^*}{a_f^*} = \frac{h_i}{h_f} = w_i^f(q, \dot{q})$, if $w_i^f > 0$; $w_i^f = 0$ if $w_i^f \leq 0$; and $w_i^e = \frac{a_i^*}{a_e^*} = \frac{h_i}{h_e} = w_i^e(q, \dot{q})$ if $w_i^e > 0$ and $w_i^e = 0$ if $w_i^e \leq 0$. Note that synergy ratios w_i^f and w_i^e are pose-dependent and invariant under muscle activation.

It is clear from (2.3) that a joint torque is represented as a linear combination of two synergies $\boldsymbol{w}^f$ and $\boldsymbol{w}^e$. In this chapter, we focus on a two-joint arm planar motion and the muscle forces are chosen to be represented by three synergy vectors, denoted as $\boldsymbol{w}_j$, $j = 1, 2, 3$. Fig. 2.1(b) shows a schematic of synergy-based muscle force model for the planar arm motion. Using the above muscle synergy model, the resultant muscle force excitation vector $\boldsymbol{e}(t) \in \mathbb{R}^N$ is represented as

$$\boldsymbol{e}(\boldsymbol{q}) = \boldsymbol{W}(\boldsymbol{q}) \boldsymbol{C}(t), \tag{2.4}$$

where the generalized coordinate for the two-joint upper-limb is $\boldsymbol{q} = [\theta_1 \ \theta_2]^T$, $\boldsymbol{W}(\boldsymbol{q}) = [\boldsymbol{w}_1 \ \boldsymbol{w}_1 \ \boldsymbol{w}_3] \in \mathbb{R}^{N \times 3}$ captures the three synergies for the upper-limb planar motion and

$\boldsymbol{C}(t) \in \mathbb{R}^3$ is the time-varying activation vector.

2.3 Strength Capacity Estimation with Physical Human-Robot Interactions

In this section, we first present a human-robot interaction force model and then discuss how to estimate the human strength capacity through physical human-robot interactions.

2.3.1 Synergy-Based Human Force Model

We use the upper-limb planar motion as shown in Fig. 2.1(b). The human force at end-effector is written as

$$\boldsymbol{F}(\boldsymbol{q}, \dot{\boldsymbol{q}}) = (\boldsymbol{J}^T(\boldsymbol{q}))^+ \boldsymbol{r}(\boldsymbol{q}) \boldsymbol{F}_0^{\max} \boldsymbol{F}_S(\boldsymbol{q}) \boldsymbol{e}(\boldsymbol{q}), \tag{2.5}$$

where $\boldsymbol{F}(\boldsymbol{q}, \dot{\boldsymbol{q}}) \in \mathbb{R}^2$ is the planar force vector, $\boldsymbol{J}(\boldsymbol{q})^T \in \mathbb{R}^{2\times 2}$ is the transpose of the Jacobian, $\boldsymbol{J}^+ = (\boldsymbol{J}^T\boldsymbol{J})^{-1}\boldsymbol{J}^T$ is the pseudo-inverse of matrix $\boldsymbol{J} \in \mathbb{R}^{2\times 2}$, $\boldsymbol{r}(\boldsymbol{q}) = [\boldsymbol{r}_1, \cdots, \boldsymbol{r}_N] \in \mathbb{R}^{2\times N}$ is the torque-arm matrix, $\boldsymbol{F}_O^{\max} = \mathrm{diag}\{F_1^{\max}, \cdots, F_N^{\max}\} \in \mathbb{R}^{N\times N}$ is the diagonal maximal muscle force matrix, and $\boldsymbol{F}_S(\boldsymbol{q}) \in \mathbb{R}^{N\times N}$ is the diagonal matrix of the scaling factors for the muscle force-length characteristics. In (2.4), the elements of $\boldsymbol{e}(\boldsymbol{q})$ and $\boldsymbol{C}(t)$ satisfy that $0 \le e_i \le 1$, $c_j \ge 0$, $i = 1, \ldots, N$, $j = 1, 2, 3$.

Combining (2.4), we re-write (2.5) as

$$\boldsymbol{F}(\boldsymbol{q}, \dot{\boldsymbol{q}}) = \boldsymbol{A}_F(\boldsymbol{q}, \dot{\boldsymbol{q}}) \boldsymbol{C}(t), \tag{2.6}$$

where $\boldsymbol{A}_F(\boldsymbol{q}, \dot{\boldsymbol{q}}) = (\boldsymbol{J}^T(\boldsymbol{q}))^+ \boldsymbol{r}(\boldsymbol{q}) \boldsymbol{F}_0^{\max} \boldsymbol{F}_S(\boldsymbol{q}) \boldsymbol{W}(\boldsymbol{q}) \in \mathbb{R}^{2\times 3}$ is the gain between the muscle activation vector and the end-effect force. Relationship between $\boldsymbol{F}$ and muscle activation $\boldsymbol{C}(t)$ in (2.6) is important for the human strength capacity estimation. We use measurements of force $\boldsymbol{F}$ and muscle activation $\boldsymbol{C}(t)$ to estimate the value of $\boldsymbol{A}_F(\boldsymbol{q}, \dot{\boldsymbol{q}})$.

2.3.2 Human Arm Skeletal Dynamics and Robot Control

We consider the arm dynamics as a rigid two-link planar arm [68]

$$\boldsymbol{M}_h(\boldsymbol{q})\ddot{\boldsymbol{q}} + \boldsymbol{C}_h(\boldsymbol{q}, \dot{\boldsymbol{q}})\dot{\boldsymbol{q}} + \boldsymbol{G}_h(\boldsymbol{q}) = \boldsymbol{J}^T\boldsymbol{F}, \tag{2.7}$$

where $\boldsymbol{M}_h(\boldsymbol{q})$, $\boldsymbol{C}_h(\boldsymbol{q}, \dot{\boldsymbol{q}})$, and $\boldsymbol{G}_h(\boldsymbol{q})$ are the arm's inertia, Coriolis, and gravity matrices, respectively. In (2.7), the applied joint torques by muscles activation are considered as the force vector $\boldsymbol{F}$.

In experiments, the human-applied force drives the upper limb such that the human hand (i.e., the robot end-effector) follows a desired trajectory. The end-effector trajectory is designed that human can gradually increase their applied force so that the end-effector moving velocity reaches its maximum value. At that moment, we consider the human upper-limb strength reaches its capacity and correspondingly, the muscle activations reach their maximum levels. A compliance control is designed for the manipulator to regulate the human-robot interactions for safe operation while tracking the trajectory. The admittance controller provides a desired dynamic relationship between the position and the interaction force [69, 70]. We design the transfer function between force $F = \|\boldsymbol{F}(\boldsymbol{q}, \dot{\boldsymbol{q}})\|$ and the position tracking error $\delta r = \|\boldsymbol{r}_e(t) - \boldsymbol{r}_e^d(t)\|$, where $\boldsymbol{r}_e(t)$ and $\boldsymbol{r}_e^d(t)$ are the actual and desired end-effector position vectors, respectively, as an ideal second-order system, i.e.,

$$G_{hri}(s) = \frac{\delta r(s)}{F(s)} = \frac{1}{s^2 + 2\xi\omega_n s + \omega_n^2}, \tag{2.8}$$

where ω_n and ξ are the frequency and damping coefficient of the desired admittance at the human-robot interactions, respectively.

It is desirable to construct a human neuro-controller for the planar motion. Inspired by the work in [71], we construct a proportional-derivative (PD) control model to capture

the human neuro-control action for the planar arm reaching movement as

$$\boldsymbol{C}_{human}(t) = \boldsymbol{K}_P \Delta \boldsymbol{q}(t) + \boldsymbol{K}_D \Delta \dot{\boldsymbol{q}}(t) + \boldsymbol{K}_A \Delta \ddot{\boldsymbol{q}}(t), \tag{2.9}$$

where $\Delta \boldsymbol{q}(t) = \boldsymbol{q}(t) - \boldsymbol{q}^d(t)$, $\boldsymbol{q}^d(t) = \mathrm{inv}(\boldsymbol{r}_e^d(t))$ is the arm joint angle profile for a given $\boldsymbol{r}_e^d(t)$, and $\mathrm{inv}(\cdot)$ is the inverse kinematic mapping of the two-joint arm links. $\boldsymbol{K}_P$, $\boldsymbol{K}_D$, and $\boldsymbol{K}_A \in \mathbb{R}^{3\times 2}$ are matrices for proportional, derivative and acceleration gains, respectively.

One motivation of using neural controller (2.9) is to reconstruct the human muscle activation without direct real-time measurements of the muscle activities. To achieve this goal, we estimate the gain matrix $\boldsymbol{A}_F(\boldsymbol{q}, \dot{\boldsymbol{q}})$ in (2.6) and then use (2.9) to reconstruct $\boldsymbol{F}(\boldsymbol{q}, \dot{\boldsymbol{q}})$ by (2.6). This model-based prediction is attractive since we can potentially estimate human strength capacity without using muscle activity sensors such as EMG. We will demonstrate the experimental results in Section 2.4.

2.3.3 Strength Capacity Estimation

The human arm's strength capacity is characterized by the maximum force generated by muscle activation. Given the non-negative property of matrices $\boldsymbol{W}(\boldsymbol{q})$ and vector $\boldsymbol{C}(t)$, the strength capacity is obtained by maximizing the value of $\boldsymbol{C}(t)$, namely,

$$C^{\max} = \max_{\boldsymbol{q}, \dot{\boldsymbol{q}}, \ddot{\boldsymbol{q}}} \|\boldsymbol{C}(t)\|. \tag{2.10}$$

To calculate $C^{\max}$ in (2.10), we consider to use dynamics (2.7) and human-robot interactions. In the testing protocol, the subject is guided to follow a desired planar trajectory (e.g., a circle) to accelerate to a possible maximum velocity at the steady state. We denote the maximum velocity at the end-effector as $\dot{\boldsymbol{r}}_e^{\max}(t)$ and then the maximum joint angle as $\dot{\boldsymbol{q}}^{\max}(t) = \boldsymbol{J}^{-1}\dot{\boldsymbol{r}}_e^{\max}(t)$, where $\boldsymbol{J}$ is the Jacobian matrix. From (2.7), the

maximum muscle activation is expressed as

$$C^{\max} = \Big\| \left(\boldsymbol{J}^T \boldsymbol{A}_F(\boldsymbol{q}^{\max}, \dot{\boldsymbol{q}}^{\max})\right)^+ (\boldsymbol{M}_h(\boldsymbol{q}^{\max})\ddot{\boldsymbol{q}}^{\max} + \boldsymbol{C}_h(\boldsymbol{q}^{\max}, \dot{\boldsymbol{q}}^{\max})\dot{\boldsymbol{q}}^{\max} + \boldsymbol{G}_h(\boldsymbol{q}^{\max}) \Big\|, \tag{2.11}$$

where $\boldsymbol{q}^{\max}(t)$ and $\ddot{\boldsymbol{q}}^{\max}(t)$ are the arm joint angle and acceleration profiles, respectively. The strength capacity in term of force is $\boldsymbol{F}^{\max} = \boldsymbol{A}_F(\boldsymbol{q}^{\max}, \dot{\boldsymbol{q}}^{\max})\boldsymbol{C}^{\max}(t)$.

2.4 Experiments

2.4.1 Experimental Setup and Protocols

Five subjects (named A to E) were recruited to conduct the experiments. The subjects were identified as healthy and capable to operate machines. In experiment, the subjects sat on a chair while their trunks were secured to the chair with straps. The subjects were trained to operate a manipulator by grasping the handle at the tip of the manipulator; see Fig. 2.4.1. The compliance controller allows the manipulator to move with the subject's hand freely. The subjects practiced several times before the experiment and took rests between each trial. An informed consent form was signed by all the subjects and the testing protocol was approved by the Institutional Review Board (IRB) at Rutgers University.

In experiments, the subject was only allowed to turn his elbow and shoulder joint in the vertical plane (the XZ plane). The subject was instructed to follow a circular shape trajectory (with the diameter about 7 inches) in the vertical plane. Both the desired trajectory and the actual gripper trajectory were shown on a computer monitor in front of the subjects. The trajectory was also physically projected on a nearby paperboard by using a laser pointer mounted on the end-effector. In the first set of experiments, the subjects followed a circular shape trajectory with angular speed ω_0 and accelerated or decelerated as their choices. The subjects ran the circular motion several times with

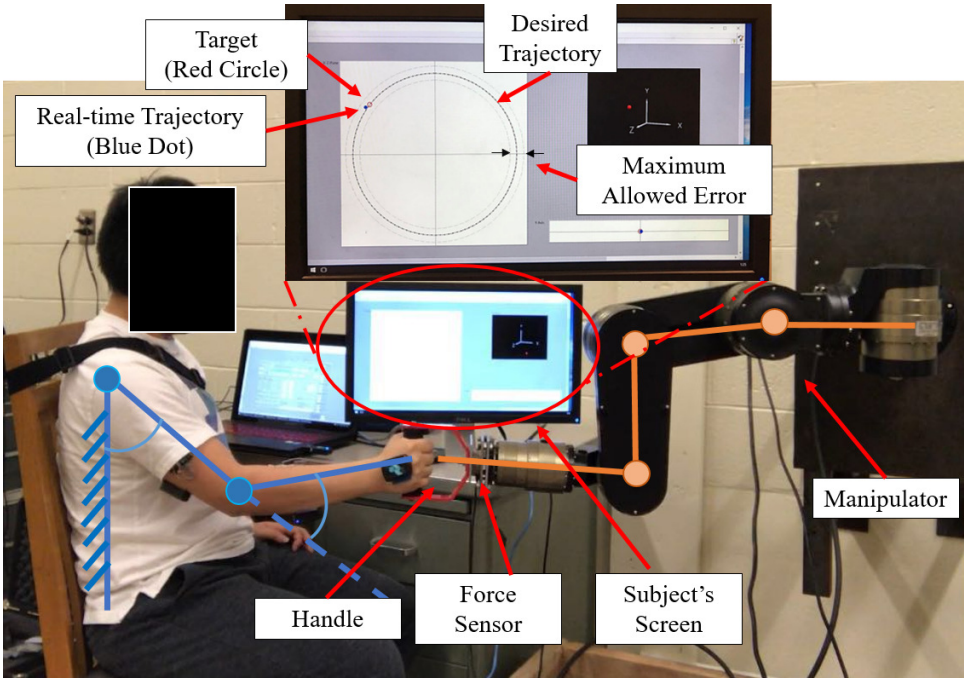

Figure 2.2: The experimental setup for the human-robot interaction with human hand movement in the vertical plane.

increasing resistance forces that were applied by the controlled manipulator. In the second set of experiments, the subjects still followed the same circular trajectory. However, they were asked to accelerate as fast as they can until reaching the possible maximum velocity, while they tried to keep on the trajectory closely. Both the motion and the interaction force were recorded.

The upper-limb movements were obtained by the motion capture system (8 Bonita cameras, Vicon, Inc., Oxford Metrics, Oxford, UK) with markers placed on the arm. The motion capture data was sampled at 100 Hz. The human-robot interaction force was recorded by a 6-DOF force sensor (model Mini45 from ATI Inc.) that was mounted at the end-effector. The force data was sampled at a frequency of 1000 Hz. To validate the estimated muscle synergies, a surface EMG system (MyoMuscle System from Noraxon Inc.) was used to obtain the muscle activities and the EMG sampling rate was 1500 Hz. For the compliance control (2.8), we used $\omega_n = 10\sqrt{10}$ rad/s and $\xi = \sqrt{10}$.

2.4.2 Muscle Activity Measurements

In experiments, the activities of eight muscles were recorded: Brachialis (BRD), Biceps (BI), MedTriceps (MTRI), LatTriceps (LTRI), Anterior deltoid (ADELT), Medial deltoid (MDELT), Posterior deltoid (PDELT), and Pect major (PECT). The raw EMG data were processed by a series of post-processing steps. Notch filtering was first applied to eliminate noise. A high-pass filter was then used to remove DC bias in the signals. The processed data were rectified and smoothed by passing through a low-pass filter. Finally, non-negative matrix factorization (NNMF) method was used to decompose the EMG signal and to generate muscle synergies.

2.5 Results

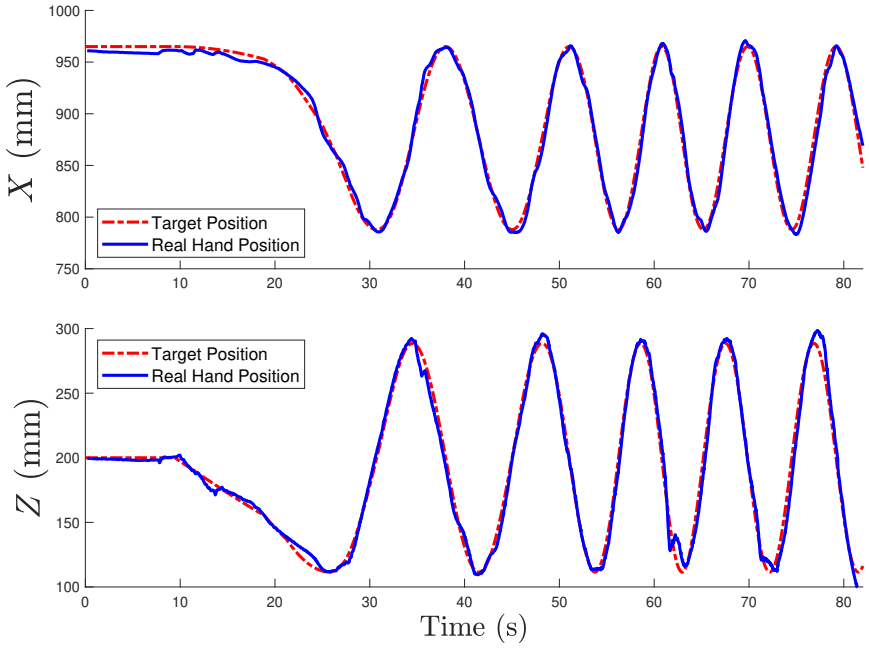

Figure 2.3: Tracking performance of the hand position in the XZ plane during one trial for Subject E.

Fig. 2.5 shows a typical subject hand motion trajectory (the X-axis and Z-axis directions) in one experiment trial. The period of the arm steady-state cyclic motion is around

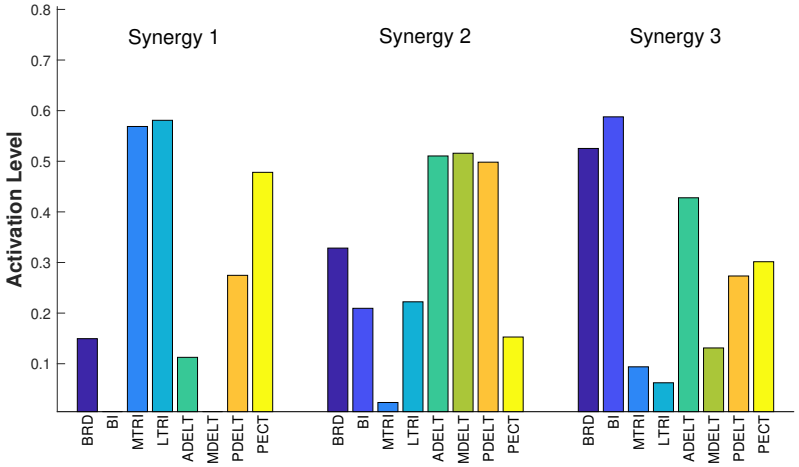

(a)

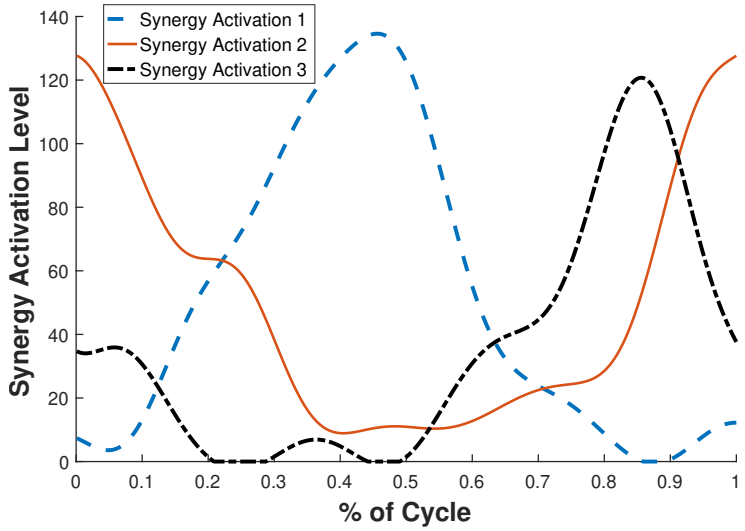

(b)

Figure 2.4: (a) Three muscle synergy patterns. Each synergy contains eight muscles: BRD, BI, MTRI, LTRI, ADELT, MDELT, PDELT, and PECT. (b) Three synergy activation levels $c_i(t)$, $i = 1, 2, 3$.

10 s. As the figure indicates, the subject accelerated from a slow periodic motion to a fast motion. All subjects conducted the experiments and the position tracking errors were small (within around 10 mm). In this study, we select three synergies to model the arm motion. Taking the EMG measurements from one trial experiment, Fig. 2.4(a) shows the three synergy patterns (i.e., $\boldsymbol{W}(\boldsymbol{q}) = [\boldsymbol{w}_1 \ \boldsymbol{w}_2 \ \boldsymbol{w}_3]$) and the corresponding activation levels (i.e., $\boldsymbol{C}(t) = [c_1 \ c_2 \ c_3]^T$) are shown in Fig. 2.4(b). In the latter, the acti-

vation levels are plotted over the time percentage of the cyclic motion. From Fig. 2.4(b), the three synergy activation levels $c_i(t)$, $i = 1, 2, 3$, achieve their peak values at different times and this implies that each synergy is activated at a certain motion interval. Fig. 2.5 shows the muscle activities for the eight muscles that are involved in upper-limb movement. It is clear from these results that the reconstructed muscle activities (solid lines) match the EMG measurements (dash-dotted lines). This confirms that three synergies account for majority of the muscle activation.

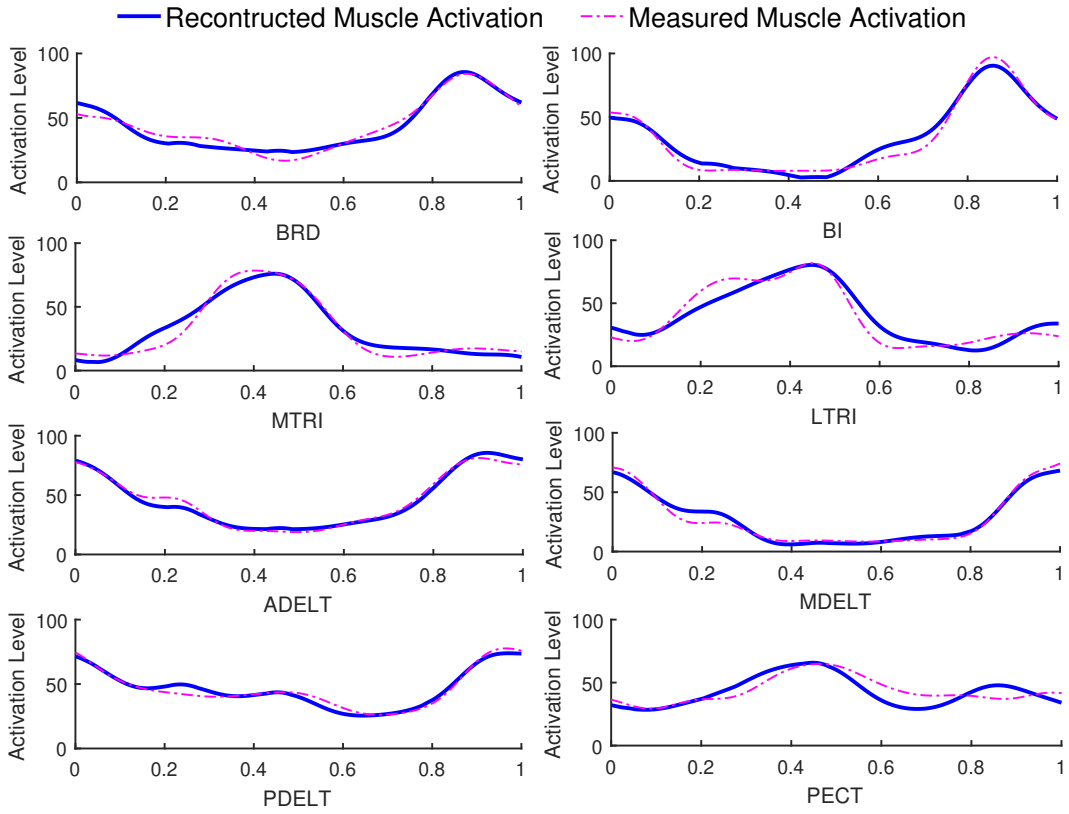

Figure 2.5: Comparison of muscle activation with the direct EMG measurements (dash pink lines) and synergy reconstruction (solid blue lines).

A set of muscle activation data from the EMG measurements and the arm motion data were used to estimate the model parameters in (2.9) by a least square method. With the identified parameters, we validate the model using other trial data by the same subject. Fig. 2.6(a) shows the comparison results of the muscle synergy activation level profiles $\boldsymbol{C}(t)$ over one motion cycle for subject E. Although showing small oscillations,

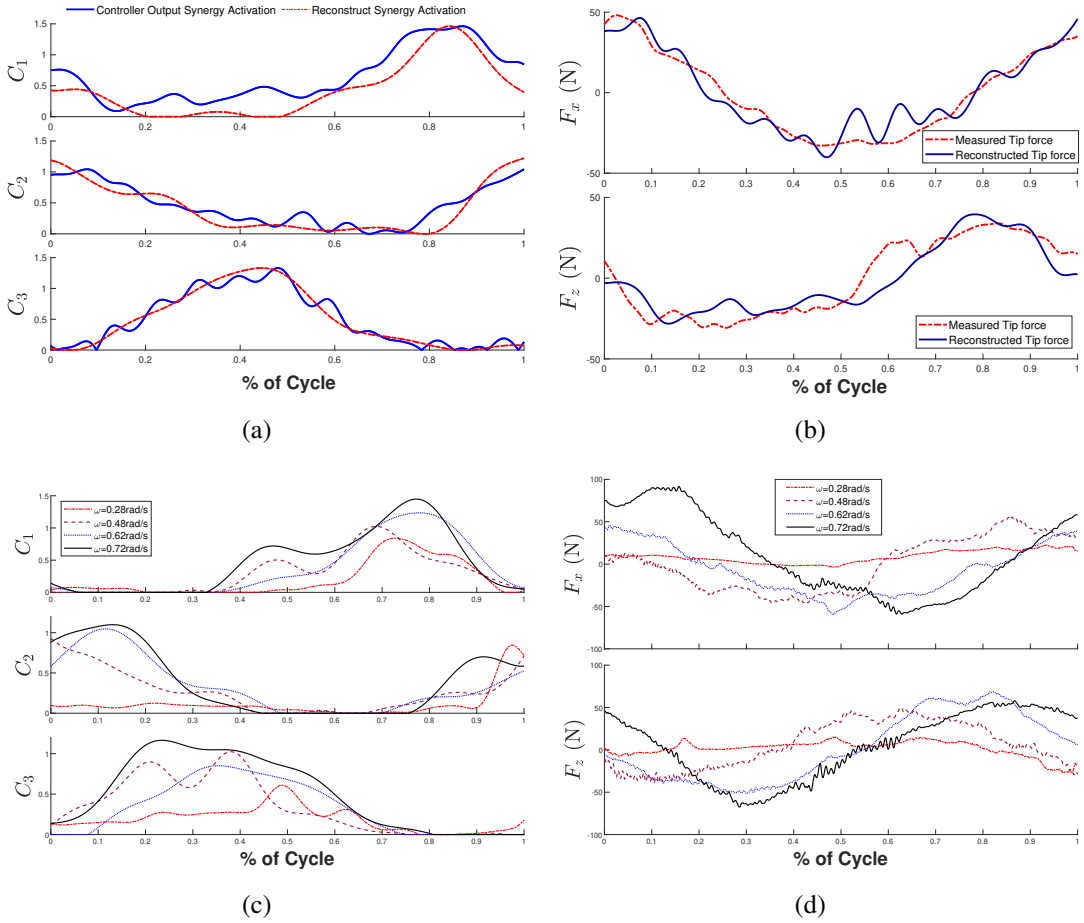

Figure 2.6: (a) Comparison of the muscle synergy activation $\boldsymbol{C} = [c_1 \ c_2 \, c_3]^T$ by the neural controller model (solid blue lines) and the reconstruction from direct EMG measurements (dash-dotted red lines) for subject E. (b) Reconstructed force $\boldsymbol{F} = [F_x \ F_z]^T$ comparisons between the synergy model prediction (solid blue lines) and the force measurements (dash-dotted red lines) for subject E. (c) Comparison of the muscle synergy activation $\boldsymbol{C}$ under various tracking speed $\omega_0 = 0.28, 0.48, 0.62$, and 0.72 rad/s. (d) Comparison of the muscle forces $\boldsymbol{F}$ under various tracking speed $\omega_0 = 0.28, 0.48, 0.62$, and 0.72 rad/s.

the model prediction by (2.9) follows the activation from the EMG measurements. The root mean square (RMS) errors of the estimation for three activation levels are 0.26, 0.12, 0.08, respectively. The results in Fig. 2.6(a) imply that Synergy 1 ($\boldsymbol{w}_1$) mainly contributes the activation between 60% to 100% of the cycle time (i.e., c_1 has large values), which corresponds to the arm retraction motion. Synergy 2 ($\boldsymbol{w}_2$) primarily contributes at the beginning and ending of motion cycle (i.e., c_2 has large values during

this period) and thus, it dominates the arm's up and down motion. Finally, Synergy 3 ($\boldsymbol{w}_3$) mostly contributes at the middle of the cycle and it is mainly related to arm extension motion.

With the synergy model, we estimate the gain matrix $\boldsymbol{A}_F$ in (2.6) using one trial data and then validate the force prediction by other trials data. Fig. 2.6(b) shows that the comparison of the predicted force $\boldsymbol{F} = [F_x \ F_z]^T$ with the force measurements for subject E. Similar to the muscle synergy activation $\boldsymbol{C}(t)$, the force prediction matches the measurement closely and the RMS errors are 7.79 N and 9.27 N for F_x and F_z, respectively. To further demonstrate changes of muscle activation under increasing cyclic tracking speed, Fig. 2.6(c) shows the $\boldsymbol{C}(t)$ profile under four different human arm tracking speed $\omega_0 = 0.28, 0.48, 0.62$, and 0.72 rad/s. When the arm rotates faster, a larger interaction force $\boldsymbol{F}$ and a higher power are needed. This is clearly demonstrated by the results shown in Fig. 2.6(c). It is also of interests to notice that the shape profiles of each element of $\boldsymbol{C}(t)$ are similar under various strengths. Fig. 2.6(d) further shows the comparison of interaction forces F_x and F_z and the trend is similar to that of $\boldsymbol{C}(t)$.

Finally, we estimate the human strength capacity under the arm planar motion. We take these motion data in Fig. 2.5 to estimate the strength capacity (2.11). Fig. 2.7(a) shows the maximum synergy activation $c_2^{\max}$ profile over the percentage of the cycle time (i.e., arm pose angle) for all five subjects. Although they have different activation levels at the same pose location, all five subjects' results show a similar trend during the motion. We further estimate the strength capacity of the total force for all five subjects as shown in Fig. 2.7(b). Clearly, we see that the horizontal force range (around $[-150, \ 100]$ N) is much larger than the vertical force range (around $[-40, \ 60]$ N). The profile of strength capacity shows an ecliptic shape.

To further validate the strength capacity estimation in Fig. 2.7(b), we conducted a static testing in which each subject was asked to apply his/her maximum force at a fixed pose angle along the circular trajectory (each $\pi/8$). The force magnitudes were recorded

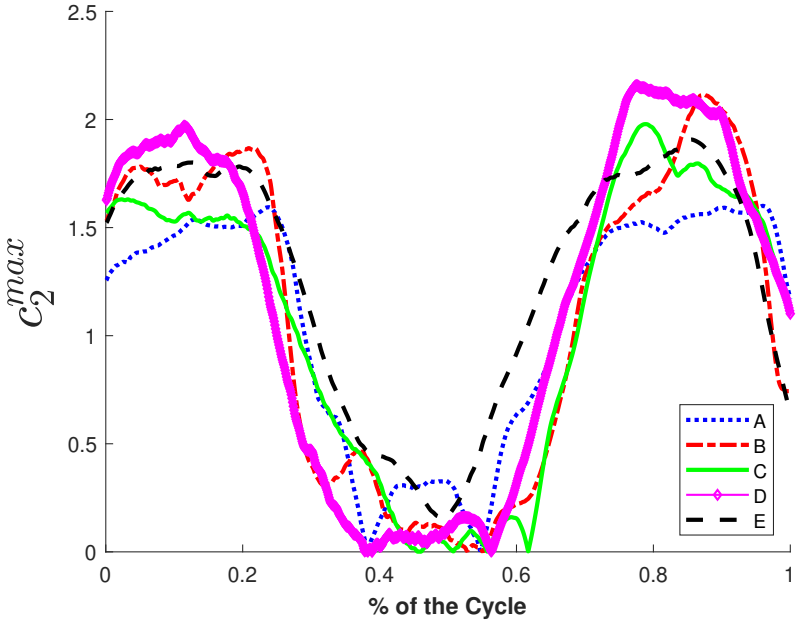

(a)

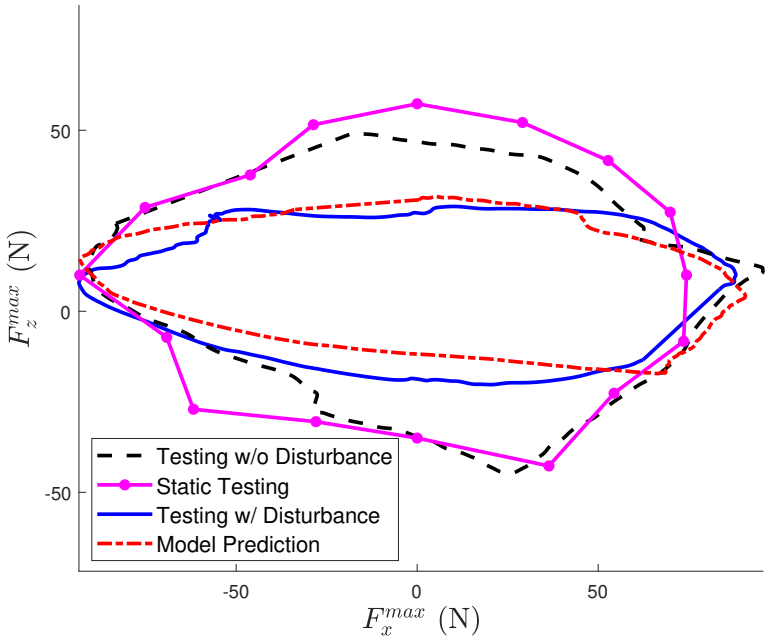

(b)

Figure 2.7: (a) The maximum synergy activation $c_2^{\max}$ for Synergy 2 as various pose position in the XZ plane. Five subjects' data were calculated by the synergy-based model. (b) Estimated strength capacity in the XZ plane for normal and disturbed condition for Subject E.

as the ground truth. During this static testing, the manipulator was controlled to resist and keep human hand position stationary at that location. Fig. 2.5 shows the estimation errors of the strength capacity at each testing location along the circular trajectory profile. The top plot in Fig. 2.5 shows the force errors $\Delta F^{\max}$ (i.e., the measured maximum force subtracts the predicted maximum force) over eight pose positions (equally positioned along the circle), while the bottom plot illustrates relative errors $e_{\max}$ in percentage (i.e, $\Delta F^{\max}$ divided by the measured maximum force). For all subjects, the mean values of the estimation is within 20% of the strength capacity as shown in Fig. 2.5.

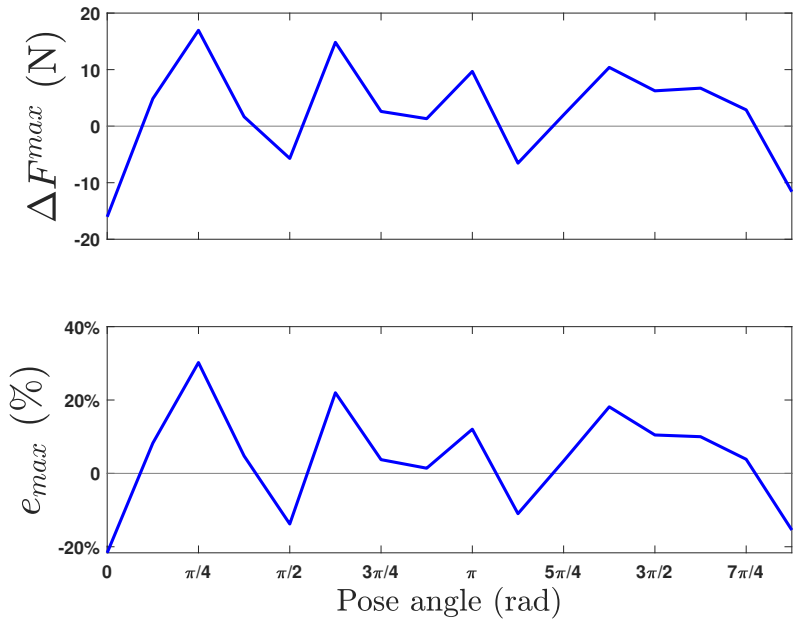

Figure 2.8: Estimation errors of the strength capacity at various pose angles: the top figure shows the error magnitudes (the error is calculated by the static measured values minus the predicted values) and the bottom plot shows the relative absolute errors in percentage.

To investigate performance under a subject with a significantly different capacity, we conduct an experiment by adding a constant disturbance weight of 10 N to the subject forearm when running the tests. The subjects ran the exact same tests and the maximum force ranges were estimated. The estimated strength capacity shown as the solid blue curve shown in Fig. 2.7(b). The estimated capacity reduces obviously at both the top

and bottom locations in the Z-axis direction; see Fig. 2.7(b). Comparing with the model estimated capacity space (i.e., the red dash-dotted curves in the figure), the testing result matches the model prediction.

2.6 Summary

In this chapter, we presented a muscle synergy model and a human-robot interaction approach to estimate human physical strength capacity. We took the advantages of the muscle synergy model that was built from offline EMG measurements. Unlike many other methods using real-time EMG measurements, the proposed approach did not need to conduct the static maximum loading tests with EMG sensors. Multi-subject experiments were conducted to validate and demonstrate the synergy model and strength capacity estimation results. The experiments confirmed the estimated strength capacity for all subjects was mostly within 20% of the static testing results.

Chapter 3

Muscle Synergy-Based Control of Human-Manipulator Interactions

3.1 Introduction

In Chapter 2, we proposed a method to estimated human strength capacity using muscle synergy model. Based on the knowledge of muscle synergy model, we propose to build a robust control system for human-manipulator interactions to further assist construction workers with robotic system in this Chapter. The paradigm assist-as-needed design tries to help human worker with necessarily required assistance to finish physical tasks in human-robot interactions. The amount of needed assistance is commonly calculated as the capability gap between that needs to achieve the required task and human intention or capability [72] or the estimation by the method presented in Chapter 2. Additionally, robotic assistance should also be robust to the changing environment and external disturbances. The motivation of this work lies in many applications in which robotic manipulators would augment human capability (e.g., strength and accuracy) as well as disturbance rejection in construction or other industries. For example, for the robot-assisted grit-blasting process as shown in Fig. 3.1, human operators provide guidance to the manipulator to conduct forceful grit-blasting task, while the process generates a large reactive force that disturbs the human-robot interaction [73]. Under a properly designed robot assistance, human operators would ideally apply their nominal forces (e.g., voluntary movement) to guide the robot without significant influence by the reactive

disturbance force. The goal of this chapter is to present an assist-as-needed manipulator control for human-robot interactions, such as that in the above-mentioned blasting process.

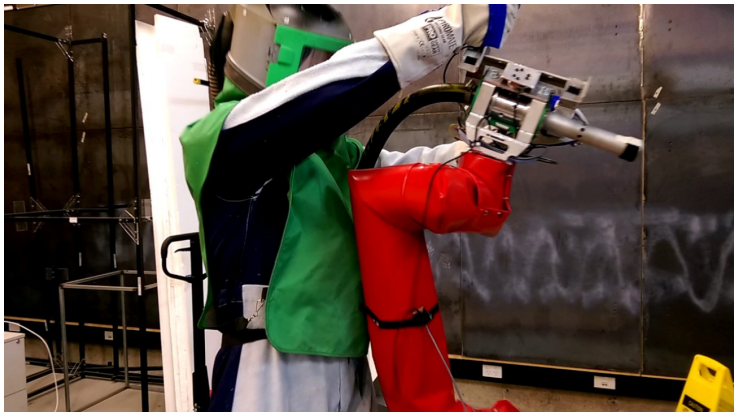

Figure 3.1: An application example for human-manipulator interactions control: robot-assisted grit-blasting [73].

To achieve a proper assistance in human-manipulator interaction tasks, it is desirable to obtain human force and intention motion. Neural networks method is particularly suitable for human intention motion estimation because of its capability to handle highly uncertain, nonlinear and complex systems [74]. In [18], the authors proposed a generalized regression neural network model to predict human knee joint angle using muscle synergy model. Combining with the muscle synergy models, the neural network design accurately predicts the human-robot interaction forces. The training of these neural networks is conducted off-line, while the force and intention motion prediction are used in real-time applications. One rationale for this design is the feasibility to use a same set of muscle synergies to model human arm motion and its interaction forces at the end effector [16].

Impedance/admittance control [75, 69] and learning control [76] are usually considered for physical human-robot interactions. Gribovskaya *et al.* constructed a learning task model to generate reference kinematic signals [77]. To reject known disturbances, a combined feed-forward and compensatory control was designed in [22] to achieve

pursuit tracking. However, the external disturbance forms are usually unknown and the approaches in the above-mentioned studies cannot be applied directly. Disturbance-rejection ability is critical for many human-robot interactions [10], such as the robot-assisted grit-blasting process aforementioned, in which disturbance reaction force could be large to hurt human operators if the manipulator does not share these forces completely or partially. Moreover, individual persons have distinctive muscle strength capacities and thus, the robot control needs to be robust to deal with these variations.

In this chapter, a muscle synergy-based force control of human-manipulator interactions is developed. Using the muscle synergy models, supervised neural networks are used to predict the human force and the intention motion trajectory passing through a few given target points and without use of EMG device. With these estimations, the disturbance force is predicted and the controller compensates for it such that human operators would not feel the impact of disturbance force. Under the proposed control, the robot follows human guided motion and provides necessary assistance to compensate for external loads and unknown disturbances. The control performance is demonstrated through multi-subject experiments in which both 2- and 3-dimensional upper-limb motion are conducted. The main contribution of the work lies in the muscle synergy-based robotic control for disturbance rejection and human effort assistance. The admittance control helps build assist-as-needed design for human-manipulator interactions.

The rest of the chapter is organized as follows. We present muscle synergy-based human intention force and motion estimation in Section 3.2. The admittance control of human-robot interactions is discussed in Section 3.3. Experiment setup is discussed in Sections 3.4 and the results are presented in Sections 3.5. Finally, we summarize the concluding remarks in Section 3.5.3.

3.2 Muscle Synergy-Based Human Force and Intention Motion Estimation

3.2.1 Synergy-Based Human Force Modeling and Estimation

Fig. 3.2(a) shows an experimental setup example of manipulator-assisted human material handling applications. Fig. 3.2(b) illustrates the modeling schematic for the arm-manipulator interactions. The motion of manipulator end-effector $\boldsymbol{O}$ is under guidance of human operator as shown in Fig. 3.2(b). Human operator is assumed to only know a set of target points (not entire trajectory), with positions denoted as $\boldsymbol{r}^d$. Human operators plan the trajectory and try to use voluntary motion to guide the robot to pass these target points.

To design an assist-as-needed strategy, it is critical to estimate human applied forces and motion in real time and muscle synergy is used here as a modeling tool. Human muscles work with skeletal system under voluntary motion and muscle activities are related with limb posture and targets [78]. Muscle force f_h at a joint can be expressed as a function of arm posture as in (2.2) [79].

Muscle synergy represents a group muscles that activate together at a relative fixed activation ratio. From modeling and control purposes, muscle synergy provides a low-dimensional representation of muscle activities for human movement. A time-varying synergy is a collection of muscle wave forms that can be expressed as a time-varying vector $w(t)$ [63]. Time dependence of the muscle activations is captured by the temporal structure of the synergies and by their onset times (denoted as t_is). For N muscles, the activation vector at time t is denoted as $\boldsymbol{a}(t) \in \mathbb{R}^N$ and expressed as

$$\boldsymbol{a}(t) = \sum_{i=1}^{n} c_i \boldsymbol{w}_i(t - t_i), \tag{3.1}$$

where $\boldsymbol{w}_i(t) \in \mathbb{R}^N$ denotes the ith muscle synergy at t, t_i represents the initiation delay of $\boldsymbol{w}_i(t)$, and c_i represents the ith amplitude coefficient, $i = 1, \ldots, n$, n is the number

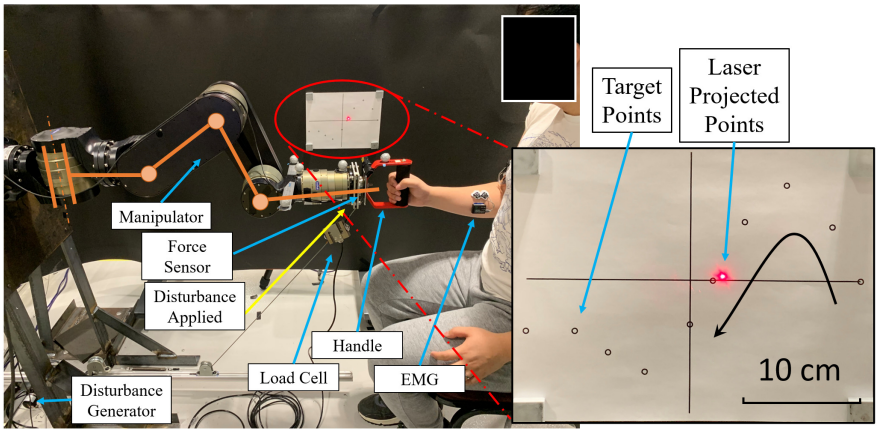

(a)

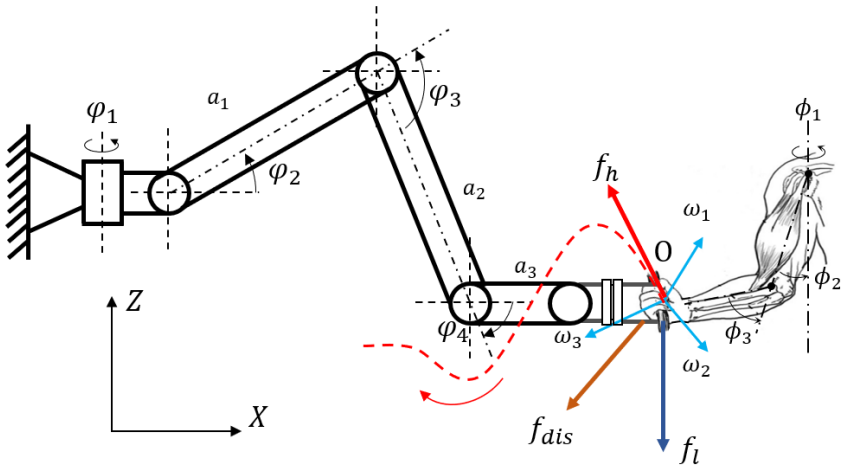

(b)

Figure 3.2: (a) Human-manipulator interactions experiment setup. The right zoom-in picture shows the set of target points to follow and current end-effector position (in the vertical plane) indicated by a laser pointer. (b) The schematic of the human upper-limb model and its interaction with a robotic manipulator in the workspace.

of muscle synergies. We consider the maximum duration for all synergies as $t_{\max}$ and it corresponds to J samples at discrete times τ_j, $j = 1, \ldots, J$. To express the time-varying synergy $w_i(t)$, we use a set of n matrices, $\boldsymbol{W}_i \in \mathbb{R}^{N \times J}$, $i = 1, \ldots, n$, whose column $(\boldsymbol{W}_i)_j \in \mathbb{R}^N$ represents the muscle activation levels for the ith synergy at the jth time sample, that is,

$$\boldsymbol{w}_i(\tau_j) = \begin{cases} (\boldsymbol{W}_i)_j & 0 \leq \tau_j < t_{\max}, \\ \mathbf{0} & t \geq t_{\max}. \end{cases} \tag{3.2}$$

For a human motion trial with K samples, using (3.1) and (3.2), we write the muscle activation in matrix form as

$$\boldsymbol{M} = \boldsymbol{W}\boldsymbol{H} \tag{3.3}$$

where $\boldsymbol{M} = [\boldsymbol{a}_i(t) \ \dots \ \boldsymbol{a}_K(t)] \in \mathbb{R}^{N\times K}$ is the muscle activation matrix. Matrix $\boldsymbol{W} = [\boldsymbol{W}_1 \cdots \boldsymbol{W}_n] \in \mathbb{R}^{N\times nJ}$ represents the muscle activation levels over the trial. Matrix $\boldsymbol{H} \in \mathbb{R}^{nJ\times K}$ contains non-negative amplitude scaling factor c_i and time shift functions. Defining $\boldsymbol{C} = [c_1 \cdots c_n]^T \in \mathbb{R}^n$ for the amplitude vector, we denote

$$\boldsymbol{H} = \boldsymbol{C} \otimes [\boldsymbol{\Theta}_i(t)]_{i=1}^n, \tag{3.4}$$

where $\boldsymbol{\Theta}_i(t) \in \mathbb{R}^{J\times K}$ is used to shift the ith synergy at time τ_j $(1 - J \le j < K)$ and $(\boldsymbol{\Theta}_i(\tau_j))_{lm} = \delta(l, m - j)$ is expressed using Kronecker delta, which is defined as $\delta(p, q) = 1$ if $p = q$ and 0 otherwise. In (3.4), operator $\otimes$ represents a Kronecker product-like multiplication such that its block from $(j+1+(i-1)J)$th to the $(j+iJ)$th rows is given by $c_i\boldsymbol{\Theta}_i(t)$. The use of $\boldsymbol{\Theta}_i(\tau_j)$ contains all the possible time shift of synergy vector and the product of $\boldsymbol{W}$ and $\boldsymbol{\Theta}_i$ shifts of onset of the ith synergy by time t_i.

The optimal muscle activation achieves motion tasks in an efficient way to minimize human muscular effort. From (3.3), similar to [80], we define human effort E_h as $E_h = \sum_{k=1}^K \|\boldsymbol{a}_i\|_2^2$. To obtain the synergy onset timings t_is, synergy form $\boldsymbol{W}$, and amplitude vector $\boldsymbol{C}_t$ for human motion from training data, we formulate the following optimization to minimize muscle activation and reconstruction errors by (3.3) and (3.4).

$$\underset{\boldsymbol{W},\boldsymbol{C}_t,\{t_i\}}{\text{minimize}} \ E_h + \frac{1}{\eta}\|\boldsymbol{M} - \boldsymbol{W}\boldsymbol{C}_t \otimes [\boldsymbol{\Theta}_i(t)]_{i=1}^n\|_2^2, \tag{3.5}$$

where η is a regulation parameter. We use a similar method in [64] to solve the above optimization problem to determine the time-varying synergies using the data measure-

ments from motion trials.

To use the above synergy model to estimate human force in testing experiments, we assume that the synergy onset timings t_is (i.e., $[\boldsymbol{\Theta}_i(t)]_{i=1}^n$) and synergy form $\boldsymbol{W}$ are the same as those in the training trail motions. From [62], human force at end-effector is proportional to the muscle activation $\boldsymbol{M}$ and with (3.3) and (3.4), we have

$$\boldsymbol{f}_h = \boldsymbol{A}_F(\boldsymbol{q}_h, \dot{\boldsymbol{q}}_h)\boldsymbol{M} = \boldsymbol{A}_F(\boldsymbol{q}_h, \dot{\boldsymbol{q}}_h)\boldsymbol{W}\boldsymbol{C} \otimes [\boldsymbol{\Theta}_i(t)]_{i=1}^n, \tag{3.6}$$

where $\boldsymbol{A}_F(\boldsymbol{q}_h, \dot{\boldsymbol{q}}_h) \in \mathbb{R}^{3\times N}$ is the gain matrix that depends on model (2.2) and Jacobian matrix from the joint rates to the velocity of $\boldsymbol{O}$ [62], $\boldsymbol{q}_h = [\phi_1\, \phi_2\, \phi_3]^T$ is the human arm joint angle vector, $\boldsymbol{q}_h^d(t) = \mathrm{inv}(\boldsymbol{r}_r(t))$ is the human arm joint angle profile for target point trajectory $\boldsymbol{r}_r(t)$ in workspace, and $\mathrm{inv}(\cdot)$ is the inverse kinematic mapping of the two-link human arm.

We use force measurements $\boldsymbol{f}_h$ and synergy activation $\boldsymbol{M}$ from EMG measurements to estimate the value of $\boldsymbol{A}_F(\boldsymbol{q}_h, \dot{\boldsymbol{q}}_h)$ off-line by regression method (i.e., least-square). Multiple subjects data under various motion trajectories are taken from training the data collection process to cover the variety of synergies. With the known values of $[\boldsymbol{\Theta}_i(t)]_{i=1}^n$ and $\boldsymbol{W}$ that are obtained from (3.5), we use (3.6) to compute human force in real time provided at the synergy amplitude vector $\boldsymbol{C}$ is estimated. We will discuss how to predict $\boldsymbol{C}$ in Section 3.2.2.

Muscle co-contraction is a task-specific motor control strategy used by healthy individuals when performing complex multi-joint activities. To capture the muscle co-contraction into the human-manipulator control design, we take the similar approach in [81] and use the EMG signals to calculate a measure of co-contraction for each antagonistic pair. Using the formulation (3.1), the muscle activation level is defined as P_i and is expressed as

$$P_i = \frac{m_i^*}{m_i^{MVC}}, \tag{3.7}$$

where m_i^* is the activation of ith muscle and m_i^{MVC} is the maximum voluntary contraction that can be measured from the EMG. Then co-contraction level of each muscle pair (e.g., Biceps and Triceps Brachii), denoted as P_a and P_b, is found by taking the minimum level that both muscles are contracted to, namely,

$$P_{co} = \min\{P_a,\ P_b\}. \tag{3.8}$$

We will use the above muscle co-contraction level calculation in the human-manipulator control design in Section 3.3.

3.2.2 Human Force and Intention Motion Estimation

In order to use (3.6) to estimate human forces, we need to predict synergy activation level $\boldsymbol{C}$. We assume that human can reproduce their voluntary motion and force using same sets of synergies when given same target points. We would estimate the synergy coefficients by predict scaling factor $\boldsymbol{C}$ and consider synergy pattern matrix is fixed for similar motions. We construct $\boldsymbol{C}$ as the function of motion, that is, $\boldsymbol{C} = \boldsymbol{C}(\boldsymbol{q}_h^d, \boldsymbol{q}_h, \dot{\boldsymbol{q}}_h, \ddot{\boldsymbol{q}}_h)$. A neural network approach is used to estimate $\boldsymbol{C}$ in real time for human-manipulator interactions. Radial basis function neural networks are considered to obtain the predictions. The prediction output $\boldsymbol{\phi}(\boldsymbol{\Lambda}, \boldsymbol{\nu})$ of neural networks is expressed as

$$\boldsymbol{\phi}(\boldsymbol{\Lambda}, \boldsymbol{\nu}) = \boldsymbol{\Lambda}^T \boldsymbol{S}(\boldsymbol{\nu}), \tag{3.9}$$

where $\boldsymbol{S}(\boldsymbol{\nu}) = [s_1(\boldsymbol{\nu})\ \cdots\ s_p(\boldsymbol{\nu})]^T$, $s_k(\boldsymbol{\nu}) = \exp\left[\frac{-(\boldsymbol{\nu}-\boldsymbol{\mu}_k)^T(\boldsymbol{\nu}-\boldsymbol{\mu}_k)}{\eta_k^2}\right]$ is the base function, $k = 1, \ldots, p$, p is the total number of base functions, $\boldsymbol{\nu}$ is the input of the neural network, $\boldsymbol{\Lambda}$ is an adjustable weight vector, and $\boldsymbol{\mu}_k$ and η_k are constant parameters. To estimate $\boldsymbol{C}$ by (3.9), the inputs of the neural networks is $\boldsymbol{\nu}_{c_s} = [\boldsymbol{q_h}\ \dot{\boldsymbol{q}}_h\ \ddot{\boldsymbol{q}}_h\ \boldsymbol{q}_h^d]^T$, $i = 1, \ldots, L_f$, L_f is the size of training data set for intention force estimation, and $\boldsymbol{q}_h^d$ is the targeted arm motion profile.

As explained previously, human operators only know a set of target points $\boldsymbol{r}^d$, not the entire desired trajectory $\boldsymbol{r}_r$. Therefore, we use the neural networks approach above to obtain the estimate of human intention motion trajectory $\boldsymbol{r}_r$. To achieve such goals, we use and extend the approach in [17] to estimate intention motion $\boldsymbol{r}_r$ by the interaction force $\boldsymbol{f}_h$, actual end-effector position $\boldsymbol{r}$ and velocity $\dot{\boldsymbol{r}}$ and (discrete) target points $\boldsymbol{r}^d$. Therefore, we take $\boldsymbol{\nu}_r = [\boldsymbol{f}_{hi}^T \ \boldsymbol{r}_i^T \ \dot{\boldsymbol{r}}_i^T \ \boldsymbol{r}_i^d]^T$, $i = 1, \ldots, L_r$, L_r is the size of training data set.

In the training process for parameters $\boldsymbol{c}_s$ and motion trajectory $\boldsymbol{r}_r$, we conduct experiments to collect measurements of actual human arm motion trajectory, motion targets, and human-robot interaction forces. Human subjects conduct voluntary motion to follow a set of repeated simple curves such as lines, circles, and some known trajectories in workspace to collect training data. The training data inclues the stationary motion at the beginning and ending of each trial. The training motion trajectories are different with the validation motion. $\boldsymbol{\Lambda}$ are estimated and obtained for both neural networks models. In the predicting phase, the human applied force $\boldsymbol{f}_h$ and desired force $\boldsymbol{f}_h^d$ (by (3.6) with the actual and desired poses $\boldsymbol{q}_h$ and $\boldsymbol{q}_h^d$, respectively) and motion trajectory $\boldsymbol{r}_r$ are obtained by using (3.9). The training process is conducted off-line and the intention predictions are implemented in real time.

3.3 Human-Robot Interaction Control

Fig. 3.2(b) illustrates the schematic of human-robot interactions. The manipulator has three rotational joints on the vertical plane, while human arm has two rotational joint on on the vertical plane. Three synergies $\omega_1 \sim \omega_3$ are selected to generate human force.

The robotic manipulator is considered by a four-link (rotational) rigid body and the dynamics model is expressed as [68, 82]

$$\boldsymbol{M}_q \ddot{\boldsymbol{q}} + \boldsymbol{D}_q \dot{\boldsymbol{q}} + \boldsymbol{G}_q = \boldsymbol{J}^T \left(\boldsymbol{f}_{hr} + \boldsymbol{f}_l + \boldsymbol{f}_{dis} \right) + \boldsymbol{\tau}_{rob}, \tag{3.10}$$

where $\boldsymbol{q} = [\varphi_1 \ \varphi_2 \ \varphi_3 \ \varphi_4]^T$ is the joint angle vector, $\boldsymbol{M}_q$, $\boldsymbol{D}_q$, and $\boldsymbol{G}_q$ are the manipulator's inertia, Coriolis, and gravity matrices, respectively. The details of matrices are discussed in Appendix A. In (3.10), $\boldsymbol{f}_{hr}$ is the human applied force that will be discussed later in this section, $\boldsymbol{f}_l$ is the known load, $\boldsymbol{f}_{dis}$ is the unknown disturbance force, and $\boldsymbol{\tau}_{rob}$ is the robot input torque vector of the fully-actuated manipulator. $\boldsymbol{J}$ is the Jacobian matrix between the end-effector velocity $\dot{\boldsymbol{r}}$ and joint rate $\dot{\boldsymbol{q}}$.

Considering $\dot{\boldsymbol{r}} = \boldsymbol{J}\dot{\boldsymbol{q}}$ and $\ddot{\boldsymbol{r}} = \dot{\boldsymbol{J}}\boldsymbol{J}^{-1}\dot{\boldsymbol{r}} + \boldsymbol{J}\ddot{\boldsymbol{q}}$, we rewrite (3.10) into the end-effector motion as

$$\boldsymbol{M}_r\ddot{\boldsymbol{r}} + \boldsymbol{D}_r\dot{\boldsymbol{r}} + \boldsymbol{G}_r = \boldsymbol{f}_{hr} + \boldsymbol{f}_l + \boldsymbol{f}_{dis} + \boldsymbol{f}_{rob}, \tag{3.11}$$

where $\boldsymbol{f}_{rob} = \boldsymbol{J}^{-T}\boldsymbol{\tau}_{rob}$, $\boldsymbol{M}_r = \boldsymbol{J}^T\boldsymbol{M}_q\boldsymbol{J}$, $\boldsymbol{D}_r = \boldsymbol{J}^T(\boldsymbol{D}_q\boldsymbol{J} + \boldsymbol{J}^T\boldsymbol{M}_q\dot{\boldsymbol{J}})$, and $\boldsymbol{G}_r = \boldsymbol{J}^T\boldsymbol{G}_q$. Controlled manipulator force $\boldsymbol{f}_{rob}$ is to assist human to compensate for (known) load $\boldsymbol{f}_l$ and unknown disturbance $\boldsymbol{f}_{dis}$. The force sensor mounted at the end-effector directly obtains the measurement of the total force $\boldsymbol{f}_m = \boldsymbol{f}_{hr} + \boldsymbol{f}_l + \boldsymbol{f}_{dis}$.

The human applied force $\boldsymbol{f}_{hr}$ consists of the nominal force $\boldsymbol{f}_h$ and the reactive force $\boldsymbol{f}_r$ due to additional load and disturbance, namely,

$$\boldsymbol{f}_{hr} = \boldsymbol{f}_h + \boldsymbol{f}_r. \tag{3.12}$$

We use the neural network model (3.6) to obtain an estimate $\hat{\boldsymbol{f}}_h$ of $\boldsymbol{f}_h$. For reactive force $\boldsymbol{f}_r$ under disturbance, we use an impedance model that was developed in [83] to estimate its value. In [83], the estimated arm reaction force $\hat{\boldsymbol{f}}_r$ is modeled as a mechanical impedance force under perturbations, that is,

$$\hat{\boldsymbol{f}}_r = \boldsymbol{K}_h(\boldsymbol{q}_h^d - \boldsymbol{q}_h) + \boldsymbol{D}_h(\dot{\boldsymbol{q}}_h^d - \dot{\boldsymbol{q}}_h), \tag{3.13}$$

where $\boldsymbol{K}_h$ and $\boldsymbol{D}_h$ are the arm stiffness and damping coefficient matrices, respectively. From [81], the value of $\boldsymbol{K}_h$ is considered to be proportional to the muscle co-contraction

level P_{co} and $\boldsymbol{D}_h$ is assumed to be a constant. Therefore, we choose $\boldsymbol{K}_h = \lambda P_{co} \boldsymbol{I}_3$, where λ is a gain and $\boldsymbol{I}_n$ represents the $n \times n$ identity matrix. The values of λ and $\boldsymbol{D}_h$ are estimated by collected data during the experiment trials.

The control goal is to generate a desired admittance between human applied force $\boldsymbol{f}_h$ and the end-effector position $\boldsymbol{r}$ [84, 85]. Under $\boldsymbol{f}_h$ and a desired admittance model, the end-effector motion is obtained by

$$\boldsymbol{M}_d \ddot{\boldsymbol{r}} + \boldsymbol{D}_d \dot{\boldsymbol{r}} + \boldsymbol{K}_d \boldsymbol{r} = \boldsymbol{f}_h, \tag{3.14}$$

where $\boldsymbol{M}_d$, $\boldsymbol{D}_d$, $\boldsymbol{K}_d \in \mathbb{R}^{3\times 3}$ are (symmetric and positive definite) desired inertia, damping, and stiffness matrices, respectively. When robot dynamics (3.11) is known, the control input $\boldsymbol{u} = \boldsymbol{f}_{rob}$ is designed as

$$\boldsymbol{u} = \boldsymbol{f}_{rob} = -\hat{\boldsymbol{f}}_{hr} - \boldsymbol{f}_l + \boldsymbol{M}_r \ddot{\boldsymbol{r}} + \boldsymbol{D}_r \dot{\boldsymbol{r}} + \boldsymbol{G}_r - \boldsymbol{v}, \tag{3.15}$$

where $\hat{\boldsymbol{f}}_{hr} = \hat{\boldsymbol{f}}_h + \hat{\boldsymbol{f}}_r$ is the estimate of $\boldsymbol{f}_{hr}$, and $\boldsymbol{v}$ is the auxiliary control input that will be designed later in this section. Plugging (3.15) into (3.11), we obtain

$$\boldsymbol{f}_{hr} - \hat{\boldsymbol{f}}_{hr} + \boldsymbol{f}_{dis} - \boldsymbol{v} = 0$$

and then plugging into (3.14), we have

$$\boldsymbol{M}_d \ddot{\boldsymbol{r}} + \boldsymbol{D}_d \dot{\boldsymbol{r}} + \boldsymbol{K}_d \boldsymbol{r} = \hat{\boldsymbol{f}}_{hr} - \boldsymbol{f}_r + \boldsymbol{v} - \boldsymbol{f}_{dis}. \tag{3.16}$$

The human-robot interaction should have the desired admittance between the desired human force $\boldsymbol{f}_h^d$ and the reference motion $\boldsymbol{r}_r$, namely,

$$\boldsymbol{M}_d \ddot{\boldsymbol{r}}_r + \boldsymbol{D}_d \dot{\boldsymbol{r}}_r + \boldsymbol{K}_d \boldsymbol{r}_r = \boldsymbol{f}_h^d, \tag{3.17}$$

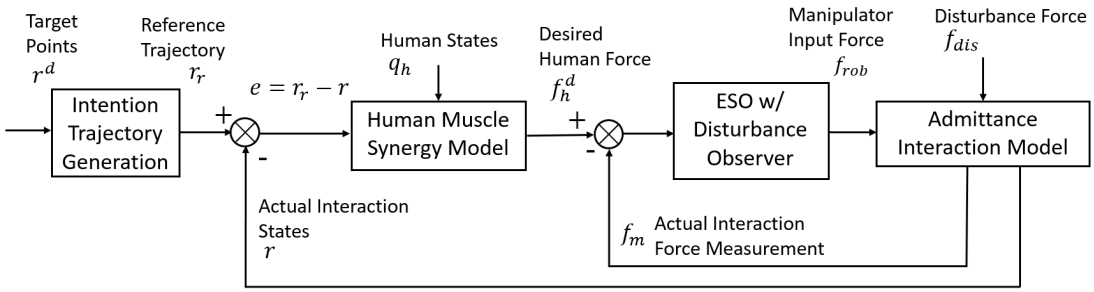

Figure 3.3: Schematic of the human-robot interactions control design.

where $\boldsymbol{f}_h^d$ is desired human force and $\boldsymbol{r}_r$ is the end-effector position reference. Defining error $\boldsymbol{e} = \boldsymbol{r}_r - \boldsymbol{r}$ and using (3.16) and the above equation, we obtain the position error dynamics as $\boldsymbol{M}_d\ddot{\boldsymbol{e}} + \boldsymbol{D}_d\dot{\boldsymbol{e}} + \boldsymbol{K}_d\boldsymbol{e} = -\hat{\boldsymbol{f}}_{hr} + \boldsymbol{f}_h^d + \boldsymbol{f}_r - \boldsymbol{v} + \boldsymbol{f}_{dis}$ and then

$$\boldsymbol{f}_{dis} = \hat{\boldsymbol{f}}_{hr} - \boldsymbol{f}_h^d - \boldsymbol{f}_r + \boldsymbol{M}_d\ddot{\boldsymbol{e}} + \boldsymbol{D}_d\dot{\boldsymbol{e}} + \boldsymbol{K}_d\boldsymbol{e} + \boldsymbol{v} = \boldsymbol{g} + \boldsymbol{v}, \tag{3.18}$$

where $\boldsymbol{g} = \hat{\boldsymbol{f}}_{hr} - \boldsymbol{f}_h^d - \boldsymbol{f}_r + \boldsymbol{M}_d\ddot{\boldsymbol{e}} + \boldsymbol{D}_d\dot{\boldsymbol{e}} + \boldsymbol{K}_d\boldsymbol{e}$.

We design a manipulator controller to assist human achieving desired interaction admittance along the trajectory and reject disturbances. Fig. 3.3 illustrates the control design structure. The controller is built on an extended state observer (ESO) to maintain the human desired force and reject the disturbance, while at the same time to reduce position error along the desired trajectory. We estimate the disturbance force $\boldsymbol{f}_{dis}$ and then the controller is used to compensate for its impacts. To design an ESO, we first introduce state variables $\dot{\boldsymbol{x}}_1 = \boldsymbol{f}_{dis} \in \mathbb{R}^3$, $\boldsymbol{x}_2 = \boldsymbol{g} \in \mathbb{R}^3$, and then write (3.18) into an extended state space form [86]

$$\dot{\boldsymbol{x}}_1 = \boldsymbol{x}_2 + \boldsymbol{v},\ \dot{\boldsymbol{x}}_2 = \dot{\boldsymbol{g}},\ \boldsymbol{y} = \boldsymbol{x}_2, \tag{3.19}$$

Using (3.19), an ESO is constructed as follows.

$$\dot{\boldsymbol{z}} = \begin{bmatrix} \boldsymbol{0} & \boldsymbol{I}_3 \\ \boldsymbol{0} & \boldsymbol{0} \end{bmatrix} \boldsymbol{z} + \begin{bmatrix} \boldsymbol{I}_3 \\ \boldsymbol{0} \end{bmatrix} \boldsymbol{v} + \boldsymbol{L}(\boldsymbol{y} - \hat{\boldsymbol{y}}),\ \hat{\boldsymbol{y}} = \boldsymbol{z}_2, \tag{3.20}$$

where $\boldsymbol{z} = [\boldsymbol{z}_1^T\ \boldsymbol{z}_2^T]^T \in \mathbb{R}^6$ is the estimate vector of $\boldsymbol{x} = [\boldsymbol{x}_1^T\ \boldsymbol{x}_2^T]^T$, $\hat{\boldsymbol{y}}$ is the estimate of $\boldsymbol{y}(t)$ by using $\boldsymbol{z}$ and $\boldsymbol{L} = \boldsymbol{L}_l \otimes \boldsymbol{I}_3$ is the observer gain vector, $\boldsymbol{L}_l = [\boldsymbol{l}\ \boldsymbol{l}]$, $\boldsymbol{l} = [l_1\ l_2]^T$. The values of l_1 and l_2 are chosen such that the observer poles are placed at $-\omega_0$ ($\omega_0 > 0$), namely, $s^2 + l_1 s + l_2 = (s + \omega_0)^2$.

With the proper ESO design, the estimate of $\boldsymbol{z}$ converges to an neighborhood of $\boldsymbol{x}$ if $\|\dot{\boldsymbol{g}}\|$ is small. A PD control structure is designed for the auxiliary input $\boldsymbol{v}$ in (3.15) to drive $\boldsymbol{z}$ to zero, namely,

$$\boldsymbol{v} = \boldsymbol{k}_p(-\boldsymbol{z}_1) + \boldsymbol{k}_d(-\boldsymbol{z}_2), \tag{3.21}$$

where $\boldsymbol{k}_p$ and $\boldsymbol{k}_d$ are the positive gain matrices. The stability of the controller design is obtained through the separation principle of the linear systems for (3.20) under the approximation $\dot{\boldsymbol{g}} \approx \boldsymbol{0}$. If $\dot{\boldsymbol{x}}_2 = \dot{\boldsymbol{g}}$ is bounded around zero uniformly, we can show that $\|\boldsymbol{z} - \boldsymbol{x}\|$ and $\|\boldsymbol{z}_2\|$ is bounded around zero closely as $t \to \infty$. Then $\|\hat{\boldsymbol{f}}_{hr} - \boldsymbol{f}_h^d - \boldsymbol{f}_r + \boldsymbol{M}_d\ddot{\boldsymbol{e}} + \boldsymbol{D}_d\dot{\boldsymbol{e}} + \boldsymbol{K}_d\boldsymbol{e}\|$ is bounded around zero, and thus, accordingly both force $\|\hat{\boldsymbol{f}}_{hr} - \boldsymbol{f}_h^d - \boldsymbol{f}_r\|$ and position $\|\boldsymbol{e}\|$ are bounded around zero.

3.4 Experiments

3.4.1 Experimental Setup

Ten subjects were recruited for experiments (nine male and one female, age: 28.4 ± 2.5 years, height: 172.1 ± 4.4 cm, weight: 71.3 ± 7.3 kg). The subjects were identified as healthy and capable to hold and move objects using upper-limbs. Fig. 3.2(a) shows the human upper-limb interactions with a 3-DOF manipulator (from Schunk GmhH & Co, Germany). In experiment, the subjects were trained to operate the manipulator by grasping the handle at the end-effector. The subject's hand can move freely with the end-effector handle and the manipulator was run under a compliance controller, denoted as *benchmark controller*, which is described in [69]. Under the benchmark control, the robotic manipulator follows human intention motion trajectory with a desired admit-

tance. One major difference of the proposed control with the benchmark controller is its capability to identify, estimate, and compensate for external disturbance forces such that subjects should be able to apply their nominal force in voluntary motion to accomplish the task. An informed consent form was signed by all the subjects and the testing protocol was approved by the Institutional Review Board (IRB) at Rutgers University.

The upper-limb movements were obtained by the motion capture system (7 Bonita cameras, Vicon, Inc., Oxford Metrics, Oxford, UK). The motion capture data were collected at 100 Hz. The human-robot interaction force was measured by a 6-DOF force sensor (model Mini45 from ATI Inc.) mounted at the end-effector. The force data was sampled at a frequency of 1000 Hz. The disturbance force was generated from a motor through a steel cable and in both the horizontal and vertical directions. The disturbance force was measured by a load cell (Model XTS4: S-Type from Load Cell Central) at a sampling frequency of 200 Hz. Both the benchmark and the proposed controllers were implemented and executed at a rate of 200 Hz. To estimate muscle synergies, a surface EMG system (MyoMuscle System from Noraxon Inc.) was used to measure the muscle activities and the EMG sampling rate was 1500 Hz. A total of eight muscle activities are measured by the EMG probes, including Brachialis (BRD), Biceps (BI), Medial triceps (MTRI), Lateral triceps (LTRI), Anterior deltoid (ADELT), Medial deltoid (MDELT), Posterior deltoid (PDELT), and Pectoralis major (PECT). The synergy activation and EMG data process were reconstructed through the non-negative factorization (NNMF) method [13].

3.4.2 Experimental Protocols

The subjects conducted manipulation experiments with the end-effector movement in both two-dimensional (2D) or three-dimensional (3D) spaces. In the 2D experiments, human subjects were instructed to guide the robotic end-effector in planar motion in the vertical plane; see Fig. 3.2(a). In experiments, the subjects' hand started at stationary,

and moved the end-effector to pass a set of given target points using their preferred motion and trajectory, and then stopped at the last point on the trajectory. The subjects were not asked to enforce precisely motion strictly. The manipulator passively follows human intention to reach the target points. Therefore, human motion in experiments was assumed as voluntary movement. The actual end-effector trajectory was shown on a computer monitor in front of the subjects and its actual position was also physically projected on a nearby paperboard by using a laser pointer mounted on the end-effector; see Fig. 3.2(a). Human subject's hand intention motion is estimated as described in section 3.2.2. If the subject's hand and intention was stationary at the starting and ending of the trail, the proposed controller didn't provide assistance. When the subject started their motion, the test trial was assumed to be continuous and non-stationary as the subjects were required to complete the trajectory and reach all the target points continuously. The subjects viewed the end-effector position in real time. The subject repeated the exact same task for multiple times and they also practiced several times before actual experiment. Fig. 3.4 shows the experimental setup for end-effector 3D movement. In 3D experiments, the subject moved the end-effector from the starting point and followed several target points. The target points were marked by small balls hanging in the workspace. The subject was instructed to move the handle and touch each ball by a certain sequence. The subject repeated the same movement for multiple times.

Disturbances were introduced and applied to the end-effector at random time in experiments. Under disturbances, two sets of experiments were conducted: human subjects tried to correct and overcome disturbance forces under the benchmark controller and the proposed controller. Each type of experiments was repeated for three trials and subjects took a brief rest (5-10 mins) between each trial. Before each trial, the subject was asked whether they feel tired or if they need additional rest to start the experiments. This practice would reduce or eliminate the negative effect of muscle fatigue and co-contraction. The subjects' ears were covered by a pair of earmuff during experiments.

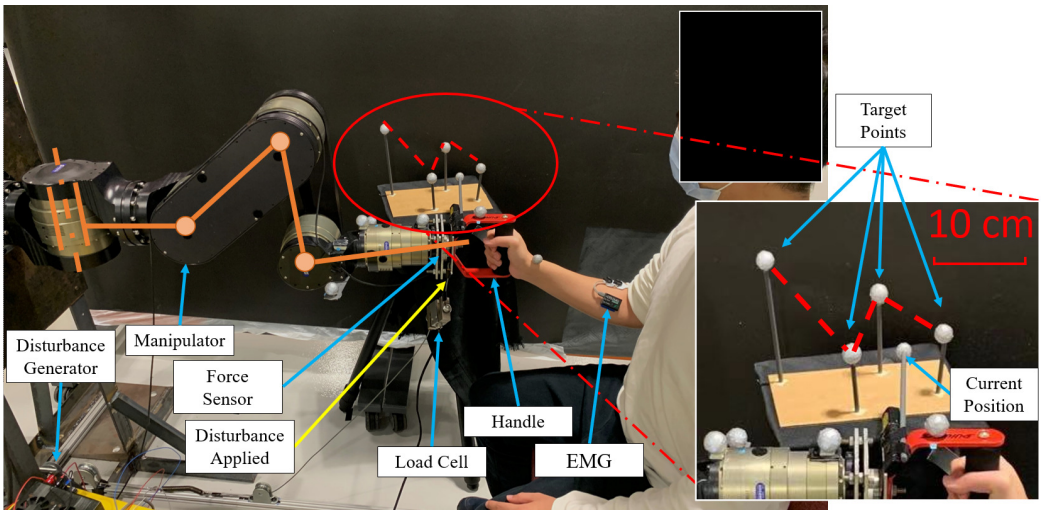

Figure 3.4: Experimental setup for 3D end-effector movement.

The earmuff can block human auditory sensing of the noises from generating the disturbance and thus, the disturbance was considered unexpected to the subjects.

Training data were from a set of repeated simple curves like lines, circles, rectangles and some known curves in a range of workspace including similar shape trajectories as the test experiments shown in Fig. 3.2(a). The validation and testing target points are chosen differently from the training data trajectories. The same target points are used to demonstrate the control performance under with and without disturbances cases for comparison purposes. The training trial length was selected to be similar with the testing trial lengths.

For both the proposed and benchmark controllers, the values of the desired admittance model parameters were chosen as $\boldsymbol{M}_d = 0.3\boldsymbol{I}_3$, $\boldsymbol{D}_d = 0.1\boldsymbol{I}_3$, $\boldsymbol{K}_d = \boldsymbol{0}_3$ in implementation. The following observer and control gain parameters were used in the ESO design, $l_1 = 1.1$, $l_2 = 0.3$, $\boldsymbol{k}_p = 2.3\boldsymbol{I}_3$, and $\boldsymbol{k}_d = 0.05\boldsymbol{I}_3$. These parameter values were chosen after multiple trials and tuning tests. The values of the kinematics and dynamics model parameters for the robotic manipulator were computed or measured using the three-link structure as shown in Fig. 3.2(b). With the recorded trajectory errors and forces during the different training trajectories, we used the least square method to esti-

mate parameters $\boldsymbol{K}_h$ and $\boldsymbol{D}_h$ in the impedance model (3.13). The co-contraction level was calculated from the activation of EMG sensors using (3.8). The co-contraction level from Biceps and Triceps were used as the major indicator of the co-contraction level for the trajectory due to its dominance as the reactive force in upper-limb motion. Only the segment when co-contraction level above a threshold was selected to calculate the gain λ (i.e., ratio between $\boldsymbol{K}_h$ and P_{co}).

3.5 Results and Discussion

3.5.1 Experiment Results

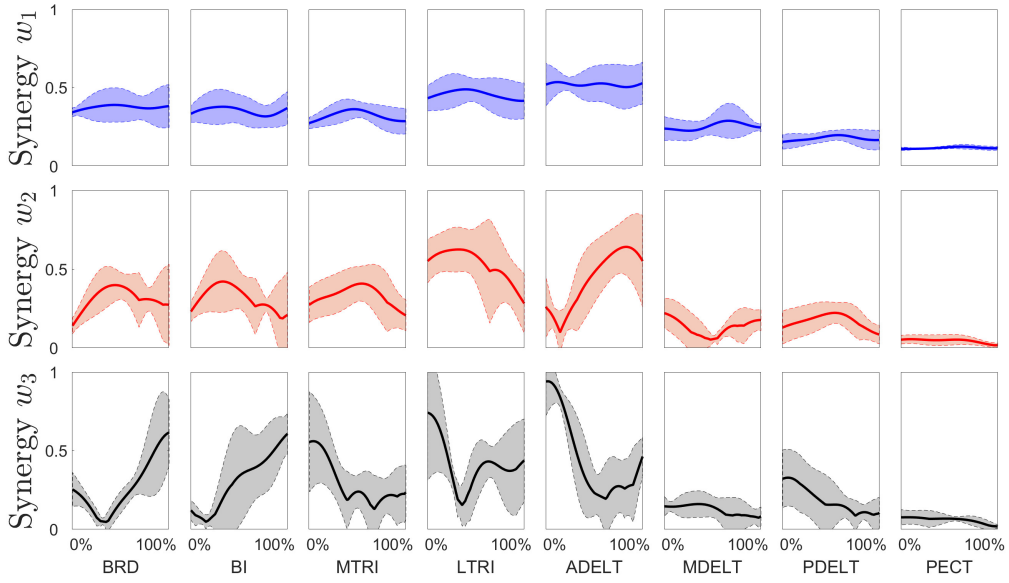

Figure 3.5: Time-varying muscle synergies ($\boldsymbol{w}_1$, $\boldsymbol{w}_2$ and $\boldsymbol{w}_3$) obtained from upper-limb movement. Each synergy contains eight muscle profiles: BRD, BI, MTRI, LTRI, ADELT, MDELT, PDELT, and PECT. The muscle activation variances of each synergy pattern are calculated from multi-subjects tests.

In 2D experiments, three synergies are selected for human upper-limb motion. We chose three synergies because they can reliably reproduce more than 90% of EMG activities [65] and therefore can capture arm muscle activities in planar motion in experiments. Fig. 3.5 shows the synergy patterns (i.e., denoted as $\boldsymbol{w}_1$, $\boldsymbol{w}_2$, and $\boldsymbol{w}_3$) as combination of several different muscle activity profiles. These synergies were extracted

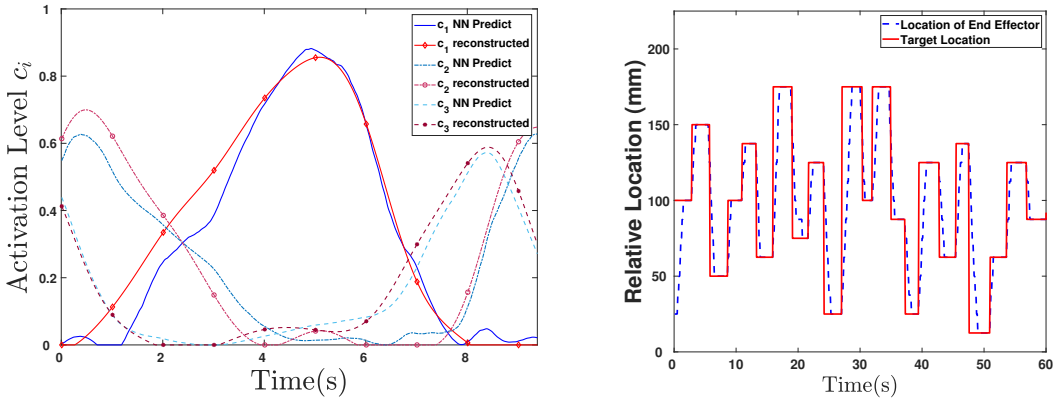

(a) (b)

Figure 3.6: (a) Human muscle synergy activation comparison by the neural network method and EMG-based reconstruction method. (b) Targeted and actual positions of the robot end-effector by one human subject (with human preferred speeds).

from the muscle group of eight muscles and each synergy contains a trail of muscle activation. The shaded areas in the figure indicate the variances of each muscle activation level. The initial delay t_i were assumed to be a constant and was taken from all the synergy pattern through all the subjects data. These synergy patterns are obtained by measuring all subjects experiments from the training data set discussed above. From the results as shown in Fig. 3.5, the average variances across all the muscles for synergies $\boldsymbol{w}_1$, $\boldsymbol{w}_2$ and $\boldsymbol{w}_3$ are 2.76%, 4.63% and 5.41%, respectively. The muscle synergy patterns are shown almost invariant across multiple subjects. This observation confirms that the same synergy pattern exists with a small variation among subjects. The variance might be due to the differences among the subjects' upper limb strength capability and biomechanic property.

Fig. 3.6(a) shows the synergy activation in an arm voluntary push motion along a straight-line. Three synergy activation levels are obtained and compared by the neural network and the EMG reconstruction methods. As shown in the figure, three synergy activation levels $c_i(t)$, $i = 1, 2, 3$, achieve their peak values at different time moments. For example, synergy $\boldsymbol{w}_1$ mostly contributes at the middle of the cycle and it is mainly

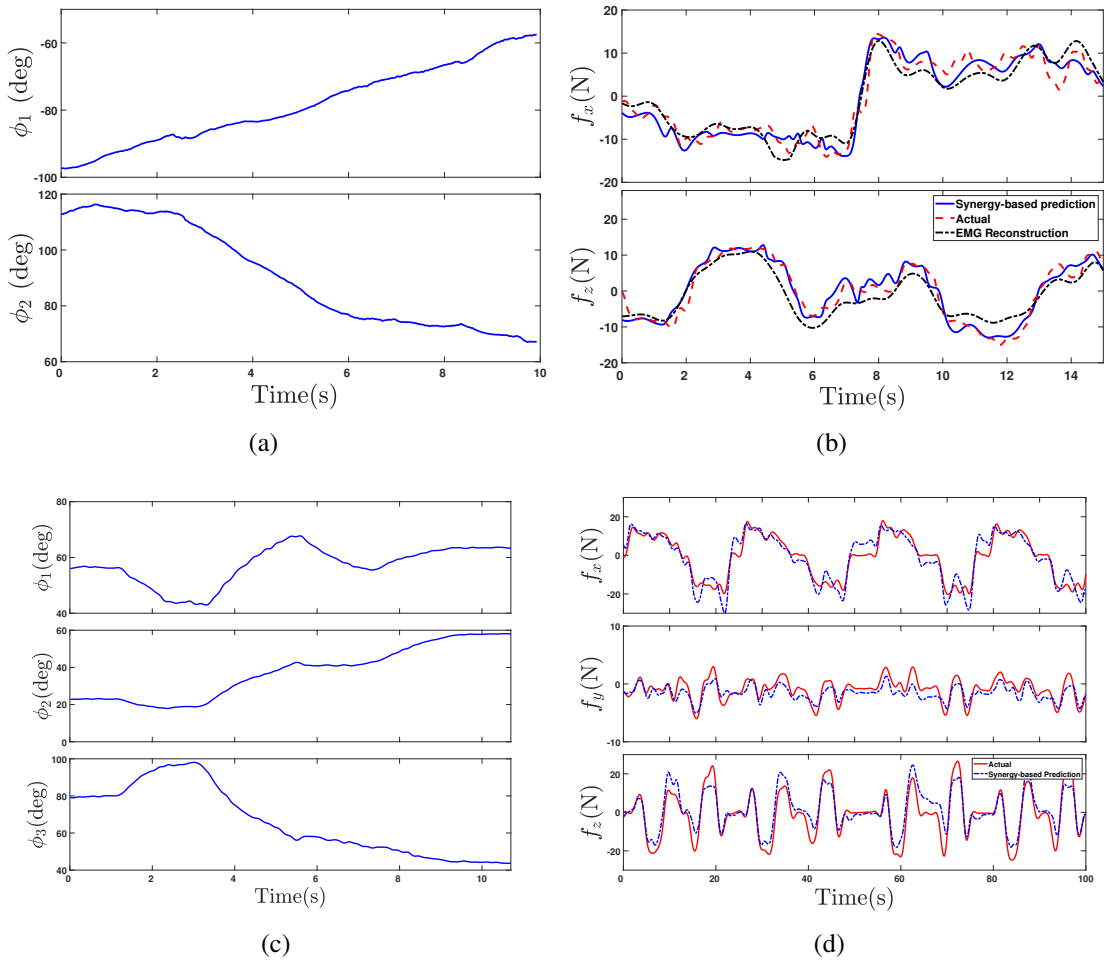

Figure 3.7: (a) The corresponding shoulder joint angle (ϕ_2 on the top plot) and elbow joint angle (ϕ_3 on the bottom plot) profiles in the 2D experiments. (b) Human force prediction comparison by the neural network-based synergy model, EMG-reconstructed method and actual force measurement. (c) The corresponding shoulder joint angle (ϕ_1 and ϕ_2 on the top and middle plot) and elbow joint angle (ϕ_3 on the bottom plot) profiles in the 3D experiments; see Fig. 3.2(b) for ϕ_1 and ϕ_2 definition. (d) In the 3D experiments, the predicted force comparison by the neural network synergy-based model and actual human force measurements.

related to arm extension motion. This observation implies that in the push task, $\boldsymbol{w}_1$ takes a major role. By using (3.6), each synergy pattern is associated with a base synergy force vector $\boldsymbol{A}_F$. The shaded area in the figure is the range of the base force vector over the entire joint angle profile. To further illustrate its dependency on joint angles, Fig. 3.7(a) shows the arm elbow and shoulder joint angles in the trail. Fig. 3.7(b) further shows the force comparison in the XZ-plane by the synergy-based prediction and actual

measurements by the force sensor. We also include the EMG-based reconstructed forces in the plot. The errors by the synergy model and the EMG measurements are less than 15.0% and 20.4%, respectively.

We further demonstrate human force prediction performance. Fig. 3.6(b) shows the actual end-effector trajectory and its target trajectory by one subject for a voluntary push movement along a straight-line. No disturbance force was applied in experiments. Fig. 3.7(d) shows the corresponding human actual applied force and synergy-based prediction force profiles. The results show that the prediction forces follow the actual human force closely. The maximum relative error between the prediction and actual forces is 14.6%. These results further confirm that the synergy model can predict human force in voluntary motion. Finally, Table 3.1 lists the root mean square (RMS) errors for the force and motion trajectory predictions from all subjects testing experiments. All these results demonstrate that the synergy-based force prediction is comparable with the EMG-based force reconstruction.

Table 3.1: Root mean square (RMS) errors for force and intention motion predictions from all subject testing experiments

NN predicted force (N)		Reconstructed force (N)		Predicted traj (mm)	
X-direction	Z-direction	X-direction	Z-direction	X-direction	Z-direction
3.2 ± 0.4	3.7 ± 0.3	5.1 ± 1.4	5.6 ± 1.4	3.0 ± 1.1	2.9 ± 0.5

Case I: Planar motion

With the synergy-based force and intention motion predictions, Fig. 3.8 demonstrates the control performance under external disturbance force. For comparison purpose, we also include the results under the benchmark controller, under which the robot follows human motion passively with a desired admittance. Fig. 3.8(a) shows the end-effector trajectory profiles along the X- and Z-direction. In the figure, four curves are plotted: nominal trajectory (black solid curves), neural network-based human intention mo-

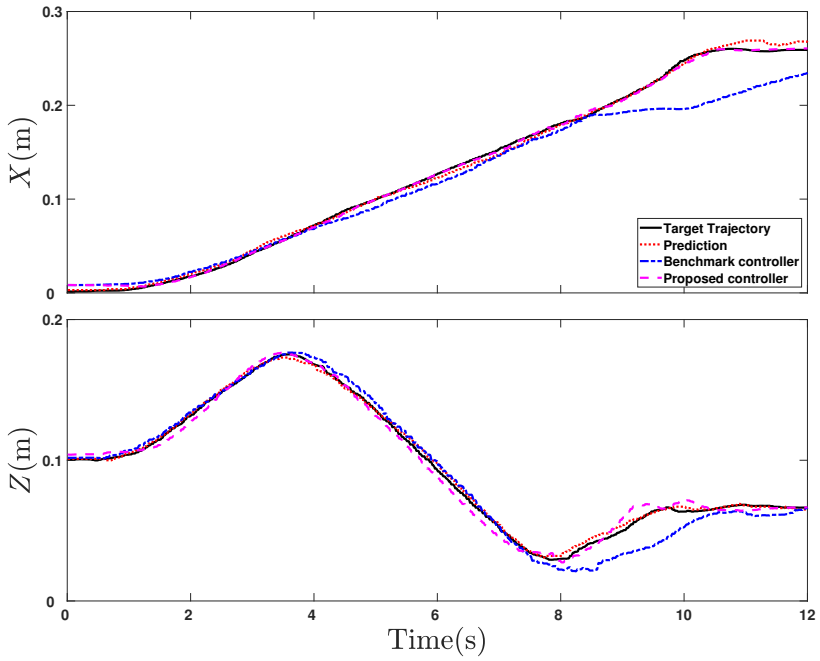

(a)

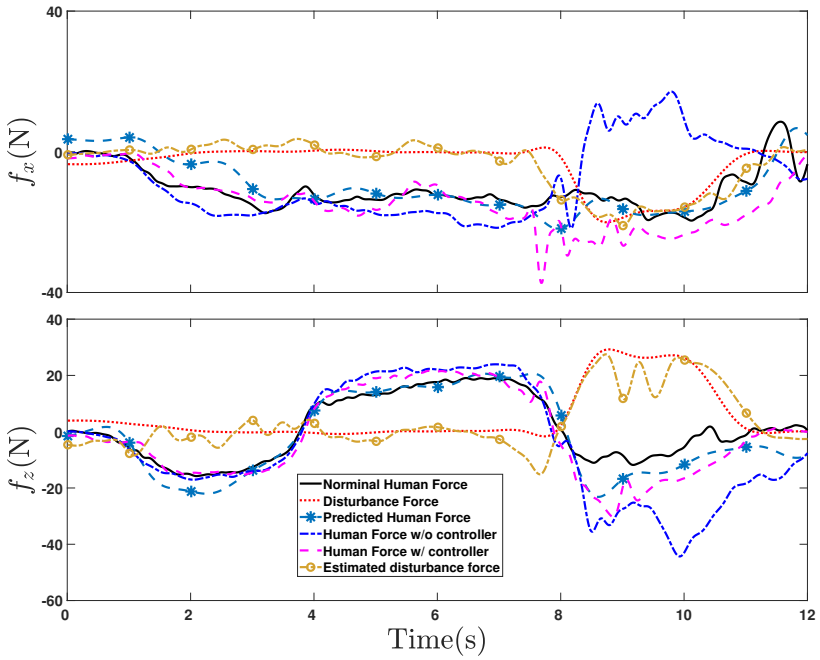

(b)

Figure 3.8: Experimental results under disturbance force by one subject. (a) End-effector motion trajectory. The top plot shows the trajectory in the X-direction and the bottom for the Z-direction. (b) Human and disturbance forces profiles at the end-effector. The top plot shows the force f_x along the X-direction and the bottom f_z for the Z-direction.

tion trajectory (red dotted curves), actual trajectories under the benchmark (blue dash-dotted curves) and the proposed controllers (magenta dash curves). Fig. 3.8(b) shows the corresponding human forces comparison in experiments. Besides the actual human forces under benchmark (blue dash-dotted curves) and the proposed controllers (magenta dashed curves), we also include the synergy model-based prediction force (light blue dash-starred curves), actual (red dotted curves) and estimate (orange dot-circled curves) of the disturbance forces in the figure. These forces are compared with the nominal human force (black solid curves) that is obtained under voluntary motion without any disturbance. The trajectory profiles in Fig. 3.8(a) confirm that the subject can control the end-effector reasonable well under disturbance force (initiated at around 7.2 s; see Fig. 3.8(b)).

Table 3.2: RMS errors for control performance comparison for all subject testing experiments of 2D experiments

Control methods	Human force (N)		End-effector position (mm)	
	X-direction	Z-direction	X-direction	Z-direction
Benchmark control	4.1 ± 5.7	5.7 ± 6.5	13.1 ± 4.7	10.5 ± 7.2
Proposed control	2.5 ± 2.4	2.6 ± 2.4	7.5 ± 4.4	6.1 ± 1.9

Fig. 3.9(a) further shows the statistics of the position errors of all subjects (using the nominal force obtained in experiments without disturbance as the reference). It is clear from these results that under the proposed control, both the position errors and variances are much smaller than these under the benchmark controller. The force control performance in Fig. 3.8(b) shows that under the benchmark controller, the human have to respond to the disturbance with large applied force and delay in both the X- and Z-direction. On the contrary, with the proposed control, the human force is much responsive and close to the nominal values. This is clearly shown in Fig. 3.9(b) which illustrates the force errors profiles of all subjects. Table 3.2 further lists the RMS errors for the trajectory tracking and human-robot interaction forces under the benchmark

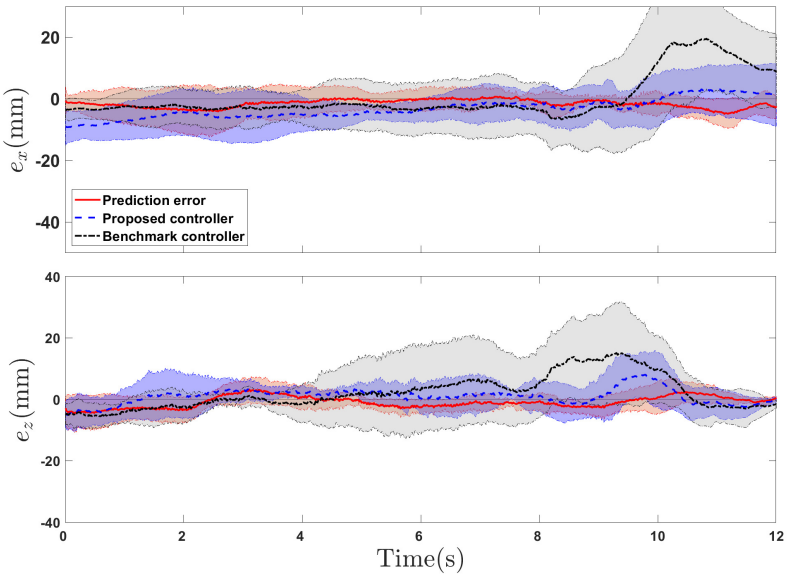

(a)

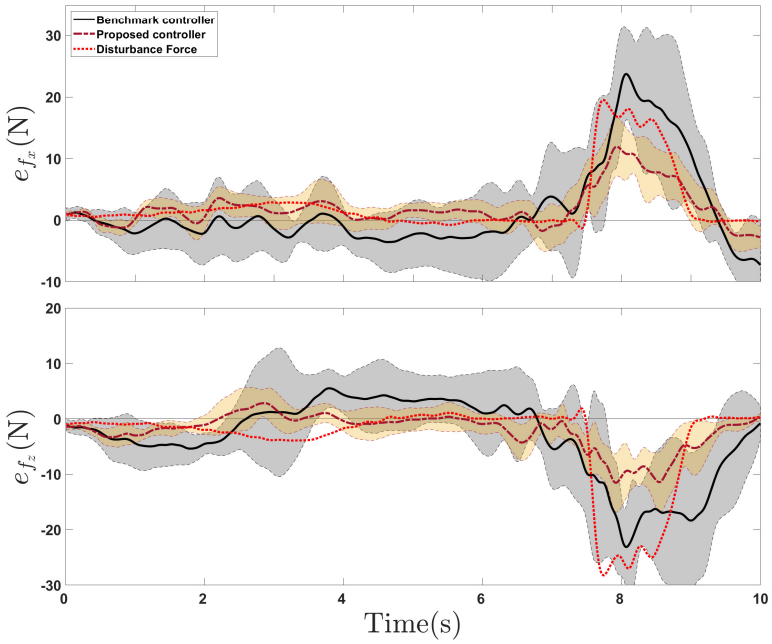

(b)

Figure 3.9: (a) End-effector motion trajectory error profiles comparison for all subjects. The top figure shows the X-direction position error e_x and the bottom for Z-direction position error profile e_z. The thick curves are the mean value profiles and the shaded areas show the one standard deviation around the mean values of all subject experiments. Same notation is used in all subigures. (b) Human force error profiles comparison for all subjects. The top figure shows the X-direction force error e_{fx} and the bottom for Z-direction force error profile e_{fz}.

and the proposed controllers for all subjects. The estimated disturbance force also follows the actual force closely. These results confirm about 50% error reduction under the proposed control comparing with the benchmark control. As shown in Figs. 3.7(d) and 3.8(a), the average delay of the robotic system responses is around 50 msec, and the end-effector tracking errors are around 3 mm, as illustrated in Table 3.1. These results also demonstrate that the control system enhances human comfort.

The above results do not include these with external load force $\boldsymbol{f}_l$. We conducted additional experiments with lifting a weight with $f_l = 9.8$ N (i.e., 1 kg) using the same experimental protocol. Fig. 3.10(a) shows the applied human and manipulator forces with and without the weight load. It is clear from these plots that with or without load $\boldsymbol{f}_l$, human forces were similar to conduct the same movement task. The additional load was carried by the robotic manipulator in the Z-direction (see the bottom plot in the figure). To demonstrate the effectiveness of the proposed control, we computed the human efforts E_h during the aforementioned experiments. The value of E_h represents the work conducted by human muscle activation during the arm motion. Fig. 3.10(b) shows the human effort comparison results. The plots include the statistical profiles of E_h by all subjects under the benchmark and the proposed controllers with disturbance, and also those under the benchmark controller without disturbance for comparison purpose. It is clearly shown by these results that under the proposed controller, the human effort under the disturbance (roughly from 6.5 to 8 s period) is much smaller than that under the benchmark controller. It is also interesting to observe that the proposed control renders the human effort (under disturbance) similar to the nominal profile (without disturbance). This implies that the proposed controller assisted human arm to perform similarly to the case without any disturbances. Fig. 3.10(b) also includes human effort results by the proposed controller with a weight load (1 kg). Same conclusion is obtained that the manipulator provides assistance such that the actual human effort is similar to these under the benchmark controller without weight load.

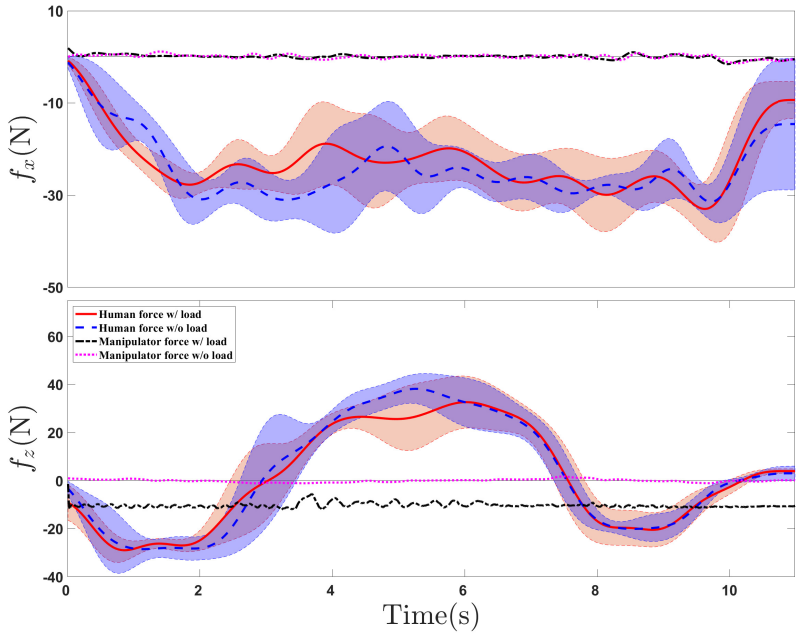

(a)

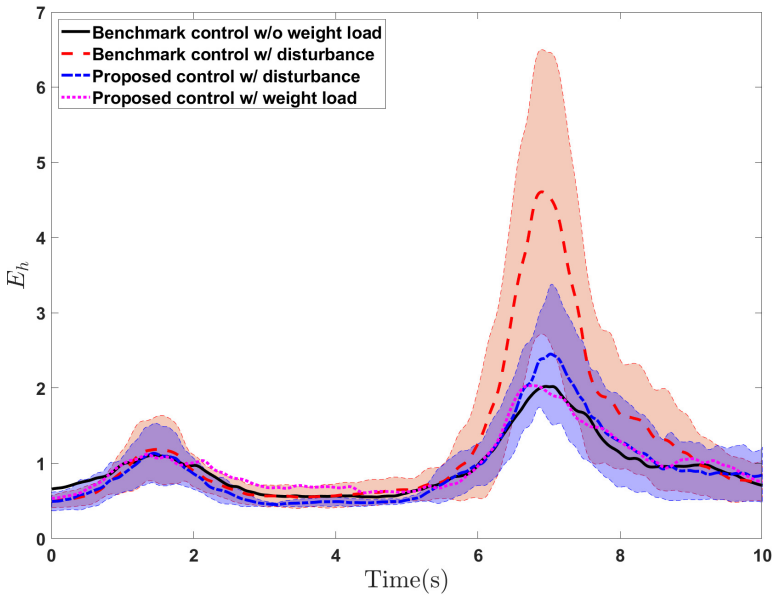

(b)

Figure 3.10: (a) Human force comparison with and without load for multiple subjects. The top figure shows the X-direction applied human and robotic forces and the bottom for the Z-direction forces. The thick curves are the mean value profiles and the shaded areas show the one standard deviation around the mean values of all subject experiments. The same notation is used in all subigures. (b) Human effort E_h comparisons under the benchmark and the proposed controllers. The results are obtained from all subject experiments.

Case II: 3D motion

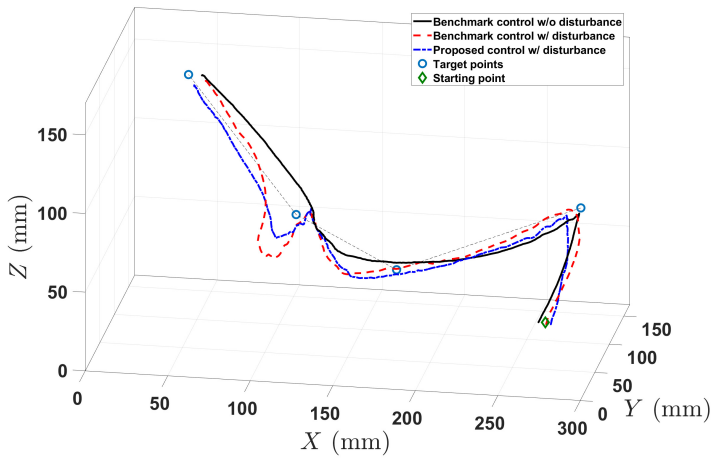

Figure 3.11: The 3D trajectory of the end-effector motion under disturbance force by one subject.

We further conducted experiments for 3D end-effector motion to validate and demonstrate the performance. Same numbers of synergies were selected for 3D experiments, which is assumed to be accurate due to the low movement speed in the lateral direction in current manipulator configuration. Fig. 3.11 shows the trajectory of 3D end-effector motion. This trajectory was chosen to mimic the motion of grit-blasting process. The subject started at the starting point (marked by the green diamond point) and then moved the manipulator to reach a few target points (marked by blue empty circles). The disturbance was applied at random point in the X- and Z-axis directions. We also plot the trajectories under the benchmark controller without disturbance (i.e., the black solid line) and with disturbance (i.e., the red dashed line) along with that under the proposed controller (i.e., the blue dash-dotted line). The trajectory under the benchmark controller deviated more further from the normal motion than that under the proposed controller.

The force control performance shown in Fig. 3.12(a) implies that comparing with the proposed controller, the human subject had to apply larger reaction force under the benchmark controller to overcome the disturbance in the X- Y- and Z-direction. This observation is also clearly shown in Fig. 3.12(b) that illustrates the force errors profiles

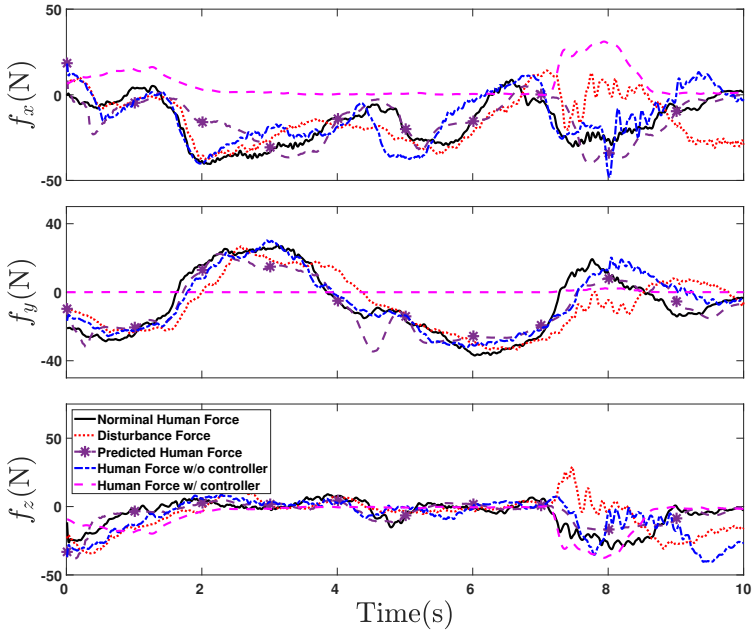

(a)

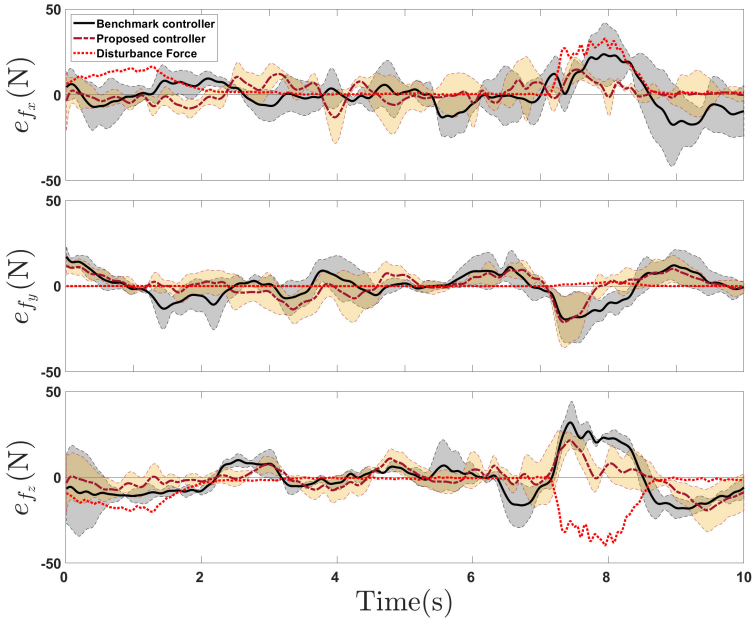

(b)

Figure 3.12: (a) Human and disturbance forces profiles at the end-effector. The top plot shows the force f_x along the X-direction, the medium plot shows the force f_y along the Y-direction and the bottom f_z for the Z-direction. (b) The top figure shows the X-direction force error e_{fx}, the medium figure shows the Y-direction force error e_{fy} and the bottom for Z-direction force error profile e_{fz}.

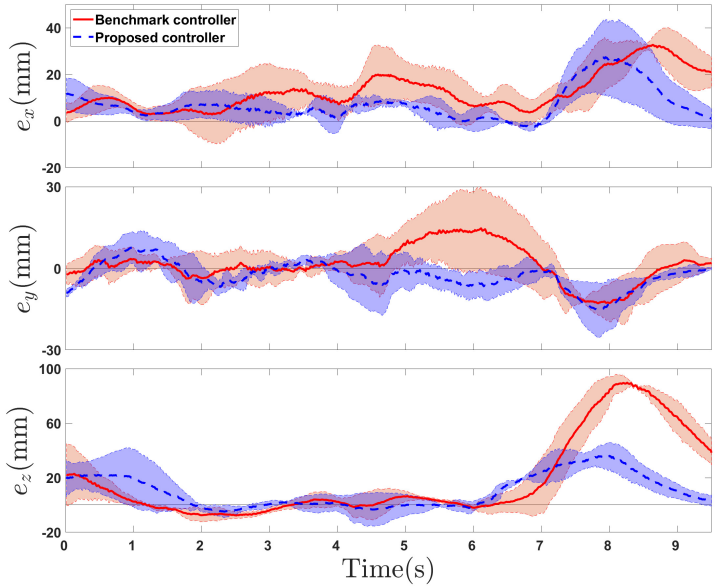

(a)

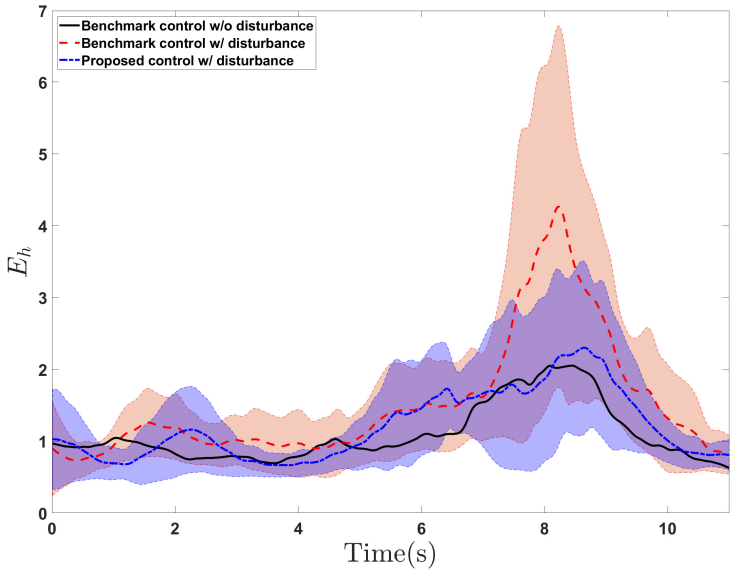

(b)

Figure 3.13: (a) End-effector motion trajectory error profiles comparison for all subjects. The top figure shows the X-direction position error e_x and the bottom for Z-direction position error profile e_z. The thick curves are the mean value profiles and the shaded areas show the one standard deviation around the mean values of all subject experiments. Same notation is used in all subigures. (b) Human effort E_h comparisons under the benchmark and the proposed controllers in the 3D experiments. The results are obtained from all subject experiments.

of all subjects. With the proposed control, the human force was much responsive and close to the nominal values. Similar to 2D experiments, Fig. 3.13(a) further shows the statistics of the position errors of all subjects (using the nominal force obtained in experiments without disturbance as the reference). When under disturbances (about 7 to 10 s), the position errors were smaller than those under the benchmark controller. We also computed the human efforts E_h in 3D experiments and Fig. 3.13(b) shows the human effort comparison results. The plots include the statistical profiles of E_h by all subjects under the benchmark and the proposed controllers with disturbance, and also those under the benchmark controller without disturbance for comparison purpose. It is clearly shown that under the proposed controller, the human effort under the disturbance (roughly from 7 to 10 s) was much smaller than that under the benchmark controller.

3.5.2 Discussion

In this chapter, with proposed model and controller, the reduction of human force error is about 50% for 2D case and 35% for 3D case under the disturbance force, which demonstrates the effectiveness of the proposed controller. In the 3D experiments, higher errors were observed in both human force and end-effector position errors in Table 3.3 compared with 2D case. This could potentially be due to the low resolution of the manipulator in the lateral direction and number of synergies which increases the possible errors from the estimation. In both 2D and 3D cases, Figs. 3.10(b) and 3.13(b) clearly show the reduction of human effort E_h during the trials with disturbance force applied under proposed controller. This observation implies that the proposed controller can potentially help reduce human applied force and effort in the above mentioned tasks.

The training data set for estimating muscle synergies contains different repeated motion patterns in the workspace and we assume human use voluntary motions to accomplish the tasks. The muscle synergies were estimated from to approximate human natural arm movement and muscle activities. This may lead to one limitation of the

Table 3.3: RMS errors for control performance comparison for all subject testing experiments of 3D experiments

	Human force (N)		End-effector position (mm)	
Control methods	Benchmark	Proposed	Benchmark	Proposed
X-direction	6.5 ± 5.9	3.8 ± 3.4	12.6 ± 8.0	7.4 ± 6.8
Y-direction	6.0 ± 4.8	4.8 ± 4.2	4.8 ± 4.7	4.2 ± 3.4
Z-direction	9.0 ± 6.8	5.1 ± 4.7	20.4 ± 28.1	11.1 ± 11.2

chapter. We assume the subjects can reproduce their motion by repeating the same motion between given target points and they always use their voluntary motion to complete these motions when they use their self-selected movement speed. At the beginning and the ending of the trial, the intention of the movement from the subject was detected and the manipulator did not provide assistance when the subject's hand was stationary. Note that, with given target points, the subject's motion was continuous and was only stationary at the starting and ending positions. Another assumption is that when the disturbance and load force applied, the dynamic properties of the interactions can be modeled with the impedance model in (3.14). Thus with same dynamic model of the interaction, the same disturbance rejection controller can be applied for various disturbance and load forces.

Due to the hardware limitation, the movement speed of human arm in the lateral was slower compared with the other two directions which may results in the higher errors in 3D experiments. A further study is required for interactions between human and a more agile robot in 3D workspace.

3.5.3 Summary

In this chapter, we developed a muscle synergy-based force control of robotic manipulator for assist-as-needed physical human-robot interactions. The muscle synergy model and the neural network approach were used to predict the muscle activation and then

estimate human applied forces in human-robot interactions. A disturbance observer was designed to estimate the unknown external disturbance forces, and then an admittance control was applied to the manipulator to simultaneously follow human intention motion and to compensate for working load and undesired disturbances. The proposed force estimation did not need any EMG sensors, which was attractive in many physical human-robot interactions. We conducted multiple subjects experiments in both 2D and 3D workspace to demonstrate the assist-as-needed control performance and disturbance rejection.

Chapter 4

Postural Balance of Kneeling Gaits for Construction Workers

4.1 Introduction

In the construction industry, among all fatal injuries, roofer is the leading construction trade and has the fourth highest fatal work injury rate among all occupations [1, 87]. Roofers perform more than 66% of their working time in kneeling, crouching, stooping, or crawling postures or gaits at high elevation and inclined surfaces [3]. It is important to understand the human postural balance control of kneeling gaits on inclined and elevated surfaces and thus to possibly introduce interventions to prevent and mitigate fall risk.

Many environmental factors influence postural balance control of construction workers such as elevation, visual scenes, inclined and restricted support surfaces [87]. Although study of human quiet stance has been reported extensively (e.g., [23, 24]), limited research exist on postural control of kneeling gaits on elevated or inclined surfaces. In [25], quiet kneeling is studied and compared with the stance with eye-open and eye-closed. Center of pressure motion and power spectral density (PSD) are used as a means to identify the difference between kneeling and stance gaits. The results in [25] conclude that PSD under kneeling shows significant difference with stance and visual feedback plays a significant role on the Center of Pressure (COP) motion under kneeling gaits. However, neither elevation nor inclined kneeling surface was considered.

Understanding and studying postural balance of quiet stance on elevated and in-

clined surfaces have been reported [88, 89]. In [88, 89], virtual reality (VR) was used as a tool to generate the high elevation and environmental scenes since running human subject experiments in high elevation location is unsafe, inconvenient and expensive. No difference was reported among the experimental outcomes in terms of height effects on human quiet stance between real and VR environments. Indeed, virtual reality, augmented reality and mixed reality (MR) become an important emerging technology for construction safety and trade skills training [90, 91, 92]. For example, it is promising to use an integrated VR and motion capture devices to study social learning among construction workers for fall risk behaviors in high elevation [93].

In this chapter, we study the postural balance of kneeling gaits on inclined and elevated surfaces for construction workers. We use the MR setup to construct the high elevation and visual scenes while subjects conduct kneeling gaits on a real inclined roof surfaces. Wearable inertial measurement units (IMUs) are used to obtain the human upper truck acceleration to quantify the body sway in sagittal and frontal planes. Quiet stance is conducted and compared with the kneeling gait results. We also use the inverted pendulum model and neuro-controller to analyze the balance performance for both quiet stance and kneeling gaits. Optimization process of model parameters is performed for the individual test and results show close matching between the power spectral density of the experimental and model prediction center of pressures. The main contribution of this work lies in the use of MR and analytical models to study the postural balance of kneeling gaits on elevated and inclined surfaces. Comparing with the quiet stance, this work complements the existing results and studies by providing new results in kneeling gaits. Comparing with the kneeling studies in [25], we mainly focus on the influence of elevation and inclined surfaces on balance performance.

The remainder of the chapter is organized as follows. Section 4.2 introduces the MR-based experimental setup and protocols. In Section 4.3, we present the kneeling and quiet stance and neuro-control models. Experiments and results are discussed in

Section 4.4, before we summarize the concluding remarks in Section 4.5.

4.2 MR-Enhanced Balance Experiments

4.2.1 Experiment Design

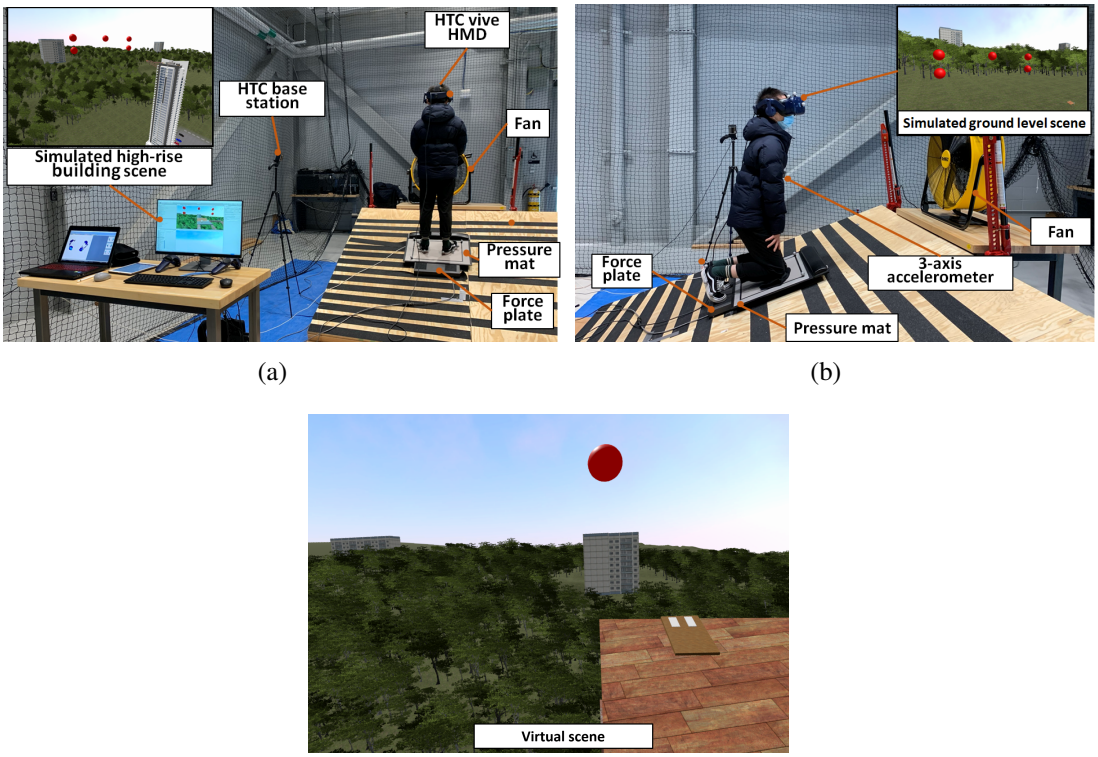

Figure 4.1: Mixed reality experimental setup on slope surface (a) standing, (b) kneeling. (c) The virtual scene that the subjects see in the VR headset.

We built an adjustable tilting virtual roof platform with wooden planks, which was combined with a VR system to build an MR environment. A backpack-type portable computer with HTC Vive Pro VR system was used in the experiments. With the backpack computer, the experimental system enables users to wear the equipment without tethering. The VR environment was built with the Unity game engine and it can stream subject's motion through motion tracking system. In order to provide a realistic virtual testing scenario, the spatial information of the room and simulated roof platform geometry were captured by a static LIDAR scanner. The virtual scenario on high (rooftop of a

high-rise 30th floor building) and low elevated surface (ground) were constructed. The VR world was aligned with physical environment before the start of each tests.

In the virtual environment, both high and low elevated surface scenes are simulated to provide the test subject with different virtual immersive experience. Fig. 4.1(a) shows the subject standing on top of the sloped rooftop platform while observing the simulated high-rise building scene. Fig. 4.1(b) shows the subject kneeling on sloped surface while observing the simulated ground scene. To simulate realistic high-rise building environment, a fan was placed in front of the subject to generate strong wind and wind noise sound was played from the headset. Different test conditions were combined and used such as standing/kneeling, level/sloped surface and high/low elevated virtual environment. Fig. 4.1(c) shows the virtual scene that the subjects see in the VR headset.

4.2.2 Experimental Protocol and Data Process

Three young male healthy subjects ($n = 3$, age: 28.3 ± 2.9 years, weight: 69.2 ± 13.8 kg, height: 169.3 ± 9.3 cm) with no known musculoskeletal or neurological defects were recruited for this study. All participants were informed about the testing protocol and signed the informed consent forms approved by the Institutional Review Board (IRB) at Rutgers University.

The participants were asked to perform quiet stance and kneeling tasks on a level (0 deg) and sloped (20 deg) surface. Visual perturbations were induced by changing the scene of the virtual environment. In addition, a sudden perturbation simulating strong wind conditions were induced using a strong fan aimed at subjects' upper trunk after first 30 sec of subjects balancing. Subjects were instructed to keep their balance and follow the visual tasks/targets (i.e., red dots in front of the subject) in the simulated environment. During tests, the subjects were instructed to kneel down or step on the force plate for each testing condition and keep their balanced for 60 sec. First 10 sec of data acquisition in each test were discarded. Overall, the subjects performed the

following tasks: standing or kneeling on 0 deg, and standing or kneeling on 20 deg.

In the experimental setup, x-, y-, and z-axis are defined as anterior-posterior (A-P), medial-lateral (M-L), and upward-downward (U-D) direction respectively. A 3-axis accelerometer (BWT901CL, WitMotion Inc.) was strapped on subjects' chest to record postural sway accelerations in the A-P, $\ddot{x}_{COM}$, and M-L, $\ddot{y}_{COM}$, directions. The portable force plate (Bertec Corporation.) and pressure mat (MatScan, Tekscan Inc.) were used to collect ground reaction forces/torques and pressure distribution measurements under feet on sloped and level surfaces. A motion capture system (8 Vantage cameras, Vicon Motion Systems Ltd.) was used to collect positions of subjects' feet and pressure mat. Data from all sensors was synchronized and collected at 100 Hz on a portable high-performance micro-processor (Intel NUC7i7DNK, Intel Corp.) through wireless connection.

Data from the force plate were used to evaluate the sway of the center of pressure in A-P and M-L directions, denoted as CP_x and CP_y, respectively. Several metrics were used to determine the postural balance stability. The power spectral density, root mean square (RMS), and mean velocity (MV) of CP_x and CP_y measurements were computed for all trials across all test conditions. The power spectrum density (PSD) was calculated using Welch method [25] with 2000 samples per periodogram and a spatial resolution of 0.05 Hz. The RMS was defined as $RMS = \sqrt{\frac{1}{N}\sum_{n=1}^{N} {x_i}^2}$, and MV was calculated as $MV = \frac{f_s}{N}\sum_{n=2}^{N}|x_i - x_{i-1}|$, where N is the number of samples of signal x_i and f_s is the sampling frequency. Characteristics of the postural sway using the accelerometer measurements, $\ddot{x}_{COM}$ and $\ddot{y}_{COM}$, were analyzed based on the 95% ellipse of postural acceleration sway [94] (major axis, minor axis, and sway area). The RMS of the $\ddot{x}_{COM}$ and $\ddot{y}_{COM}$ were computed to analyze the variability of corrective movement of the center of mass. In addition, we analyzed the experimental torque T_c measurements which were normalized with the body mass.

4.3 Neural Postural Balance Control

4.3.1 Neural Balance Controllers

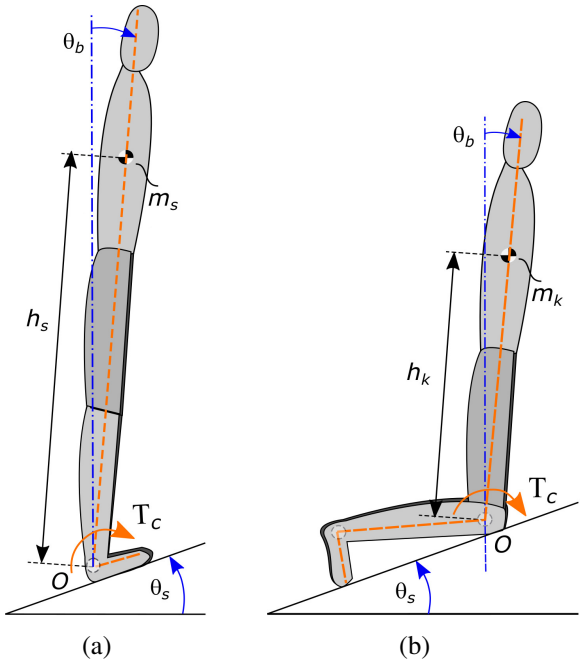

Figure 4.2: Inverted pendulum model for a) standing, b) kneeling on slope surface.

We consider an inverted pendulum model for human body sway in the sagittal plane during the quiet stance and kneeling balances. Fig. 4.2 shows the schematic of the inverted pendulum models for stance and kneeling gaits. The pendulums pivot around point O on the tilted surface. We denote the human body tilted angle and sloped angle as θ_b and θ_s, respectively. The distances from the human mass center to foot and knee are denoted as h_s and h_k, respectively. The mass and mass moments of inertia for stance and kneeling gaits are denoted as m_s and J_s, J_k, respectively. Fig. 4.3 illustrates the block diagram of the human postural neural balance control model. The model is adopted from the development in [25] and [24] for quiet kneeling and stance, respectively.

For inverted pendulum sway in the sagittal plane with small magnitude of θ_b, we

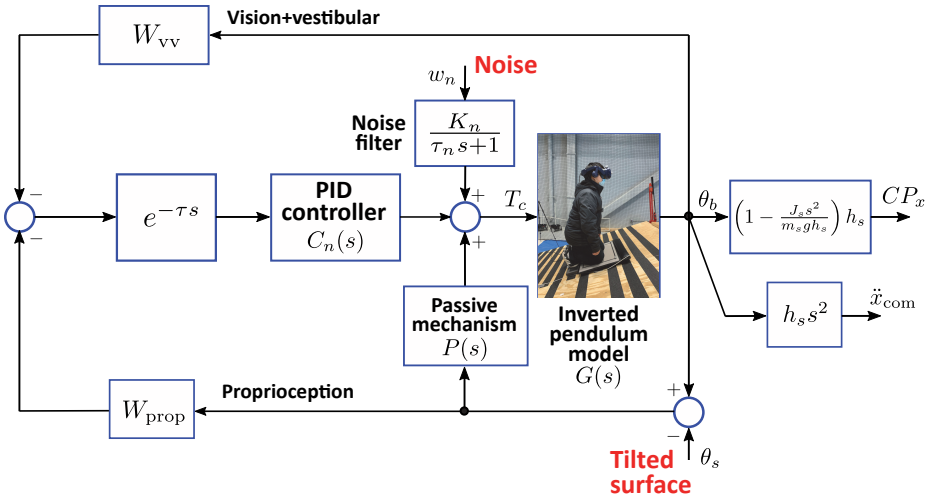

Figure 4.3: Block diagram of the human postural neural balance control model.

obtain the equation of motion as

$$J_s\ddot{\theta}_b + m_s g h_s \theta_b = T_c, \tag{4.1}$$

where T_c is the total torque applied on the human body. Denoting the positions of the mass center (COM) and COP in the horizontal plane as x_{com} and CP_x, respectively, we obtain

$$x_{\text{com}} = h_s\theta_b,\ CP_x = x_{\text{com}} + \frac{J_s}{m_s g h_s}\ddot{x}_{\text{com}}. \tag{4.2}$$

From (4.1) and (4.2), we obtain the transfer function from CP_x to θ_b as

$$\frac{CP_x(s)}{\Theta_b(s)} = \left(1 + \frac{J_s s^2}{m_s g h_s}\right) h_s. \tag{4.3}$$

For neural balance postural control, as shown in Fig. 4.3, we consider vision, vestibular and proprioceptive sensory feedback. The vision and vestibular sensory is considered into one feedback loop with a combined gain W_{vv}. The proprioceptive sensory feedback is modeled with gain W_{prop} and composite tilted angle $\theta_b - \theta_s$. The neural controller contains the time delay τ and the PID module $C_n(s) = K_p + K_d s + \frac{K_i}{s}$. The passive mechanism is modeled $P(s) = K_{ps}$. A colored noise is denoted as a filtering mech-

anism with white noise $w_n(t) \sim \mathcal{N}(0,1)$ with low-pass filter $\frac{K_n}{\tau_n s+1}$. From the neural balance control, we obtain the applied torque T_c as

$$T_c = \left(K_p + K_d s + \frac{K_i}{s}\right) e^{-\tau s}(W_{\text{prop}}\theta_s - \theta_b) + K_{ps}(\theta_b - \theta_s) + \frac{K_n}{\tau_n s + 1} w_n, \tag{4.4}$$

where we use model property $W_{\text{vv}} + W_{\text{prop}} = 1$ from [24].

4.3.2 Model Parameter Estimation

To estimate the model parameters, we need to compute the transfer function from $w_n(t)$ to outputs such as CP_x and $a_x := \ddot{x}_{\text{com}}$, which are measured by the force plates and the accelerometer on the upper body, respectively. From (4.1) to (4.4), we obtain

$$CP_x = \left(h_s + \frac{J_s s^2}{m_s g}\right)\theta_b,\ a_x = h_s s^2 \theta_b, \tag{4.5}$$

where $\theta_b = G_{w_n}(s)w_n + G_{\theta_s}(s)\theta_s$,

$$G_{w_n}(s) = \frac{K_n}{(\tau_n s + 1)\Phi(s)},\ G_{\theta_s}(s) = \frac{C_n(s)e^{-\tau s} - K_{ps}}{\Phi(s)},$$

and $\Phi(s) = J_s s^2 - (m_s g h_s + K_{ps}) + C_n(s)e^{-\tau s}$. We use the power spectrum of measured signal CP_x and a_x to estimate the model parameters. From (4.5), the power spectrum $S_{CP_x}(\omega)$ and $S_{a_x}(\omega)$ are given as

$$S_{CP_x}(\omega) = \left(h_s^2 + \frac{J_s \omega^2}{m_s g}\right)\|G_{w_n}(\omega)\|^2, \tag{4.6}$$

$$S_{a_x} = h_s \omega^2 \|G_{w_n}(\omega)\|^2. \tag{4.7}$$

Similar to the approach in [24] and [25], the model parameters are obtained by minimizing the following weighted errors between the model prediction and experimental data

at a selective frequencies, namely,

$$E = \sum_{i=1}^{N} \left| \frac{S_{CP_x}(\omega_i) - S^{exp}_{CP_x}(\omega_i)}{S^{exp}_{CP_x}(\omega_i)} \right| + r \left| \frac{S_{a_x}(\omega_i) - S^{exp}_{a_x}(\omega_i)}{S^{exp}_{a_x}(\omega_i)} \right|,$$

where $S_{CP_x}(\omega_i)$ ($S_{a_x}(\omega_i)$) and $S^{exp}_{CP_x}(\omega_i)$ ($S^{exp}_{a_x}(\omega_i)$) are the model-predicted and experimental power spectrum for CP_x (a_x) signals at frequency ω_i, respectively, N is the total number of selected frequencies, and $r > 0$ is a weight factor. To simplify the optimization process, we set weight constant r to be 0. In each optimization step, Fréchet distance was calculated between the simulated and the experimental PSDs.

4.4 Experimental Results

Fig. 4.4(a) shows the variation of the normalized CP_x during postural sway of one subject. Larger signal variations are clearly observed during stance on level or sloped surface, while variations during kneeling remain small. Fig. 4.4(b) shows the results of the PSD of the CP_x experimental data for stance and kneeling tests. The results are averaged across all the subjects for test conditions on level (0 deg) and sloped surface (20 deg) for low and high elevated MR scenes. Stance on level surface with shown low or high altitude MR scenes exhibit higher spectral density values compared to the ones observed during kneeling, regardless of the displayed visual scenes, see top figure of Fig. 4.4(b).

Comparing PSD of CP_x during stance on level surface (0 deg) shows higher values at frequencies below 0.3 Hz and higher area under the curve, when subjects were shown high elevated surface. These observations suggest less postural sway when observing high elevation visual scenes. Contrary, the higher PSD values of CP_x at frequencies between 0.3 and 0.6 Hz are observed when subjects were shown low level scene environment. The PSD results of CP_x for kneeling on the 20 deg sloped surface show similar trends as those observed on level surface. Surprisingly, the mean spectral density dur-

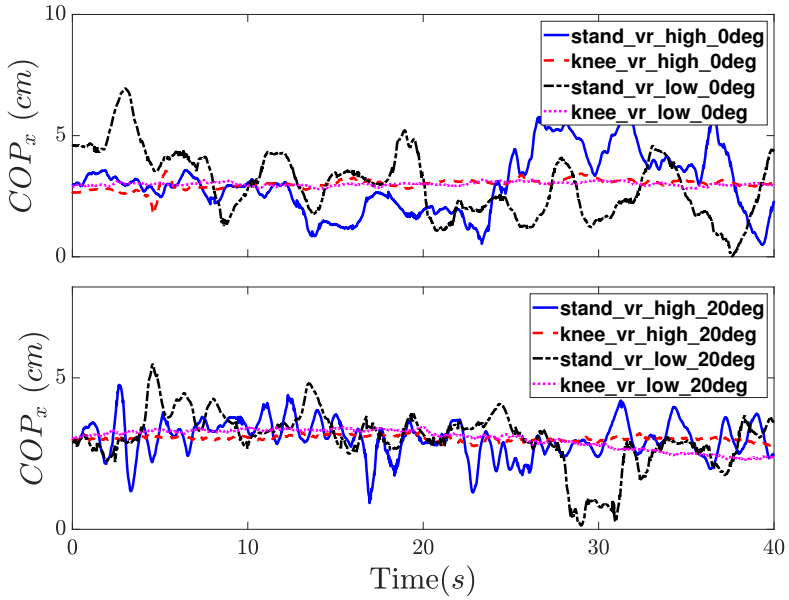

(a)

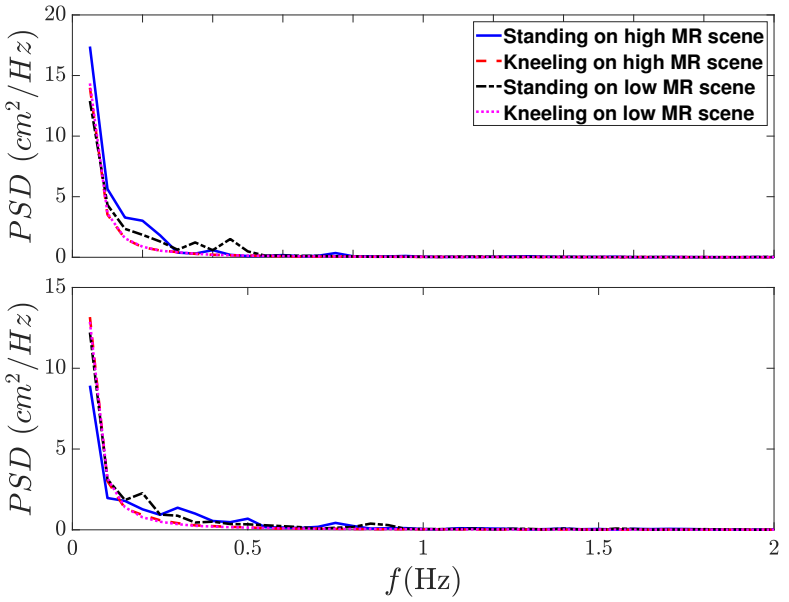

(b)

Figure 4.4: (a) COP in A-P direction of subject 2. (b) Power spectral density of experimental CP_x results averaged across all the subjects. As shown are results for standing and kneeling tests on level (0 deg, top figure) and sloped surface (20 deg, bottom figure) for low and high elevated MR scene.

ing stance on the 20 deg sloped condition exhibit lower values and lower area under the curve for frequencies below 0.3 Hz and higher area under the curve for frequencies between 0.3 to 0.6 Hz. These results suggest less sway during stance on a sloped sur-

face with the visual stimulus of high elevation working environment. This could be the result of the subjects applying corrective reactions to reduce sway and increase postural stability.

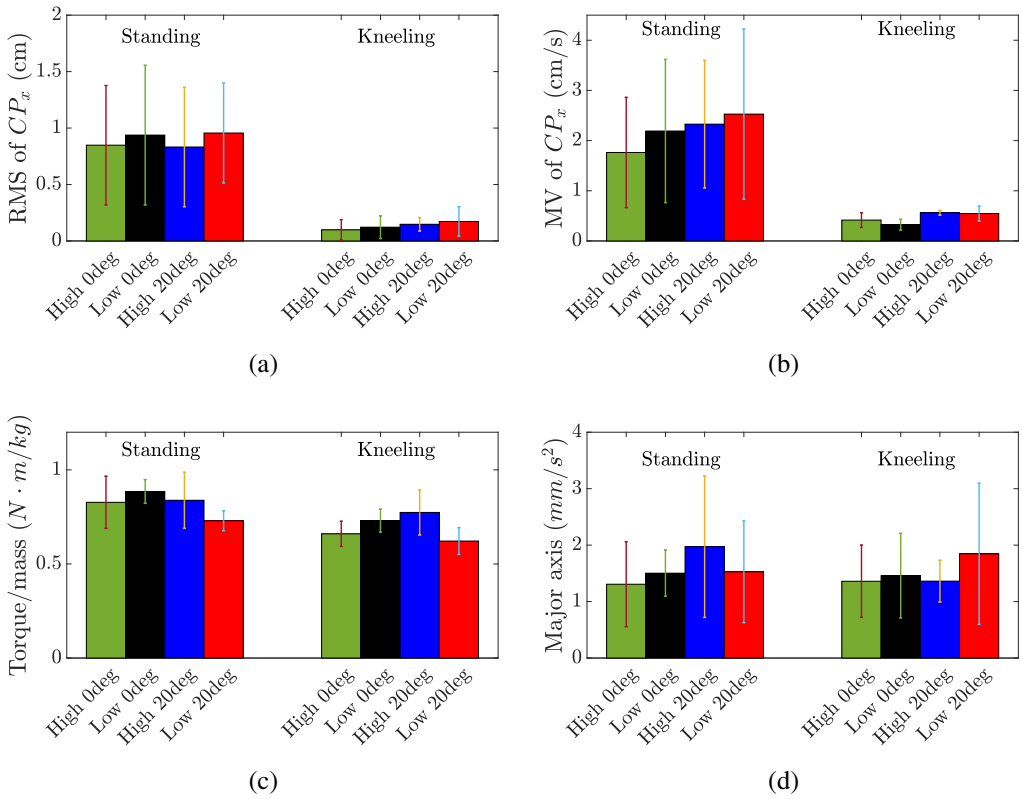

Figure 4.5: Results from standing and kneeling trials under various test condition with averaged values across all subjects of (a) average RMS of CP_x, (b) average MV of CP_x, (c) normalized torque values, and (d) major axis of the 95% ellipse of linear acceleration sway.

Fig. 4.5(a) shows the average results of the RMS of CP_x signals across all subjects. Higher RMS during all stance trials indicate higher variability in magnitude of the CP_x compared to all kneeling trials. Comparing RMS values during stance and kneeling trials individually, the results show the lowest RMS values during postural balance when high MR elevation scene was shown to the subjects. Observations of less postural sway of subjects during those trials imply that the subjects restricted their sway at high elevation as a consequence of the presence of a visual threat. The average results across all subjects of mean velocities of CP_x signal in Fig. 4.5(b) show higher values during

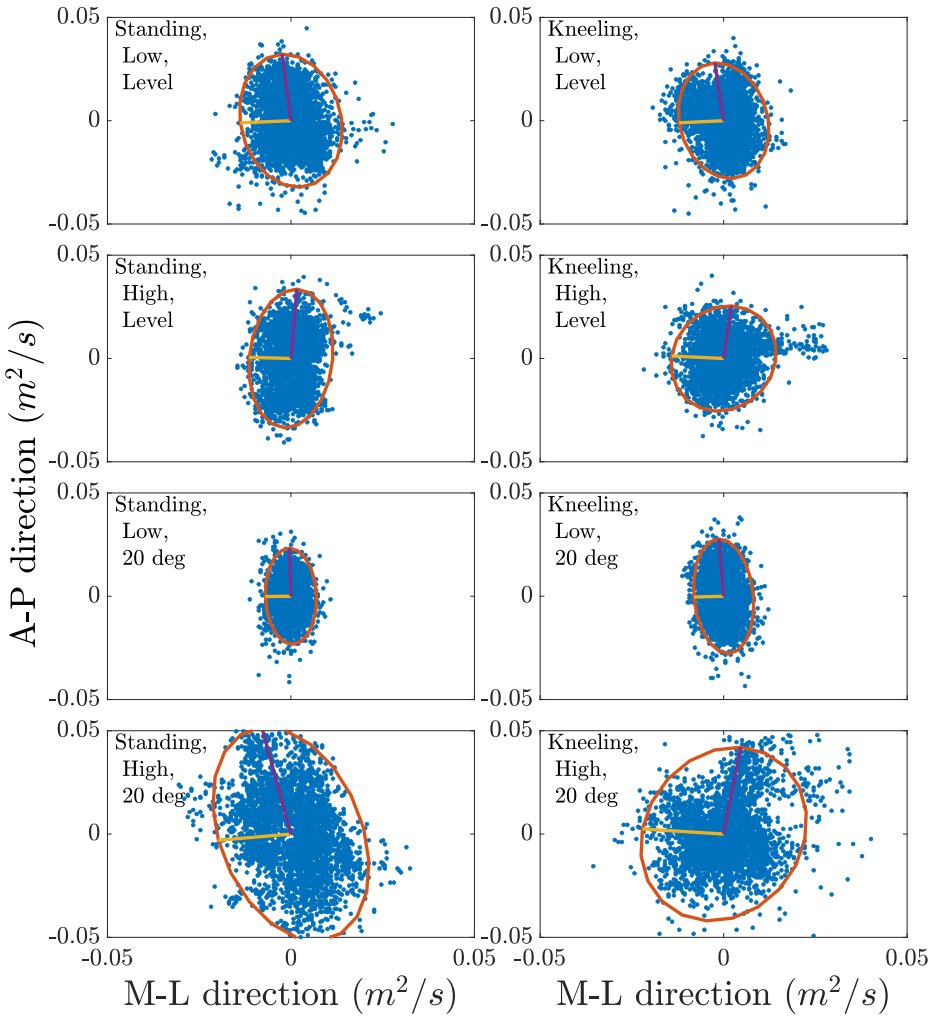

Figure 4.6: Results of the 95% ellipse of trunk linear accelerations in A-P and M-L directions during postural balance shown for all test conditions during kneeling and standing.

stance compared to kneeling across all test conditions. The comparison of mean velocity values among kneeling trials shows the highest mean velocity during kneeling on a flat surface with low MR environment scene. During stance, mean velocities of CP_x increase with increase of the slope of the supporting surface regardless of the displayed low/high environmental scene. The results of the normalized torques exerted on the force plate during postural balance are shown in Fig. 4.5(c). All normalized torque values during kneeling are lower compared to those during stance across same test conditions. Normalized torques during stance or kneeling on 20 deg sloped surface exhibit

the lowest values across all test conditions.

Fig. 4.6 shows the trunk linear accelerations in A-P and M-L directions during postural balance. The major axes with variance of the 95% ellipse of the postural sway accelerations are shown in Fig. 4.5(d). The smallest ellipse (i.e., major and minor axes) of the postural sway accelerations is observed during kneeling with shown low elevation in the MR immersion environment. These observations are held for both level and sloped surface conditions. Contrary, the largest deviation across all tests is surprisingly for the kneeling tests with the high immersion environment on both level and sloped surfaces.

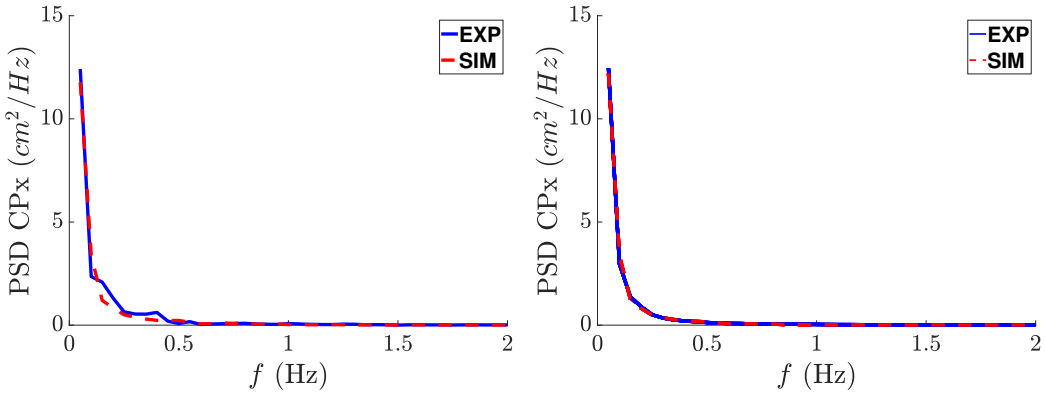

Figure 4.7: Comparison of the experimental and matching model prediction results of the PSD of CP_x for a) standing on 20 deg slope with low VR scene, b) kneeling on 20 deg slope with high VR scene.

Optimization process of model parameters was performed for the individual test of each subject. Figs. 4.7(a) and 4.7(b) show close matching between the PSD of the experimental and model prediction CP_x results for stance and kneeling tests, respectively. Both figures present results of one subject on level and sloped surfaces with low and high MR environmental scenes.

For the individual simulation condition, the model parameters of the neural control were obtained by optimization described in Section 4.3.2. Summary of the tuned model coefficients and their distributions for all the subjects obtained from the optimization

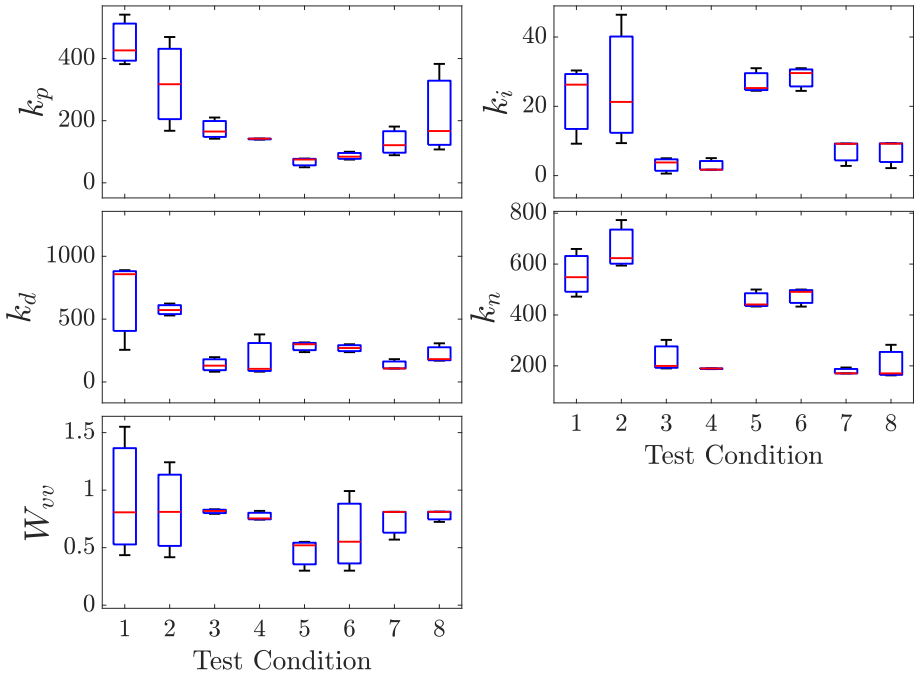

Figure 4.8: The parameters of standing and kneeling gaits were identified from simulation using the proportional-derivative neural controller. 8 test conditions are included as standing (condition $1 \sim 4$) and kneeling (condition $5 \sim 8$): Low, level surface; High, level surface; Low, 20 deg slope surface; High, 20 deg slope surface.

Table 4.1: Optimization Parameters for all the simulated conditions.

	k_p	k_i	k_d	k_n	W_{vv}
Standing, Low, Level surface	449.8	21.9	667.6	560.0	0.93
Standing, High, Level surface	318.0	25.7	575.1	663.5	0.82
Standing, Low, 20 deg slope	172.4	3.1	136.1	230.5	0.82
Standing, High, 20 deg slope	141.2	2.8	188.1	189.0	0.77
Kneeling, Low, Level surface	67.6	26.9	284.0	458.2	0.46
Kneeling, High, Level surface	86.3	28.4	269.0	474.6	0.61
Kneeling, Low, 20 deg slope	130.3	7.1	132.0	178.1	0.73
Kneeling, High, 20 deg slope	218.9	6.9	219.6	205.2	0.78

is shown in Fig. 4.8 and Table 4.1. Parameter optimization of the stance tests show a greater proportional control gain (k_p) on level surface than sloped surface while kneeling tests show an opposite trend. A clear and consistent increased trend is shown for the integral gain (k_i) on level surface compared to the ones used for the sloped surface.

Control parameters k_d and k_n exhibit a similar trend as that of the k_i, with increased values for trials on the level surface and one fold or two smaller values for trials on the 20 deg sloped surface. Finally, the coefficients related to visual and vestibular sensory feedback W_{vv} are all within a range above 0.7 except kneeling on level surface tests.

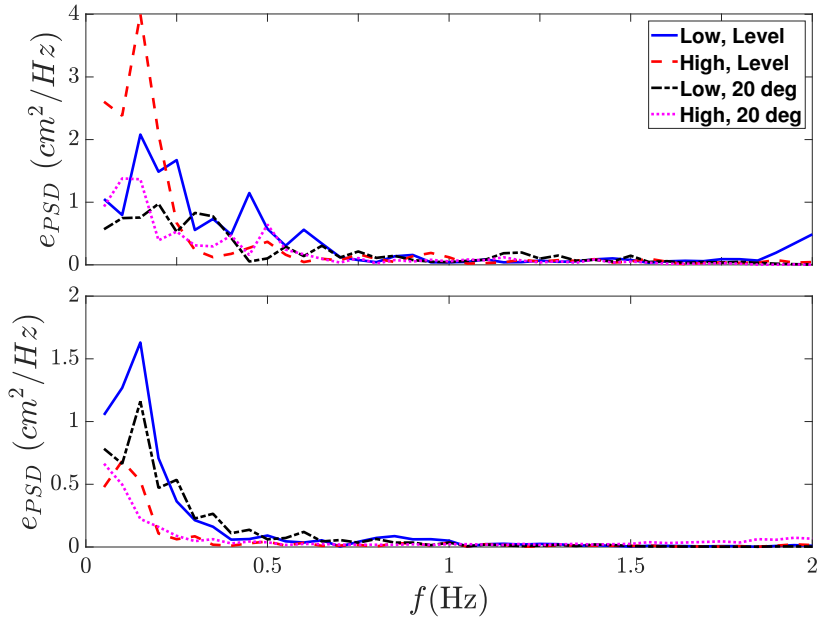

Figure 4.9: The error curves between experimental and simulated PSD plots are presented for both standing (top) and kneeling (bottom) gaits in various test conditions.

Fig. 4.9 shows that parameter optimization of kneeling tests has smaller errors than stance tests in general, which implies that the proposed model has a better fit for kneeling gaits. For the optimization of stance tests, a smaller error from experiments on the sloped surface than on the level surface is observed especially at lower frequency range. The error plots of kneeling tests show smaller values in the high elevated MR scenes than those under low elevated scenes.

Our results on kneeling tests show the subjects have a larger variance of center of pressure on both level and slope surfaces in the A-P direction. This suggests that subjects are more relaxed on the low/ground level surface than on the elevated surface. On the high elevation scene, the normalized torque has higher variances, which indicates that subjects used more variant torques to control their balance. The power spectral density

and RMS of center of pressure curves match with the results of previous study [25]. Comparison of center of pressure mean velocities showed several times higher values during stance than kneeling. These results contradict findings from previous study [25], where surprisingly a reverse trend was reported. The values of control gains k_p and k_d show similar decreasing trend as in [25] from stance to kneeling, however the noise gain k_n doesn't agree with the results, which also shows a decreasing trend in [25]. A small sample size might affect our results. Further studies are needed to explain these different trends.

4.5 Summary

In this chapter, we investigated the postural balance during kneeling and standing on sloped and elevated surfaces. A postural model was developed to simulate postural sway in the anterior-posterior direction. The model and controller parameters were optimized to precisely match the experimental results. Variation of model parameters with respect to particular test conditions provided insight on relationship on human neural balance postural control and sensory system. This work complements the existing research on the postural control during kneeling, which is of particular relevance for construction workers that commonly perform work on elevated and inclined surfaces.

Chapter 5

Wearable Knee Assistive Devices for Kneeling Tasks in Construction

5.1 Introduction

In the previous chapter, we discussed about human balancing modeling. With human modeling, control system for the exoskeleton can be design to help reduce WMSD risks in the construction. Construction workers regularly perform tasks that include repetitive kneeling down/ standing up and prolonged stationary kneeling on one or both knees on flat or inclined surfaces; see Fig. 5.1. Emerging technologies such as wearable robotics provide promising potentials to prevent WMSDs [95]. All industrial exoskeletons on the market (e.g., [96]) are passive and mainly for assistance in walking, lifting, and carrying gaits that are significantly different from kneeling tasks. One of the goals of this study is to develop a wearable sensing and assistive system to assist construction workers during kneeling tasks.

Biomechanical studies have shown that static deep knee flexion kneeling alters the walking gait knee joint kinematics and kinetics, suggesting that prolonged abnormal knee loading might lead to KOA [97, 98]. Using knee savers during deep flexion kneeling was recently suggested as a potential intervention to reduce the risk of musculoskeletal disorders [99]. Distribution of forces under the knees can be modified using proper knee-pads that results in decrease of knee disorder due to kneeling [100]. Compared with walking gait, the activity of proximal muscles during kneeling were shown to in-

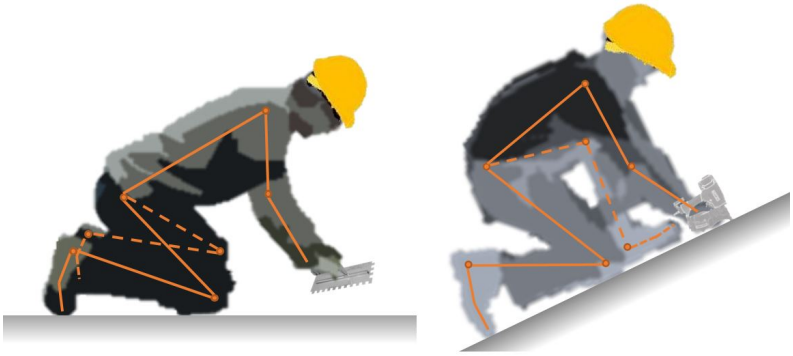

Figure 5.1: Examples of kneeling tasks for construction workers: (a) tile installer in double-leg kneeling and (b) roofer in single-leg kneeling on sloped surface.

crease [101]. The increased physiological demands and biomechanical loading deteriorate the comfort and lead to fatigue and injury risk of workers, which need to be minimized. Knee assistive exoskeleton can potentially reduce knee loading exposures, i.e., peak muscle activations and knee-ground contact pressures, and thus mitigate WMSD risks.

Wearable robotics is an active research field in human-robot interactions [8] and personalized technology for construction workers [102]. Real-time control of wearable robotics is challenging because of difficulty to predict human performance under dynamic variations and noises [103]. Impedance control is commonly used for human-robot interactions together with series elastic actuators (SEA) (e.g., [104]). Instead of using SEA, quasi-direct drive (QDD) actuation was recently developed to meet the high-torque, high-backdrivability, and high-bandwidth requirements [105, 29]. Comparing with many SEA-based robotic devices, lightweight QDD-based knee exoskeleton has demonstrated promising potentials for industrial applications.

In this chapter, we present a wearable mechatronic system that consists of active knee exoskeletons and a wearable sensing suite to assist construction workers in kneeling tasks. It is challenging to design a lightweight exoskeleton for kneeling tasks due to large knee flexion and required high assistive power. The knee exoskeleton is adapted from the previous design [39] with extended large assistive torques without increasing

additional weights and modified to wearable, nontethered configuration. We analyze the kneeling gait features on sloped surfaces. To enable real-time gait detection in kneeling tasks, a set of wearable inertial measurement units (IMUs) are used to identify various kneeling events (i.e., up, down, or stationary), types of kneeling (i.e., single- or double-leg), and kneeling with changes in trunk posture. Control of the exoskeleton device is based on the gravity compensation of the trunk and thighs to assist subject during kneeling down, standing up from kneeling position, or stationary kneeling. Human subject experiments validate the system design in assisting subject to perform required tasks. The main contributions of this work lie in the design and evaluation of the lightweight wearable sensing devices and knee exoskeletons for construction workers. New developments also include the control of the wearable device for construction workers on sloped and level surface during single- and double-leg kneeling and the feasibility demonstration of wearable assistive devices to reduce knee contact loads and muscle activation during kneeling tasks. To the authors' best knowledge, there is no reported study for use of passive or active exoskeletons in kneeling tasks. The design of flexible, lightweight, QDD-actuated exoskeleton enables feasible assistance in kneeling tasks.

The remainder of the chapter is organized as follows. Section 5.2 introduces the wearable mechatronic devices used in this study. In Section 5.3, we present the biomechanics model and control of exoskeleton for kneeling gaits. Experimental results and discussions are presented in Section 5.4. We finally summarize the concluding remarks in Section 5.5.

5.2 Wearable Systems for Kneeling Tasks

5.2.1 Wearable System Integration

We created a laboratory environment that mimicked setup of construction workers on level and sloped surfaces. Fig. 5.2 shows the wearable sensing and exoskeleton devices on a subject wearing a construction uniform. We constructed a wooden structure with

a variable surface slope and glued anti-skid tape. A level surface (0 deg), low-slope (10 deg), and conventional slope (20 deg) were used in the experiments to investigate a variety of common slopes of roof surfaces in construction [106].

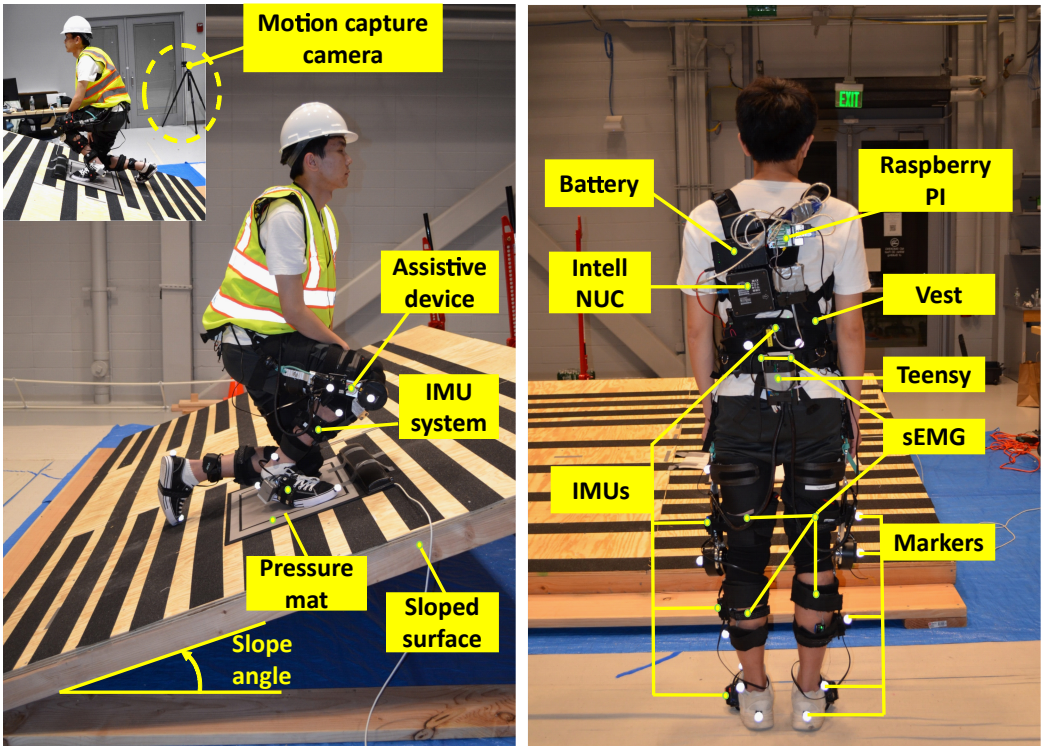

Figure 5.2: Laboratory environment mimicking construction setup with variable slopped wooden structure. Wearable sensor suit and stationary sensors were used in the experiments to measure subjects' kinematics and kinetics.

Fig. 5.3 shows overall schematics of the wearable mechatronic systems used in the experiments. All components were connected and synchronized through desktop computer and portable high-performance micro-processor (Intel NUC7i7DNK, Intel Corp.) through WiFi wireless connection. An optical motion capture system (8 Vantage cameras, Vicon Ltd) was used to collect whole-body ground-truth kinematics. A portable pressure mat (MatScan, Tekscan Inc.) was used to measure knee/foot contact pressures on level and sloped surfaces. The wearable systems included a bi-lateral knee assistive exoskeleton device [39] that provides assistive torque to the individual knee, IMU system (8 units, Chordata Motion Inc.) to measure lower limb and trunk kinematics, and

wireless surface EMG (16-channel DTS EMG, Noraxon Inc.) to measure human muscle activations and effort.

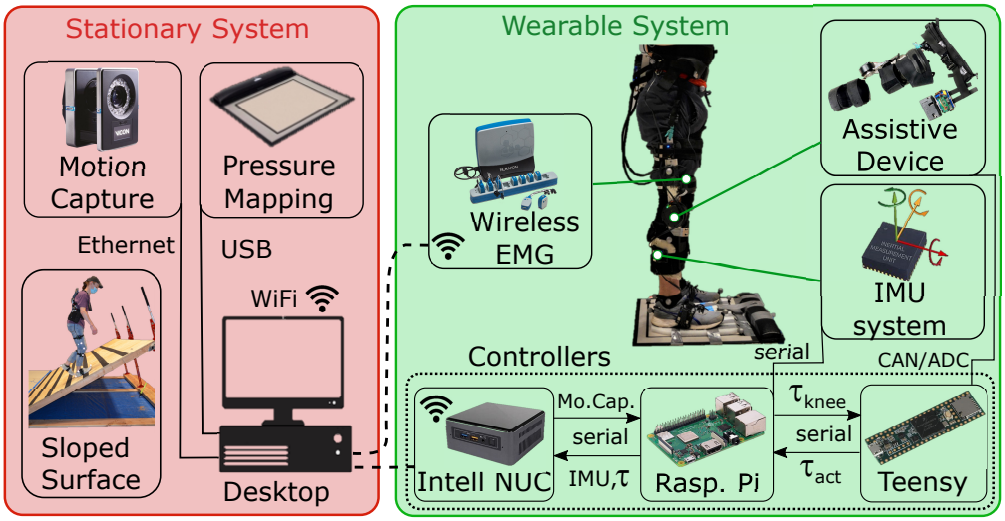

Figure 5.3: Schematics of the experimental system integration. Wearable sensors suits includes: bilateral knee assistive exoskeleton device, lower-body IMU system, and wireless surface EMG to measure thigh, hip and shank muscle activations. Laboratory-based stationary system consists of sloped surface with anti-skid tape, optical motion capture cameras, and portable pressure mat.

In the experiments, we collected data from the Vicon motion capture system at a 100 Hz sampling frequency. Sixteen reflective markers were placed on the lower limbs and trunk, and joint angles were calculated using custom algorithms in Matlab software (MathWorks, Natick, MA). Surface electrodes were placed on knee extensor muscles (Rectus Femoris (RFEM), Vastus Lateralis (VLAT), and Vastus Medialis (VMED)), knee flexor muscles (Biceps Femoris (BFLH) and Semitendinosus (SEMT)), shank extensor muscle (lateral gastrocnemius (LGAS)), and hip extensor (Gluteus Maximus (GMAX)) and hip abductor muscles (Gluteus Mediuss (GMED)). The activations of the selected muscles were measured to evaluate the subjects' exerted effort during kneeling tasks with and without assistive torque. The EMG data were collected at 1500 Hz and the raw data were processed by a series of post-processing steps. Notch filtering (10-500 Hz) was first applied to eliminate noise. The muscle activation signals were normalized with the average value of that specific muscle obtained throughout the entire

trial to eliminate the effect of the applied contact pressure affecting the absolute values of the EMG measurements. The processed data were then rectified and the average of root means square (RMS) was computed and used in the analysis.

5.2.2 Portable Knee Exoskeleton with QDD Actuation

The knee exoskeleton aims to assist during knee extension and distribute musculoskeletal load and stress from the knee joint to the thigh and shank. The portable knee exoskeleton design is compact by using an integrated lightweight actuator with unilateral or bilateral configuration. Fig. 5.4 shows the main components of the exoskeleton for unilateral configuration.

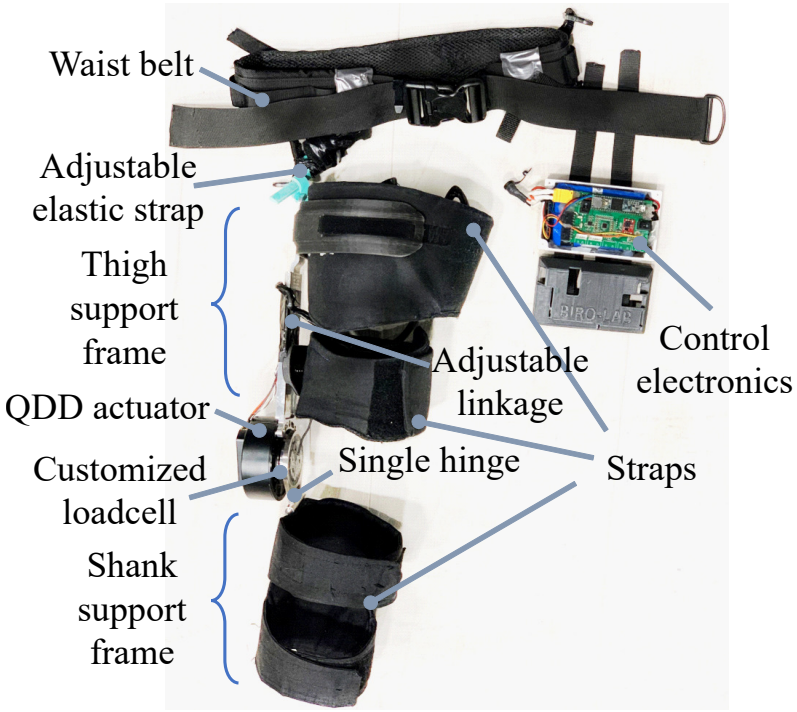

Figure 5.4: The mechanism and components of the knee exoskeleton.

The waist belt supports the weight of the exoskeleton through elastic straps connected to the device's thigh support frame. The belt has an integrated compartment for the micro-controller and battery. The pretension of the elastic straps helps anchor the knee actuator to prevent misalignment. The thigh support frame includes a height-

adjustable aluminum linkage on the lateral side of the leg, a cuff on the posterior upper thigh, and a cuff on the anterior lower thigh. The knee joint actuation system includes a QDD actuator and a customized torque sensor ($\pm$ 40 Nm full scale and $\pm$ 0.1 Nm resolution). The QDD actuator is connected to the thigh support frame, and the load cell is connected to the shank support frame. The shank support frame includes a large anterior shank cuff and a single hinge structure to provide a passive degree of freedom allowing to fit the exoskeleton to subjects of different heights. The knee exoskeleton range of motion is 0-160° (flexion), and the anterior lower thigh and shank contact elements do not interfere during kneeling.

The middle-sized unilateral knee exoskeleton without waist belt and battery weighed only 1.7 kg. The total weight of the bilateral knee exoskeleton (with waist belt and battery) is 4.1 kg, the lightest among reported similar devices. The overall customized QDD actuator is lightweight (710 grams), compact (98 mm (diameter) $\times$ 49 mm (height)), and can generate 35 Nm peak torque. It includes a high torque density BLDC motor, a 6:1 ratio embedded planetary gear, a 16-bits high accuracy magnetic encoder, and an embedded controller. We implemented a low-level control loop for position, velocity, and current feedback. High-level control devices can send a command to read and write the real-time information through the Controller Area Network (CAN) communication protocol. The actuator can reach a nominal speed of 155 rpm (16.23 rad/s). Due to using low gear ratio transmission design, the actuator has low output inertia (52.2 kg cm^2), which is essential for achieving low impedance and therefore minimizes the resistance to natural human movements.

The electrical system of the knee exoskeleton facilitates high-level torque control, motor control, sensor signal conditioning, data communication, and power management. The high-level micro-controller runs on Raspberry Pi and implements torque control based on the proposed torque design described in Section 5.3. A 450 grams 2500 mAh LiPo battery is used to power the knee exoskeleton, which provides over 2 hours life-

cycle of kneeling torque assistance.

5.2.3 Experimental Protocol

Human subject tests were performed to analyze effectiveness of the device during kneeling tasks. Two healthy young male subjects ($n = 2$, age: 34 ± 4 years, mass: 75 ± 2 kg, height: 180 ± 2 cm) were recruited to perform simulated construction tasks. Only male subjects were recruited in this study, considering only 3.5% of women working in the construction and extraction occupations [107]. The testing protocol was approved by the Institutional Review Board (IRB) at Rutgers University.

The main trials of the experiments included single-leg and double-leg kneeling tests. In each trial, subject performed set of kneeling tests wearing the device with three assistive torque modes: non-powered device ("No Torque"), low assistive torque ("Low Torque"), and high assistive torque ("Hi Torque") that was determined as close to maximum torque capabilities of the assistive device. Each set of tests was performed on three slopes (0, 10, and 20 degs). These specific sets of tests were designed to analyze the effect of wearing the device on muscle activation reduction during kneeling tasks. During single-leg kneeling tests, the subjects were instructed to first step on the pressure mat, stand still for 5 secs, then kneel down on one knee in a kneeling position for 5 secs and stand up. Seven repetitions were performed for each test. For the double-leg kneeling experiments, the subject started by standing in front of the pressure mat, then squatted down and knelt into an upright kneeling position on both knees (i.e., Gait A) and held position for 5 secs. The subject leaned forward and then backward into a full deep knee flexion position (i.e., Gait B) and kept still in each position for 5 secs. The subject then stood up simultaneously with both knees and repeated this sequence 5 times for each set of tests. In between each test set, subjects had five-minute pause to fully recover and to eliminate any fatigue effects.

5.3 Bipedal Kneeling Control

5.3.1 Biomechanics Model and Knee Torque Assistance

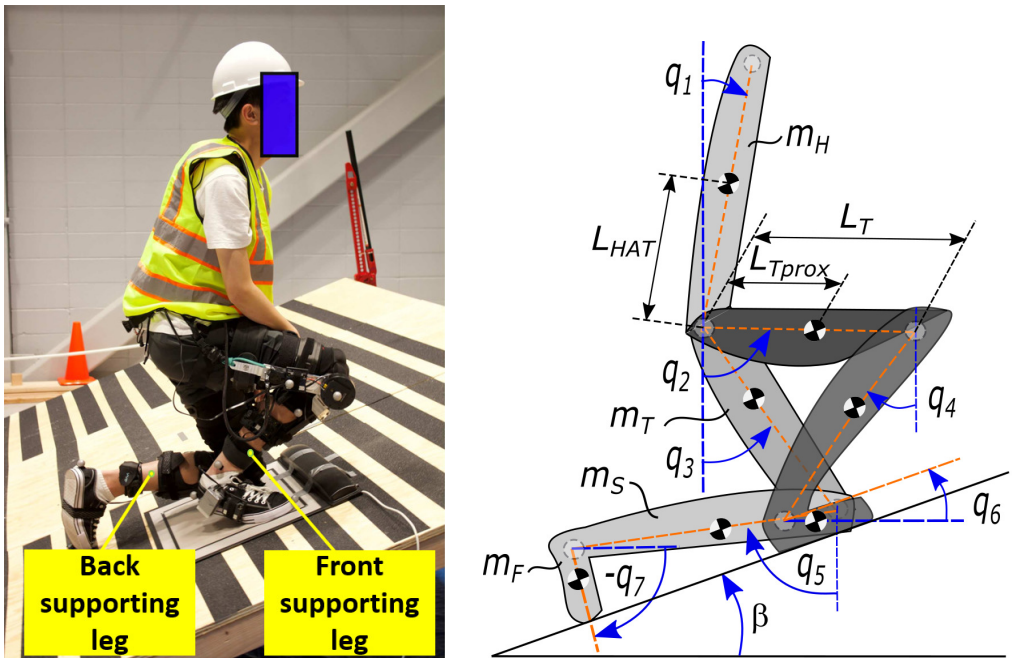

(a) (b)

Figure 5.5: (a) Construction worker during single-leg kneeling on a sloped surface. (b) Schematics of the 7-link human kneeling model. In the single-leg kneeling gaits, the back leg with knee touching the floor was defined as back supporting leg, and the other one was defined as front supporting leg.

Fig. 5.5 illustrates the schematic of the human biomechanics model during kneeling. Kneeling motion is considered in a sagittal plane. The human gait is represented by a 7-link rigid body model; see Fig. 5.5(b). The HAT link represents the head, arms and torso, and is connected to both thighs. A set of relative angles q_i, $i = 1, \ldots, 7$, are introduced to define the coordinates of the individual link with respect to the perpendicular direction to the sloped surface. Defining $\boldsymbol{q} = [q_1 \ \cdots \ q_7]^T$ as the generalized coordinate, similar to [108], the standing-to-kneeling motion dynamics are described as

$$\boldsymbol{D}(\boldsymbol{q})\ddot{\boldsymbol{q}} + \boldsymbol{C}(\boldsymbol{q}, \dot{\boldsymbol{q}})\dot{\boldsymbol{q}} + \boldsymbol{G}(\boldsymbol{q}) = \boldsymbol{\tau}, \tag{5.1}$$

where $\boldsymbol{D}(\boldsymbol{q})$, $\boldsymbol{C}(\boldsymbol{q}, \dot{\boldsymbol{q}})$, and $\boldsymbol{G}(\boldsymbol{q})$ are the inertia, Coriolis, and gravity matrices, respectively, and $\boldsymbol{\tau}$ is the joint torque input vector. To determine the knee assistive torque during single-leg kneeling gait as shown in Fig. 5.5, a quasi-static motion is considered during standing, stationary kneeling, and kneeling transitions. For construction workers, the kneeling down and standing up motions on the sloped and level surfaces are typically relatively slow, thus the assistive knee torque mainly compensates for the weight of subject's body parts along the kinematic chain between the front knee and knee contact point. We ignore the inertia and Coriolis terms in (5.1) and consider only gravitational terms contributions of body parts with the highest mass to obtain the estimated knee assistive torque as

$$\begin{aligned}\tau_R = &- w_R\Big[m_H g\big(L_T \sin(q_2+\beta) - L_H \sin(q_1-\beta)\big) \\ &+ m_T g\big(L_T - L_{Tp}\big)\sin(q_2+\beta) + m_T g\big(L_T \sin(q_2+\beta) \\ &- L_{Tp}\sin(q_3+\beta)\big)\Big], \end{aligned} \tag{5.2}$$

where $0 \leq w_R \leq 1$ is the assistance weight factor, β is the slope angle, m_H and m_T are respectively masses of the HAT and the thigh, L_T is a length of a thigh, and L_H and L_{Tp} are distances from the hip joint to the center of mass of the HAT and thigh segments, respectively. In (5.2), the three terms are the moments exerted on the front supporting leg knee joint, due to the gravity of the HAT, and front and back leg thighs, respectively. Although (5.2) is for the estimated assistance torque for the front supporting leg knee as in Fig. 5.5, it is also used for the back supporting leg knee by swapping q_2 and q_3 due to symmetry.

The assistive torque is computed for each individual subject using their anthropometric parameters that are estimated using methods in [109]. The knee assistive torque in (5.2) is designed for single-leg kneeling gait. For double leg kneeling, the last term in equation (5.2) was excluded and the torque is valid for both legs considering the re-

spective thigh angles. This is due to the symmetric configuration of double leg kneeling gaits and both legs equally contributing to support the weight of the subject, including HAT and thigh segments.

The amount of assistance by the exoskeleton is tuned by changing w_R in (5.2). The gains of torque assistance during single-leg kneeling were set as $w_R = 0.55$ and 1.00, and $w_R = 0.4$ and 0.8 during double-leg kneeling experiments for low- and high-torque assistance, respectively. These values are chosen to prevent the torque saturation or exceeding the maximum torque capabilities of the device.

5.3.2 Exoskeleton Controller

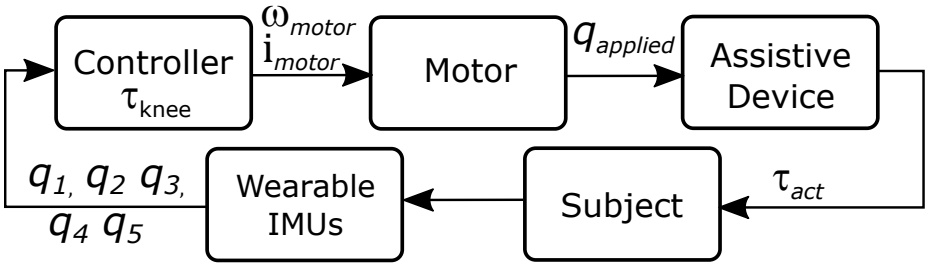

Figure 5.6: Schematics of a high-level structure of controller design to provide knee assistive torques to construction workers during kneeling tasks. Thigh angles (q_2, q_3), shank angles (q_4, q_5) and low-back angle (q_1) were obtained from the IMU measurements.

The exoskeleton control in the previous section is primarily based on the trunk and thighs gravity compensation during kneeling gait considering upright posture as a neutral pose. Fig. 5.6 shows the schematics of the high-level controller design. The exoskeleton provides assistive torque to the knee joints based on the detected gait intention. The gait detection is built on the direct measurements from the wearable IMUs on thighs (q_2, q_3), shanks (q_4, q_5), and lower back (q_1). The low-level controller includes velocity feedback as an outer loop and current feedback as an inner loop to guarantee the desired torque performance and proper motion tracking of the device.

The start and end of the kneeling gait are detected based on the moving average of the

last five frames (0.1 sec) of the shank angle (q_4, q_5) obtained from IMU measurements. Compared to the standing pose, if the average value of shank angle exceeds a fixed threshold (i.e., 5 degs), the kneeling motion is detected. Similarly, if the averaged shank angle reaches again the threshold, the end of standing-up motion is detected; see Fig. 5.7.

5.4 Experimental Results and Discussions

5.4.1 Experimental Results

Fig. 5.7 shows the ground reaction force profiles and kinematics of a representative subject during single-leg kneeling experiment on a level (0 deg) surface. Force profiles are normalized with respect to subjects' body weight. The kneeling gait is defined from the beginning of the kneeling down event to the end of standing up event; see snapshots at the top of the figure. Fig. 5.7(a) shows the force profiles and kinematics without any applied assistance torque and Fig. 5.7(b) shows the exerted high knee assistance torques and force profiles on both legs. The applied maximum mean torque (averaged over 7 repetitions) is around 22 Nm on the knee of the front leg and close to zero torque for the knee of the other leg. Measured kinematics using the IMUs of the absolute thigh, low back, and relative knee angles show consistent trends for no, low and high knee assistance torques. The measured contact forces under the front foot and the knee during the 50-60% of the kneeling gait show knee load reduction (Fig. 5.7(b)) when an assistive torque is applied to the front (right) supportive knee. The total force profiles exerted by both the front leg and knee show similar values for tests with and without torque assistance. These results confirm a weight shift from the knee on to the supporting leg under provided assistive torques.

To investigate the effect of assistance torque across various slopes, we computed and compared the average of pressure profiles during stationary kneeling period (50-60% of the kneeling gait). Fig. 5.9 shows comprehensive kinetic results from tests across all subjects on three slopes (i.e., 0, 10, and 20 degs) with three torque profiles (i.e., No,

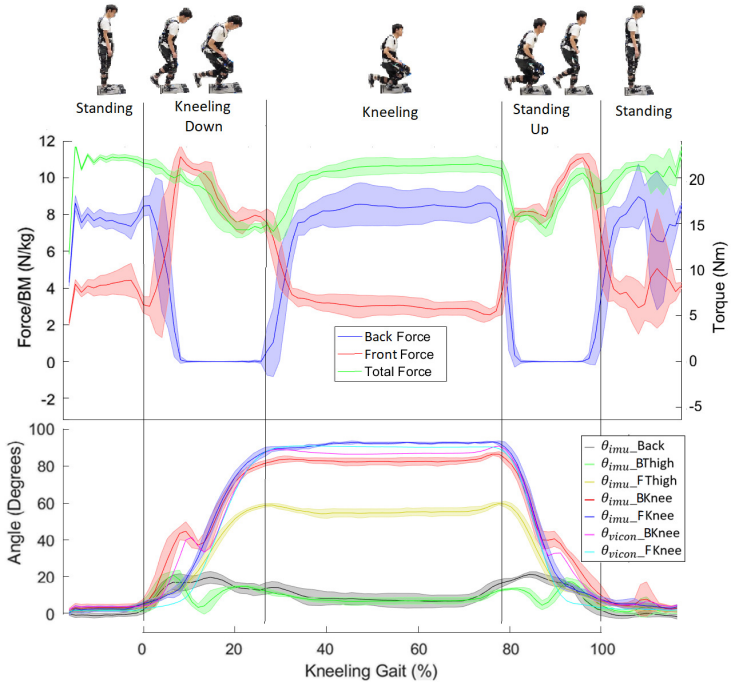

(a)

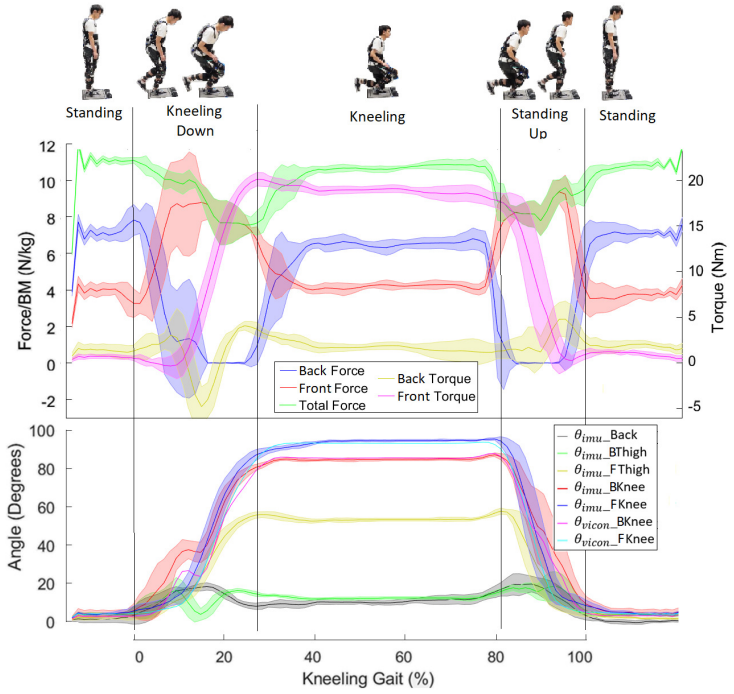

(b)

Figure 5.7: Kinematics and kinetics during single-leg kneeling gait on level (0 deg) surface (a) without and (b) with provided "High" assistance knee torque (around 22 Nm) during one kneeling gait. Forces were normalized with respect to the measured total force during the initial standing portion of each test set.

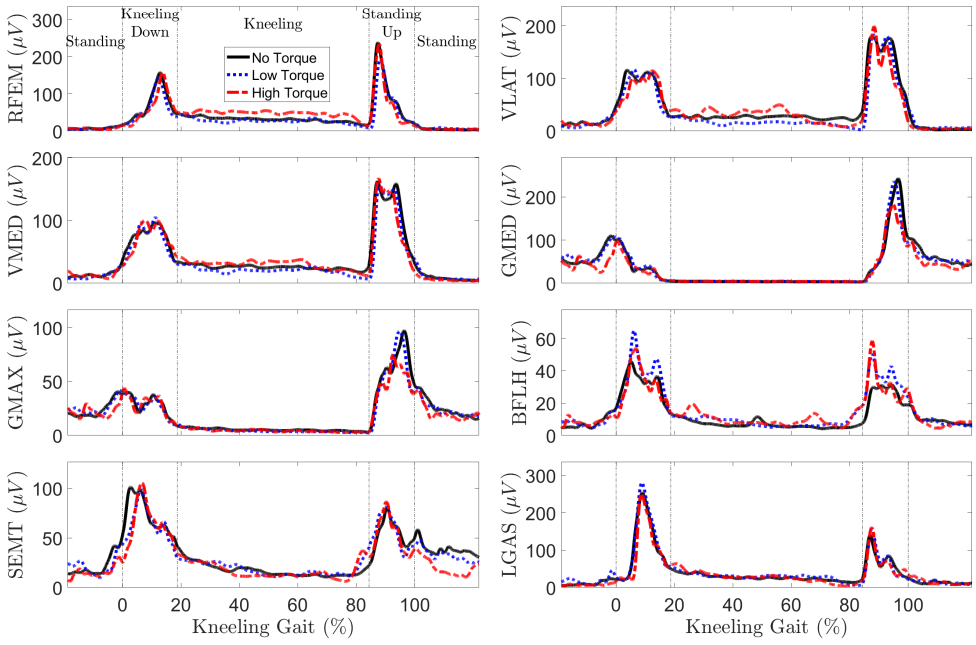

(a)

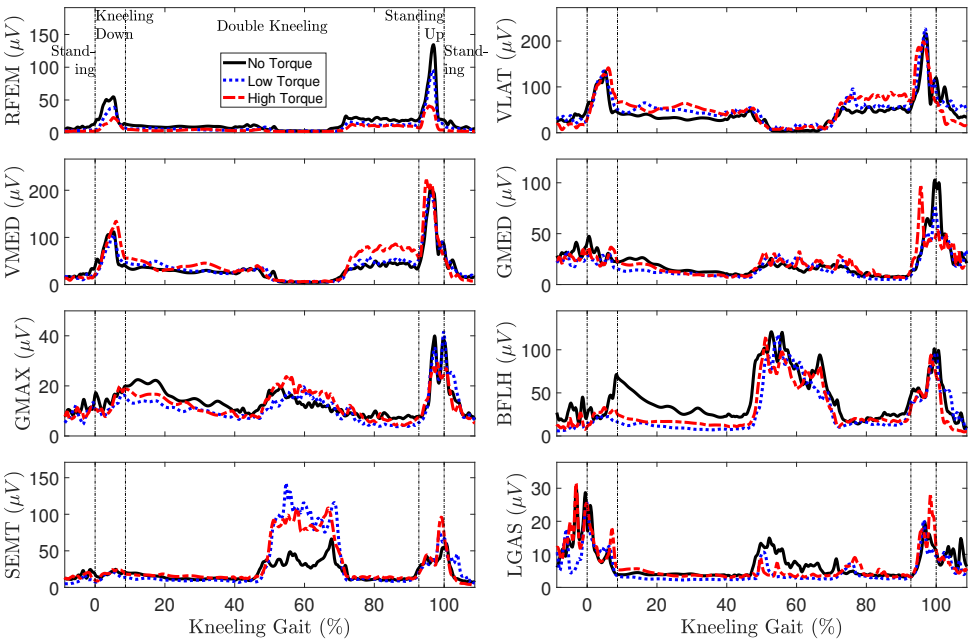

(b)

Figure 5.8: Muscle activation profiles of a representative subject during (a) single-leg and (b) double-leg kneeling on a 20 deg sloped surface. The EMG plots include three different assistive torque profiles: “No torque” (power off), “Low torque”, and “High torque”. The plots are for the subject’s dominant leg, that is, front supporting leg in single-leg kneeling test. The kneeling gait is defined between the beginning of kneeling down and the ending of standing up gaits.

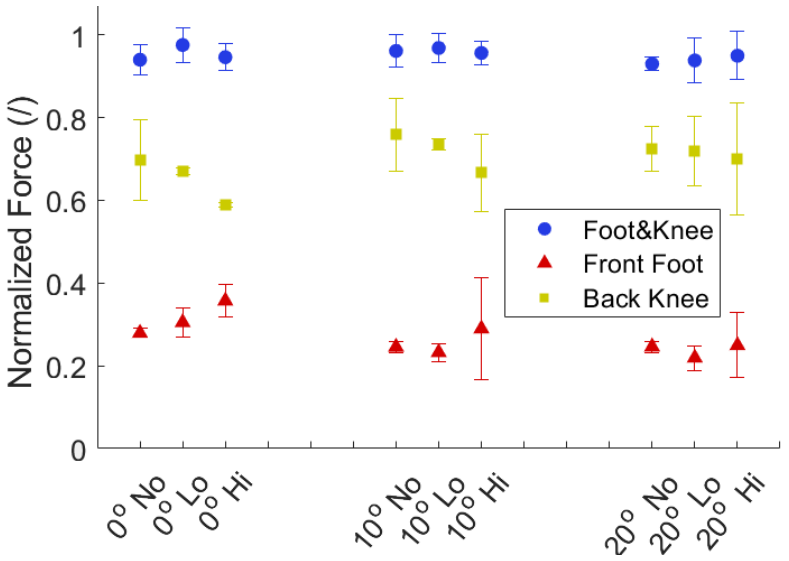

(a)

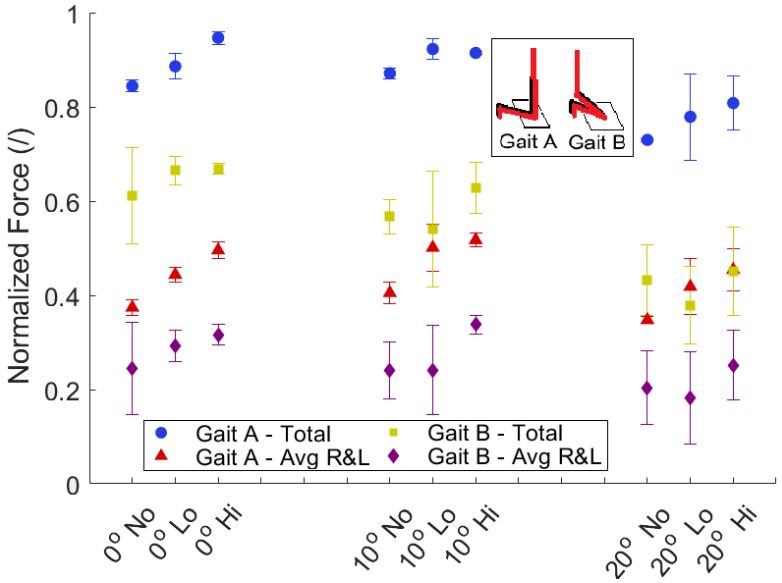

(b)

Figure 5.9: Normalized knee contact forces during (a) single- and (b) double-leg kneeling gaits on 0, 10 and 20 deg sloped surfaces and various assistive torques.

Low and High Torques) for both the single- and double-leg kneeling gaits. The measured forces were normalized with respect to the total force during the initial standing portion of the individual test. The single-leg kneeling results in Fig. 5.9(a) show a load reduction on the knee and a load increase on the front supporting leg with the assistance torques across all surface slopes. The largest reduction (15.4%) was observed for tests on level surface with the high assistive torque. The normalized total exerted force re-

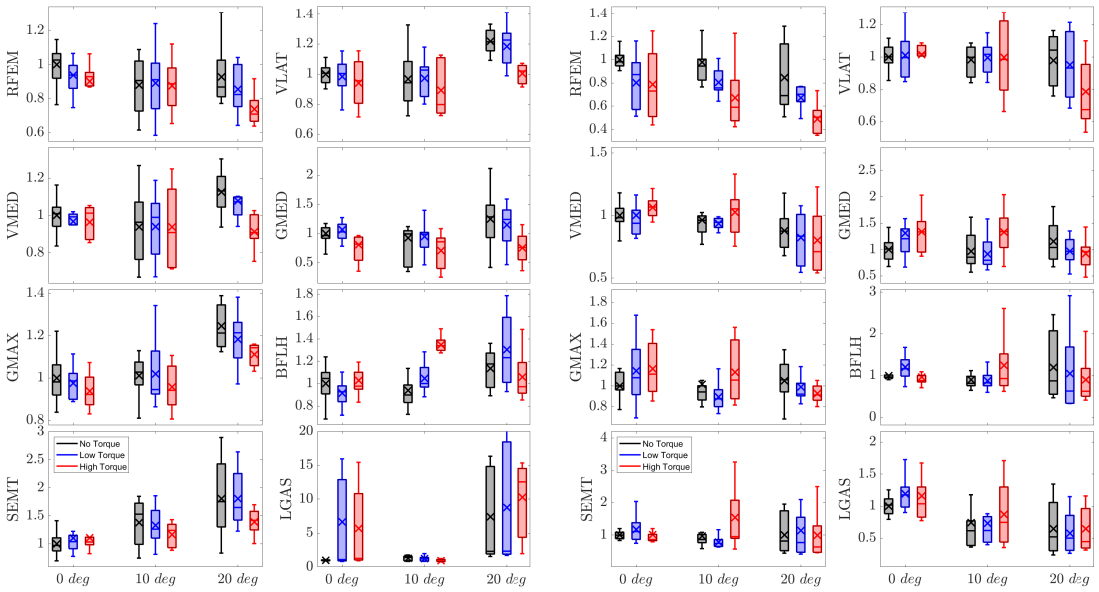

(a) (b)

Figure 5.10: Normalized EMG measurements during standing up from (a) single-leg kneeling pose and (b) double-leg deep flexion kneeling pose on three different slopes (0, 10, and 20 degs). Compared are baseline test ("No Torque", black box plots) and tests when subjects wore the device while provided two levels of assistive torque profiles ("Low Torque" and "High Torque", blue and red box plots, respectively). EMG profiles were normalized for individual subject to the values obtained from the baseline test ("No Torque"). For each box plot, cross mark represents mean value, horizontal bar represents median value, and whiskers represents data distribution of the same muscle across all the test trials for all subjects.

mains constant across all tests, which implies a purely internal force redistribution due to provided assistive torque. These results suggest that the use of exoskeleton benefit in reducing knee loads applied during single-leg kneeling as potential intervention to prevent WMSD.

Fig. 5.9(b) shows double-leg kneeling kinetic results. An increase in the surface slope shows an overall decrease in knee contact pressure. This effect is pronounced for deep flexion kneeling (i.e., Gait B) because a significant portion of the subjects' weight is supported by sitting back on their feet. This does not hold true for the upright double kneeling (i.e., Gait A) on the 10 deg sloped surface, likely because the weight of the subject's vertical trunk is still mostly supported by the knees. The 20 deg slope

results show a significant decrease because a much larger portion of that weight can be supported by the feet without the risk of falling forwards.

Fig. 5.8(a) shows the EMG profiles of a representative subject's dominant leg during single-leg kneeling gait cycle on a 20 deg sloped surface. Each curve represents the average value of 5 repetitions of the same test condition. During standing up from kneeling, the activations of knee extensor muscles (RFEM, VMED and VLAT) of the front supporting leg were reduced under the assistive torque, compared to no torque condition. Results from both the low- and high-torque conditions show reduced muscle activations during the standing up motion. The muscle activations of hip extensor/abductor muscles (GMAX and GMED) were also reduced during the standing up stage. The peak activation of GMAX was reduced by 22.8% and the peak of GMED is reduced by 25.2% under high assistive torque. During the kneeling-down stage, the activations of knee extensor muscles remain almost the same as assistive torques increase. Fig. 5.8(b) shows the average muscle activations during double-leg kneeling test. Activations of knee extensors (RFEM) during kneeling down and standing up were significantly reduced with increased knee assistive torques. Compared to no torque condition, the low- and high-torque conditions reduce the EMG peaks of the RFEM by 34.8% and 53.3% during the kneeling down motion and 39.5% and 55.1% for the standing up motion, respectively.

Fig. 5.10 shows the normalized EMG measurements during standing up portion of the single-leg (Fig. 5.10(a)) and double-leg (Fig. 5.10(b)) kneeling trials on three sloped surfaces. Presented box plot results show the mean, median, first and third quartile, minimum and maximum values across all subjects. Table 5.1 summarizes the muscle activation reductions. The muscle activities of knee extensors (RFEM, VMED and VLAT) were reduced under low and high assistance torques. Compared to no assistance condition, the average muscle activities of VLAT were reduced by $6.4\%, 7.1\%$ and 18.7% on the 0, 10 and 20 degs slopes, respectively; for muscle RFEM, the reductions are 10.0% and 20.5% and for VMED the reductions were 3.7% and 18.4% on the 0 and

20 degs slope respectively. On the 20 deg slope, the hip muscles GMED and GMAX were reduced by 39.5% and 10.9%, respectively, under high assistive torque when compared with no-torque condition. In the single-leg kneeling tests, the muscle activations of BFLH and SEMT during standing up gait phase showed an increase with the increase in surface slope. This might be due to subjects utilizing the back thigh muscles to stabilize and balance themselves on sloped surfaces. In addition, providing a high torque assistance during standing up on 0-deg slope showed no or minimal increase, while on 20-deg sloped surface showed a decrease of BFLH and SEMT muscle activations compared to no torque assistance. The reason is that provided high assistive torque from a wearable device requires subjects to use less effort to stand up on sloped surface, resulting in reduced muscle co-contractions and lower muscle activations. For LGAS muscle, the trend in muscle activation is less clear as the slope and assistive torque increase and additional investigation is required for more detailed analysis.

Table 5.1: Muscle activation changes with exoskeleton for all subjects during single-leg kneeling gait experiments.

Assistance	Slope	Muscles				
		RFEM	VLAT	VMED	GMED	GMAX
Low assist.	$0°$	-6.2%	-1.7%	-3.2%	6.4%	-2.5%
	$10°$	0.1%	0.5%	0.2%	2.2%	0.8%
	$20°$	-7.8%	-2.9%	-4.4%	-8.0%	-5.1%
High assit.	$0°$	$\mathbf{-10.0\%}$	$\mathbf{-6.4\%}$	-3.7%	$\mathbf{-19.1\%}$	-6.2%
	$10°$	-0.3%	$\mathbf{-7.1\%}$	0%	$\mathbf{-23.8\%}$	-5.3%
	$20°$	$\mathbf{-20.5\%}$	$\mathbf{-18.7\%}$	$\mathbf{-18.4\%}$	$\mathbf{-39.5\%}$	$\mathbf{-10.9\%}$

Fig. 5.10(b) shows a similar analysis for double-leg kneeling test. Under low- and high-torque assistance, the average muscle activities of knee extensor (RFEM) were reduced by 19.8%, 17.9%, 20.4% and 21.3%, 31.5%, 42.4% on the 0, 10 and 20 degs sloped surfaces, respectively. As shown in Fig. 5.8(b), for double-leg kneeling gaits, the muscle activations of VLAT, VMED, GMED and GMAX remained almost the

same when assistive torque was applied during both kneeling down and standing up. Compared with no torque trial, the muscle activation of SEMT increased as the subject switched from upright kneeling position (Gait A) to leaning forward and backward (Gait B), while the muscle activation of BFLH decreased from kneeling down to Gait A. The muscle activation of VLAT and VMED slightly increased when the subjects kept the kneeling pose (during Gaits A and B) and this might be due to the adaptation to the exoskeleton. A further study is required to investigate how adaptation affects the muscle activation results.

5.4.2 Discussions

Knee angle profiles obtained from IMU measurements were compared to the ground truth results from the optical motion capture system; see Fig. 5.7. They are in a good agreement, which validates the measurements from the wearable IMU system. The results in Fig. 5.9(a) clearly demonstrate the reduction of the exerted contact pressure on the knee when assistive knee torque is provided and this observation suggest that wearable exoskeleton can potentially reduce musculoskeletal injury risk and prevent KOA during single-leg kneeling tasks. The results of the double-leg kneeling tests in Fig. 5.9(b) show increased knee pressure with an increase of assistive torque across all slopes for Gait A kneeling. Results of Gait B deep flexion kneeling on 10 and 20 deg slopes show knee contact pressure decrease during low torque and increase during high torque assistance, respectively. The knee contact pressure under no assistive torque across all slopes does not show a clear correlation. Further investigation is required to investigate the above mentioned observations.

As shown in Table 5.1, activation levels of some muscles during the single-leg kneeling on the 10 deg sloped surface do not perfectly follow the expected trend with increased torque assistance as observed on the 0 and 20 deg sloped surfaces. The back thigh muscle (BFLH) shows an increased muscle activation, while all three knee exten-

sor muscles (RFEM, VLAT, and VMED) show minimal changes. Further experiments are required to fully explain these results. During single-leg kneeling on 20 deg sloped surface, large reductions of GMED and GMAX muscles were observed during high torque assistance compared to no torque conditions. This might be due to subjects using muscles around hips to keep postural balance on the surfaces with larger slope. The muscle activities of the back thigh and back shank muscles remained the same or slightly increased, which might be due to the imperfect fit of the device and potential misalignment between the device and the human subject. In Fig. 5.8(b), during the 50%-70% of the kneeling gait, the subjects were leaning forward during double leg kneeling on 20 deg sloped surface. In this pose, the current configuration of the exoskeleton does not provide much assistance to the subjects. Moreover, in the forward leaning pose, the subjects utilized their back thigh muscles (i.e., SEMT) and co-activated flexor-extensor muscles to stabilize the trunk to keep their balance, thus the muscle activation increases during this process. The level of muscle activation during static leaning forward pose in the double leg kneeling pose needs further investigation and is part our future work. Standing up from both single- and double-leg kneeling gaits shares similarities with squatting motion and we observed similar muscle activation increase of the knee flexors muscles (SEMT and BFLH) as previously reported during squatting task [39]. A comprehensive analysis of metabolic cost could provide additional information about the total work performed by muscles and would help evaluate benefits of using the device. Overall, using the current controller and exoskeleton design, the muscle activations during the kneeling gaits on 20 deg sloped surface were reduced on average by 21.6% with active control on, which indicates benefits of the exoskeleton assistance. Improved design of exoskeleton actuator and increased comfort level when wearing the exoskeleton, the assistive torque can be increased for kneeling gaits, which may result in further reduction of the muscle activations.

In our current implementation, a simplified threshold-based kneeling gait detection

algorithm was used. The algorithm was sufficient for the purpose of detecting the start and end of the kneeling gait. However, the algorithm should be improved for accurate, real-time detection of complex kneeling gait events during construction tasks, which is out of the scope of this dissertation. During kneeling tests with wearing the device, the knee and device sometimes touched the pressure mat that resulted in decrease in peak pressures. Design improvement of the device would help avoid these disturbances.

There are several limitations in this study. One is the limited number of human subjects and we need to conduct experiments on large amount of human subjects, particularly including subjects of various body sizes and ages. A specific effort will have to be made to adjust device to each individual subject to guarantee a proper fit and comfort while wearing the device. Although the results in this chapter demonstrate the feasibility and promising potential of the knee pressure and muscle activation reduction by supplied assistive torques, all experiments were conducted by healthy subjects and no construction workers were recruited. It would be valuable to test the wearable assistive devices with professional construction workers at industrial sites.

5.5 Summary

This chapter presented a mechatronic assistive system design in kneeling assistance for construction workers. We developed a novel controller design to assist construction workers using an improved design of a bilateral knee exoskeleton with enhanced torque capabilities (up to 35 Nm) and wearable, non-tethered configuration. Several wearable and stationary sensor suites were used to measure subjects' kinetics, kinematics, and physiological parameters during kneeling tasks. The results showed reductions in muscle activation of knee and hip extensor muscles during standing from kneeling with the highest reduction under high-torque assistance on highly slopped surfaces. Measurements of ground reaction forces showed reductions in knee pressure with increased torque assistance. The human subject testing results validated the effectiveness of the

device with the goal to reduce and alleviate WMSD risk for construction workers when performing kneeling tasks on level and sloped surfaces.

Chapter 6

Real-Time Walking Gait Estimation for Construction Workers

6.1 Introduction

Construction workers often suffer intense physical effort, and are exposed to serious safety and health risks in hazardous, dynamic working environments. One of the most common locomotions in construction trades is walking gait on flat and sloped surfaces (e.g., scaffold workers and roofers). It is critical to monitor workers' gaits and body poses in real-time for safety and health conditions [110]. Wearable IMUs are particularly attractive for gait detection and posture estimation in construction because they are small-size, low-cost and non-intrusive [42].

Wearable inertial sensors were widely used for human kinematics. In [47], two IMUs were attached to the back of the helmet and the worker's back for head, neck and trunk inclination estimation. The wearable sensors in [111] included eight IMUs on the trunk and limbs to detect gaits and motion of construction workers. In [112], 17 IMUs were used to identify poses of masonry workers using support vector machines. Comparison results of various IMU locations on the human body were reported in [113]. However, the pose estimation accuracy of the IMU measurements in these studies has not been systematically and extensively validated. Moreover, wearable IMUs were not studied for real-time applications in the above-mentioned work and accurate limb poses were not among the focus. In [49], a real-time gait event detection was presented to

capture walking gait events over level and inclined surfaces and staircases using one single IMU. Similar types of real-time walking gaits detection were also reported in [50, 51, 52] for periodic movement using machine learning methods. For gait detection of non-periodic human movements, [111] used a set of wearable IMUs on human limbs and trunk to monitor construction workers' gait activities. Wearable IMU-based human gait detection was also presented in [114] for real-time applications.

As mentioned above, increasing use of machine learning techniques was reported in the past few years for human activity or gait classifications, and readers can refer to two recent reviews [115, 116]. In [53], recurrent neural network (RNN) with long short-term memory (LSTM) cells were used to reconstruct human poses during various motions in real-time. A hierarchical multivariable hidden Markov model was employed in [54] for full-body locomotion reconstruction of human walking, running, jumping, and hopping motion on a flat floor using one IMU attached to the subject's shank. Considering the periodic walking gait, a phase-functioned neural network model was presented in [55] to generate the human walking character in animation with fast computational capability.

Inspired by these work and motivated by construction applications, we present a real-time gait detection and pose estimation scheme for walking on flat and sloped surfaces using one single IMU. An LSTM approach is first used to detect the human walker gaits and the slope angle. A learned motion manifold is then constructed using the gait activity information. The pose estimation is built on the learned motion manifold and the IMU measurements. We use the Gaussian process dynamic model (GPDM) to construct the human motion manifold [117, 7]. Due to periodic feature in biped walking, the learned GPDM is a closed manifold in latent space and similar to [55], a phase variable is used to parameterize the GPDM model to predict the joint angles in real-time. Extensive human experiments are conducted on flat and sloped surfaces that represent roof workers in construction. The experimental results demonstrate the efficacy and effectiveness of the design. The main contribution of the work lies in the

novel integrated LSTM and GPDM gait detection and pose estimation for real-time applications using one single IMU. The design provides a potential enabling tool for integrated wearable robotic systems to reduce the risk of work-related musculoskeletal disorders in construction.

The remainder of the chapter is organized as follows. Section 6.2 introduces the experiment configuration and data collection. In Section 6.3, we present the machine learning-based real-time gait detection and pose estimation algorithms. Experimental results are discussed in Section 6.4 before we summarize the concluding remarks in Section 6.6.

6.2 Experiments and Data Collection

6.2.1 Experimental Setup

We created a laboratory environment that mimicked construction workers on the level and sloped surfaces. A wooden slope structure with glued anti-skid tapes was designed as a roof structure and the roof slope can be adjusted to reach any angle up to 40 degs. Fig. 6.1 shows the overview of the data collection systems used in the experiments.

To measure the human kinematics and motion, an IMU sensor (from WitMotion Inc.) was attached to the right shank of the subject; see Fig. 6.1(a). The raw IMU data consists of 12 measurements (3-joint angles, 3-gyroscope, 3-linear acceleration, and 3-magnetometer). The IMU sensor was carefully placed on the same location of the shank segment with same orientation before each trial. A motion capture system (8 Vantage cameras, Vicon Motion Systems Ltd.) with sampling frequency of 100 Hz was used to collect marker position for reference motion. 39 markers were placed on subjects' lower and upper limbs, trunk and head to represent full-body motion. Joint angles were calculated using custom algorithms in MATLAB software (Version R2020a, The MathWorks Inc.) using the marker positions. The IMU measurements were sampled at 100 Hz, and the data were wirelessly transmitted to the portable embedded computer (Intel

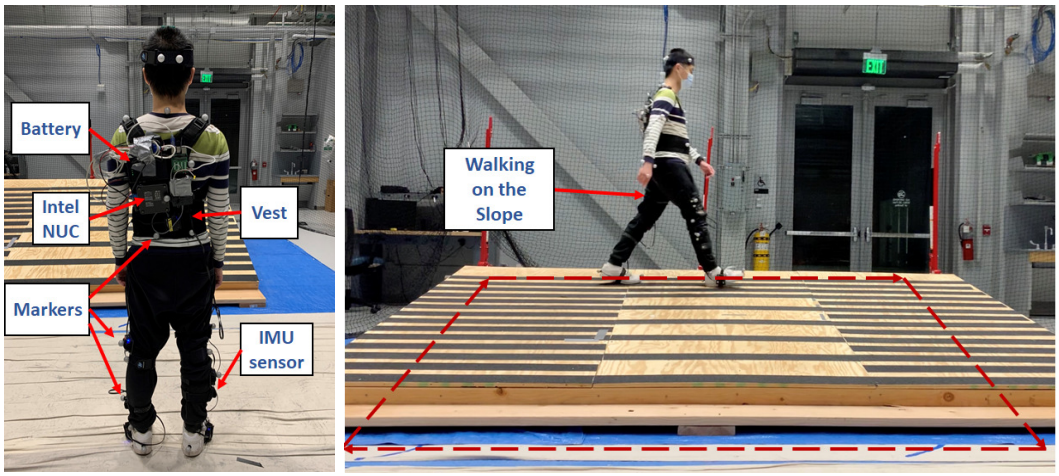

(a) (b)

Figure 6.1: Laboratory experimental setup mimicking roof workers in construction. (a) Wearable IMU and embedded systems. (b) Walking setup on variable slopped wooden structure.

NUC7i7DNK, Intel Corp.) which was worn by the subject (Fig. 6.1(a)). In the training phase, all the data were connected and synchronized through a desktop computer and portable high-performance embedded computer. In the testing phase, data collection, real-time gait detection, and pose estimation algorithm were implemented on a desktop computer (Dell XPS-8953, Dell Inc). The desktop computer is equipped with Intel i7-8700 CPU, Nvidia 1030 GPU, and 16 GB RAM.

6.2.2 Experimental Protocol

Five healthy subjects ($n = 5$, age: 30 ± 3 years, weight: 73.3 ± 6.5 kg, height: 172.0 ± 6.7 cm) were recruited for experiments, and they are capable of walking on flat and sloped surfaces. Four types of walking patterns were defined in experiments: walking on the level ground, walking up on the slope, walking transverse the slope and walking down the slope; see Fig. 6.1(b). The subjects were instructed to use their normal gaits and self-selected speeds to walk on the level and the sloped surfaces. An informed consent form was signed by all the subjects, and the Institutional Review Board (IRB) at Rutgers University approved the testing protocols.

The subject started walking on the level ground surface and then followed the sequence of up the slope, transverse the slope and down the slope in the clockwise direction and finally returned to the starting location. The subjects repeated the sequence in the first four minutes for the training data collection phase, and then in the last minute they only walked transverse the slope from one side to the other side to collect the data in the symmetric direction. Three slope angles were selected in the training experiment: 5, 10, and 15 degs. For real-time pose estimation tests, IMU sensor data was streamed live to a local computer and treated as inputs of the trained model.

6.2.3 Data Preprocess

The IMU and motion capture data were preprocessed by customized scripts. The walking activities were labeled based on the four different patterns. In each activity, only the complete strides were used for data analysis. The stride information was extracted from motion data, and stride length and walking speeds were calculated. The beginning and ending of each stride was defined by using the location of heel markers. The current and next right foot heel strikes were set as $s = 0\%$ and 100% of the gait phase, respectively, where s is the gait phase variable. To enlarge the training data set, multiple strides of the same activity were concatenated. To derive the latent space variables, averaged strides parameters from all the subjects were calculated. The strides from the same activity were resampled to be in the same frame length.

The corresponding IMU data were also concatenated for the same activities. IMU data were reshaped for the training purpose and 60 consecutive frames were combined as one frame data. The IMU sequence data was normalized with the mean and standard derivation of the data set, which was then used as inputs of the model. In the testing phase, 59 past frames with one current frame data were combined to form the input of the pose estimation model. The same mean and standard deviation were used to standardize and normalize the real-time IMU data, that is, the IMU sequence was subtracted by

mean and divided by standard derivation of the training data.

The pretrained learning models and neural network parameters were stored in the local computer. The real-time IMU sequence data were streamed into the learned model, and the subject's motion activities and pose was estimated. In a real-time application, we detected foot strike by inspecting the sudden drop of the gait phase variable and the variation of the linear acceleration data. When walk cycle ended and foot strike was detected, the gait phase variable s was reset to the beginning of the stride (i.e., $s = 0$).

6.3 Learning-based Gait Detection and Pose Estimation

6.3.1 Overview

Fig. 6.2 illustrates the overview of the human walk gait and pose estimation scheme. The approach contains three tasks: walking activity detection, gait phase detection and full-body pose estimations. An LSTM-based classification and regression model is used to identify the walking activities (e.g., flat or sloped surfaces), and the estimated slope angle (denoted as θ) is also obtained. The gait propagation and phase variable $s \in [0, 1]$ are estimated using a second LSTM-based RNN. Finally, a full-body human pose estimation scheme is obtained using the GPDM model. In the following, we describe each of these modules in details.

6.3.2 RNN-based Activity Detection and Gait Phase Estimation

The three layers of Fig. 6.3 shows the schematic of the LSTM-based walking activity detection, slope angle estimation and gait phase estimation. The LSTM is a recurrent neural network architecture to learn sequential information using memory cells that stores and outputs information to capture the temporal relationships. As shown in the left bottom of Fig. 6.3, the information update is through various gates and the relationships among the input gate, forget gate and output gates [48]. For the training purpose, the raw IMU data are collected and labeled for four walking patterns on level surface, up the

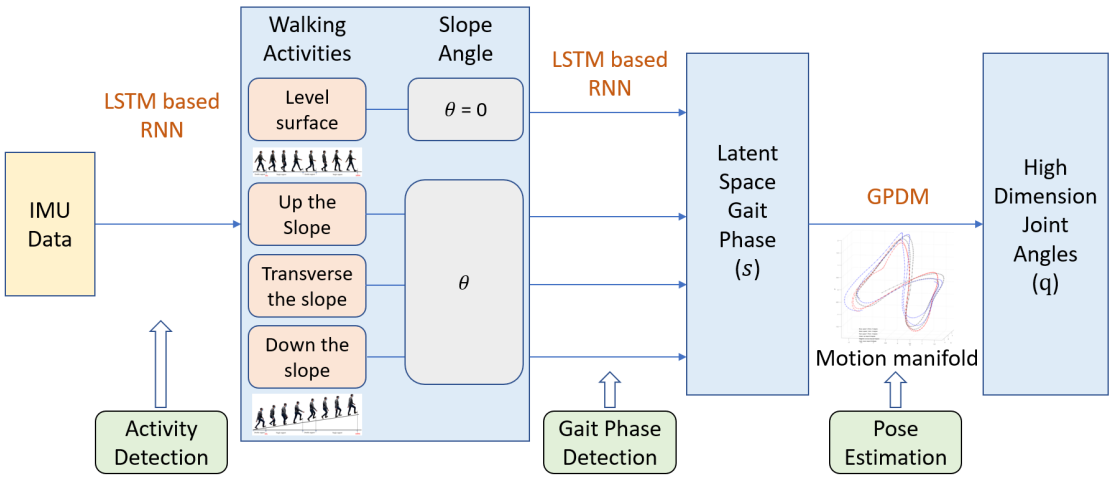

Figure 6.2: Human pose estimation scheme in three stages (Activity detection, gait propagation detection and pose estimation).

slope, transverse the slope, and down the slope with different slope angles (i.e., $\theta = 0$, 5, 10, and 15 degs). The IMU data were scaled and reshaped to three-dimensional input (i.e., samples, timesteps, features) for the LSTM models.

For the activity classification model, the single LSTM hidden layer has 50 neurons and the output of the LSTM layer is passed through a `Dropout` (0.2) layer to randomly drop 20% units from the network to prevent overfitting of the model. The outputs from the dropout layer are passed through a fully connected layer with 50 neurons with `ReLU`. Finally, the fully connected hidden layer is connected to the `Softmax` activation function, which converts the class scores to probabilities such that the activity with the highest probability can be recognized. The slope detection model consists of a two-stacked LSTM-based networks. The first LSTM hidden layer has 64 neurons followed by a `Dropout` (0.2) layer and the second LSTM and dropout layers are used to generate the output. For the classification and model, the categorical cross-entropy and mean squared error are used as loss functions. Adam optimizer is used for both the activity classification and slope angle estimation models. The model loss and accuracy curves are assessed to determine the model fit. The gait phase variable s represents the current percentage of the stride, and is assumed to be increasing within one stride. The

gait phase estimation model contains a two-stacked LSTM-based networks with one `Dropout` (0.2) layer between them, while both LSTM hidden layer has 32 neurons. Adam optimizer is used for gait phase estimation models and mean squared error is used as loss functions.

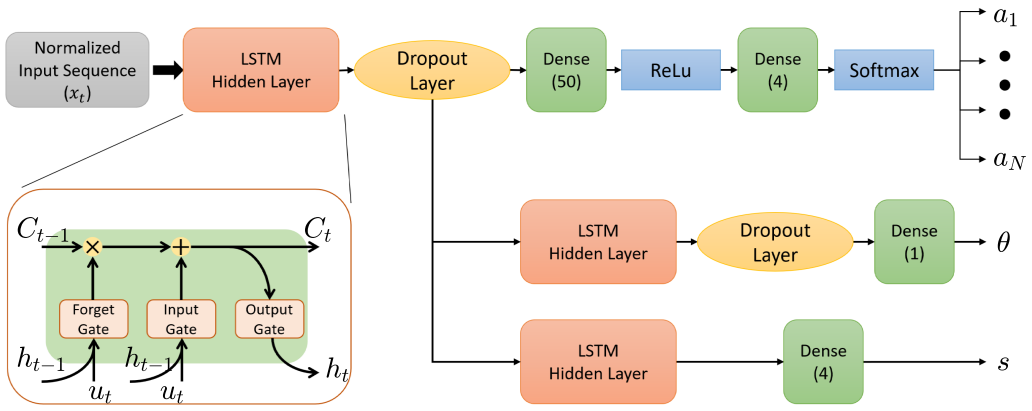

Figure 6.3: Schematic of the LSTM-based gait activity and phase variable estimation scheme.

6.3.3 GPDM Model and Full-Body Pose Estimation

A periodic walking gaits in the high-dimensional joint angle space are represented in low-dimensional latent space through various manifold learning techniques such as GPDM. Let us denote the full-body joint angle as $\boldsymbol{y} \in \mathbb{R}^D$ and the latent state variable as $\boldsymbol{x} \in \mathbb{R}^d$, where d and D ($d \ll D$) are the dimensions of the latent space and the joint angle space, respectively. For each type of the walking activity a_i, $i = 1, \ldots, N$, and slope angle θ, the latent dynamics for human motion are formulated as

$$\mathcal{M}_i(\theta): \begin{cases} \frac{d\boldsymbol{x}_i}{ds} = \boldsymbol{f}_i(\boldsymbol{x}_i, \boldsymbol{\alpha}_i, \boldsymbol{u}_i) + \boldsymbol{w}_{pi}, \\ \boldsymbol{y}_i = \boldsymbol{g}_i(\boldsymbol{x}_i, \boldsymbol{\beta}_i, \boldsymbol{u}_i) + \boldsymbol{w}_{oi} \end{cases} \tag{6.1}$$

where $\boldsymbol{x}_i = \boldsymbol{x}_i(s)$, $\boldsymbol{y} = \boldsymbol{y}_i(s)$, and $\boldsymbol{u}_i = \boldsymbol{u}_i(s)$ are latent state, joint angles and IMU measurements at gait phase variable s, respectively. $\boldsymbol{\alpha}_i$ and $\boldsymbol{\beta}_i$ are GP parameters and

obtained from learning process, $\boldsymbol{w}_{pi}$ and $\boldsymbol{w}_{oi}$ are zero mean model noises for the state dynamics and output models, respectively. In the training phase, the IMU data set $\boldsymbol{U}_i = \{\boldsymbol{u}_i\}_\theta^M$ and joint angle set $\boldsymbol{Y}_i = \{\boldsymbol{y}_i\}_\theta^M$ have number of M training data points that are obtained for walking on surface with slope angle θ. We then estimate the mappings $\boldsymbol{f}_i(\cdot)$ and $\boldsymbol{g}_i(\cdot)$ in (6.1) by identifying parameters $\boldsymbol{\alpha}_i$ and $\boldsymbol{\beta}_i$ through minimizing the posterior probability

$$\mathcal{L}_i = -\ln p(\boldsymbol{X}_i, \boldsymbol{\alpha}_i, \boldsymbol{\beta}_i | \boldsymbol{Y}_i, \boldsymbol{U}_i, \hat{\boldsymbol{X}}_i), \tag{6.2}$$

where $\hat{\boldsymbol{X}}_i = \{\hat{\boldsymbol{x}}_i\}^M$ is used to initialize $\boldsymbol{X}$ in the optimization process (i.e., label of $\boldsymbol{X}$)), and probability

$$p(\boldsymbol{X}_i, \boldsymbol{\alpha}_i, \boldsymbol{\beta}_i | \boldsymbol{Y}_i, \boldsymbol{U}_i, \hat{\boldsymbol{X}}_i) \propto p(\boldsymbol{Y}_i | \boldsymbol{X}_i, \boldsymbol{\beta}_i) p(\boldsymbol{X}_i | \boldsymbol{U}_i, \boldsymbol{\alpha}_i) p(\boldsymbol{X}_i | \hat{\boldsymbol{X}}_i) p(\boldsymbol{\alpha}_i) p(\boldsymbol{\beta}_i) \tag{6.3}$$

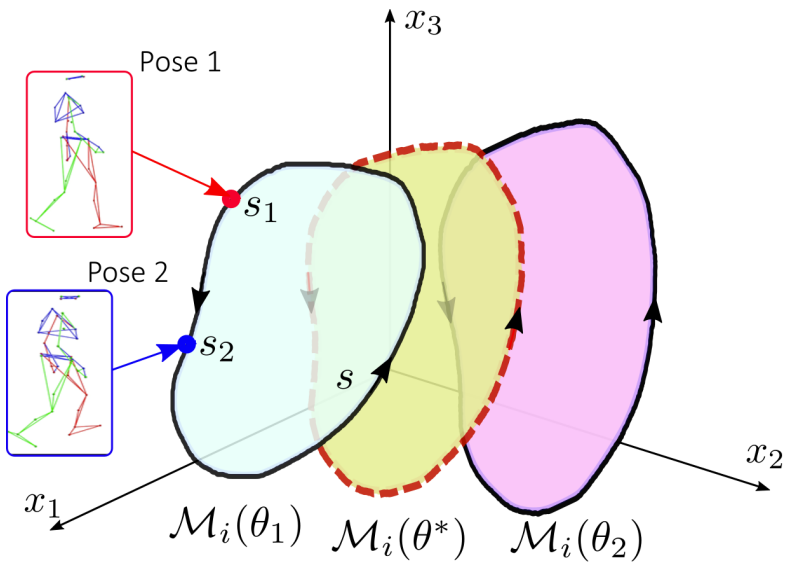

Figure 6.4: Schematic of the learned manifolds $\mathcal{M}_i(\theta_1)$ and $\mathcal{M}_i(\theta_2)$ that are obtained at slope angles θ_1 and θ_2 for activity a_i. Manifold $\mathcal{M}_i(\theta^*)$ is an estimated from interpolation from $\mathcal{M}_i(\theta_1)$ and $\mathcal{M}_i(\theta_2)$.

It is known that nearby points in the joint angle space are likely located close together in the latent space from manifold learning results [118]. Therefore, we consider that the level curves that belong the same activity share the same topological shapes in the

latent space with small variations. Fig. 6.4 further illustrates the above-discussed learned motion manifold concept. Manifolds $\mathcal{M}_i(\theta_1)$ and $\mathcal{M}_i(\theta_2)$ are obtained respectively by training the GPDM models with data sets at slope angles θ_1 and θ_2 for activity a_i. To estimate the manifold $\mathcal{M}_i(\theta^*)$ at any given slope angle $\theta^* = \gamma\theta_1 + (1-\gamma)\theta_2$, where $0 \leq \gamma \leq 1$ is weight factor, we interpolate from $\mathcal{M}_i(\theta_1)$ and $\mathcal{M}_i(\theta_2)$ as shown in Fig. 6.4. Once GPDM $\mathcal{M}_i(\theta^*)$ is obtained from activity a_i on surface with slope angle θ^*, with the gait phase variable s, latent state $\boldsymbol{x}_i(s)$ is predicted by the state dynamics and thus joint angles $\boldsymbol{y}_i(s)$ by the output equation of (6.1).

6.4 Experimental Results

In this chapter, we only consider upper- and lower-limb joint angles in the sagittal plane, and 12 joint angles are captured in the study. In the GPDM models, the latent space dimension is taken $d = 3$ and the dimension of the joint angle space is $D = 12$. The total number of walking activity is $N = 4$ (i.e., walking on level surface, up the slope, transverse the slope, and down the slope) and the slope angle is considered within 15 degs.

Fig. 6.5 shows the confusion matrix for walking activity detection algorithm and the overall detection accuracy is 96.73%. The model can successfully detect each individual activity with more than 95% accuracy. Fig. 6.6 further illustrates the performance of activity predictions on a sample of a test data for four activities. The blue spikes in the figure indicate false classifications by the LSTM-model. Only occasional false classifications occur between walking on the level surface and walking up or down the slope, due to the closest similarity among these gaits.

To validate the feasibility of our method, gait propagation and human joint angles are estimated and compared with actual values calculated from motion capture system. Twelve human joint angles from lower- and upper-limbs were selected for validation in our application, namely, left and right side hip, knee, ankle, shoulder, elbow and wrist

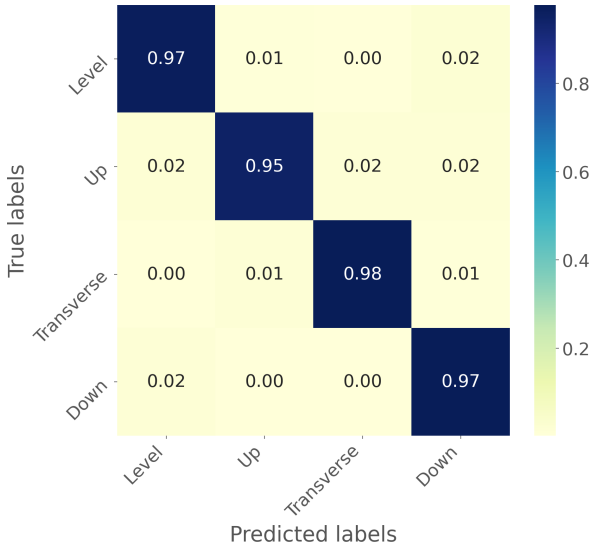

Figure 6.5: Confusion matrix for classification of four different activities (walking on the level surface, up the slope, transverse the slope, and down the slope).

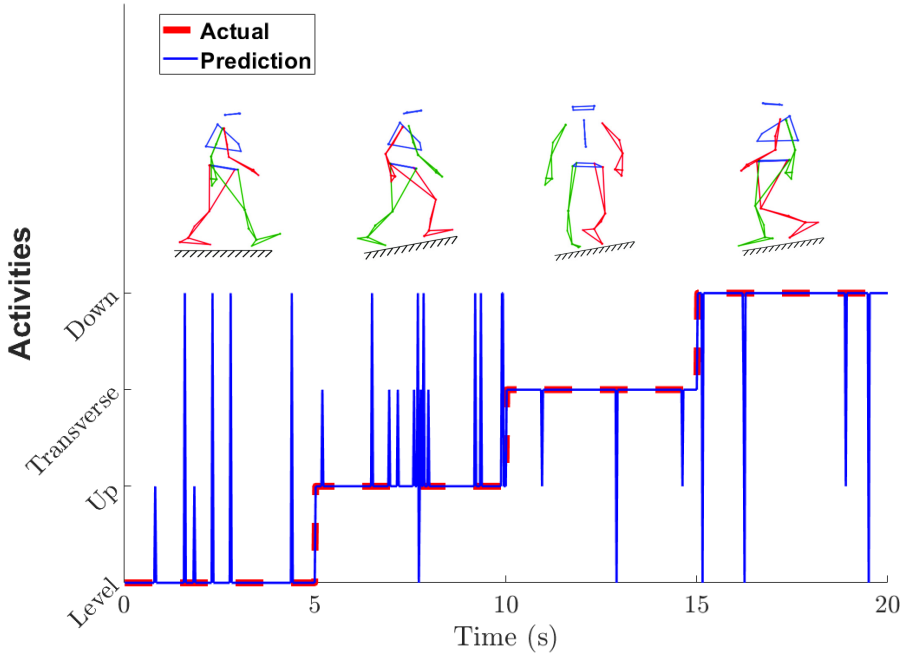

Figure 6.6: Comparison of the activity predictions with the actual one for walking on a 10 deg slopped surface. Shown are rare occasional misclassification that occur due to similarities between those gaits, due to the small slope angle.

limb joints. Fig. 6.7(a) shows the gait phase prediction from the LSTM model for five complete gait cycles of a subject walking on level surface. A representative length of

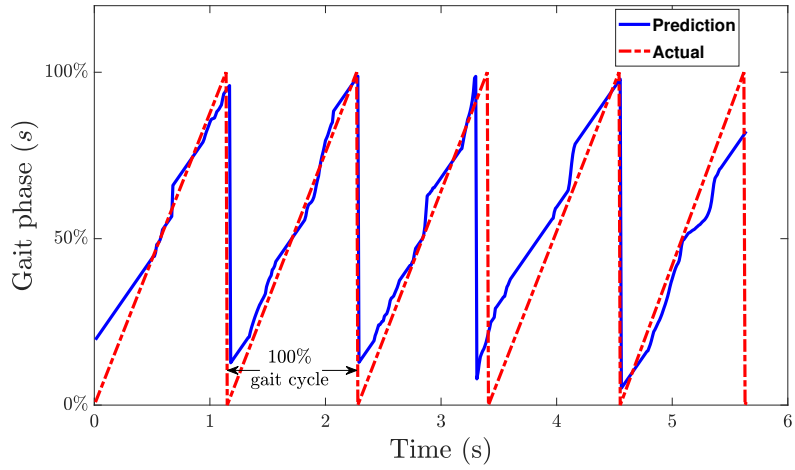

(a)

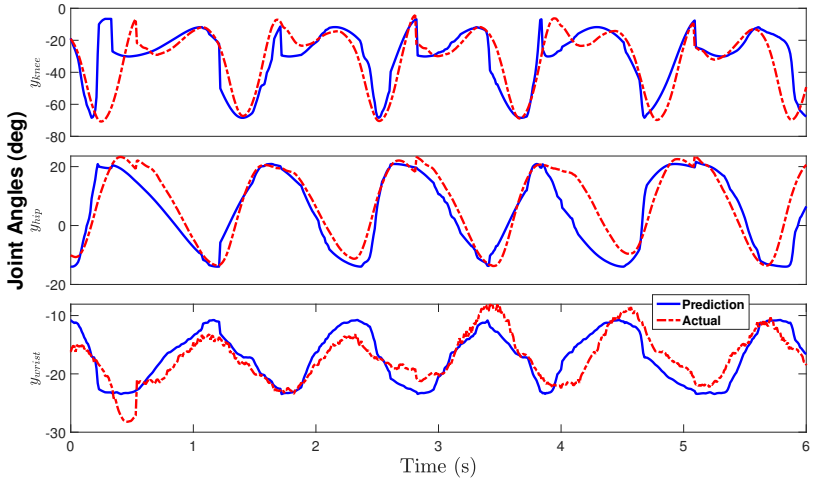

(b)

Figure 6.7: Gait phase and joint angle profile of a representative subject during level surface walking. (a) Predicted gait phases (blue solid lines) compared with the actual gait phases (red dash-dotted lines). (b) Predicted (blue solid lines) and actual (red dash-dotted lines) angles of the knee (ϕ_{knee}), hip (ϕ_{hip}) and wrist (ϕ_{wrist}) joints.

a gait cycle is marked in Fig. 6.7(a), as the gait phase variable s increases from 0 to 100%. In general, gait phase prediction was less accurate at the start of each stride, and it however convalesces as the gait propagates. Fig. 6.7(b) illustrates three selected joint angles (knee, hip, and wrist) from all twelve joints to demonstrate the performance of the pose estimation. The estimation results match more closely with the joints that are closer to the IMU location; see knee angle results in the top plot of the figure. On the

other hand, the errors for wrists (the bottom plot) show slight increase in discrepancies.

Additionally, Table 6.1 lists the overall mean absolute errors of all joint angles for each activity with respect to different slope angles. The joint angle errors were calculated and averaged from all 12 joints during all the gait phase, thus from 0% to 100 %. The error is the highest when the subjects walk down the slope, which may result from the fact that walking down the slope may be confused with that on the flat surface when the slope angle is small as seen in Fig. 6.5. This results agree with the conclusion in [41]. Table 6.1 also includes results of the joint angle estimation error for the walking gaits on two sloped surfaces (8 and 12 degs) which used manifold interpolation approach. Note that the data from these two tests were not present in the original training data. The resultant average joint angle estimation errors are slightly higher compared to those for the "trained" slope angles used in the data collection. In Table 6.1, we also list the accuracy of the slope angle estimation results. The average slope angle estimation error is around 3.4 degs and standard derivation is around 2.2 degs. The estimation results are not highly accurate and one possible reason is that the training data set sizes are not large enough. We are currently working to improve these results.

Table 6.1: Mean absolute errors of joint angles for all subjects and slope angle estimation during different activities.

	Learned model			Interpolated	
Slope Angle / Activity	5°	10°	15°	8°	12°
Up Slope	6.88°	8.00°	6.32°	12.13°	11.07°
Transverse	5.35°	6.15°	5.49°	10.86°	10.25°
Down Slope	8.95°	5.80°	7.31°	12.30°	10.52°
Level	5.39°				
Slope Angle Estimation	$4.02 \pm 2.59°$	$2.67 \pm 2.49°$	$3.01 \pm 1.51°$	$2.19 \pm 3.04°$	$4.14 \pm 1.58°$

Furthermore, Fig. 6.8 shows the mean joint angle errors of three selected limb joints with their variances over different slope angles ($\theta = 5, 10$ and 15 degs) from all subjects

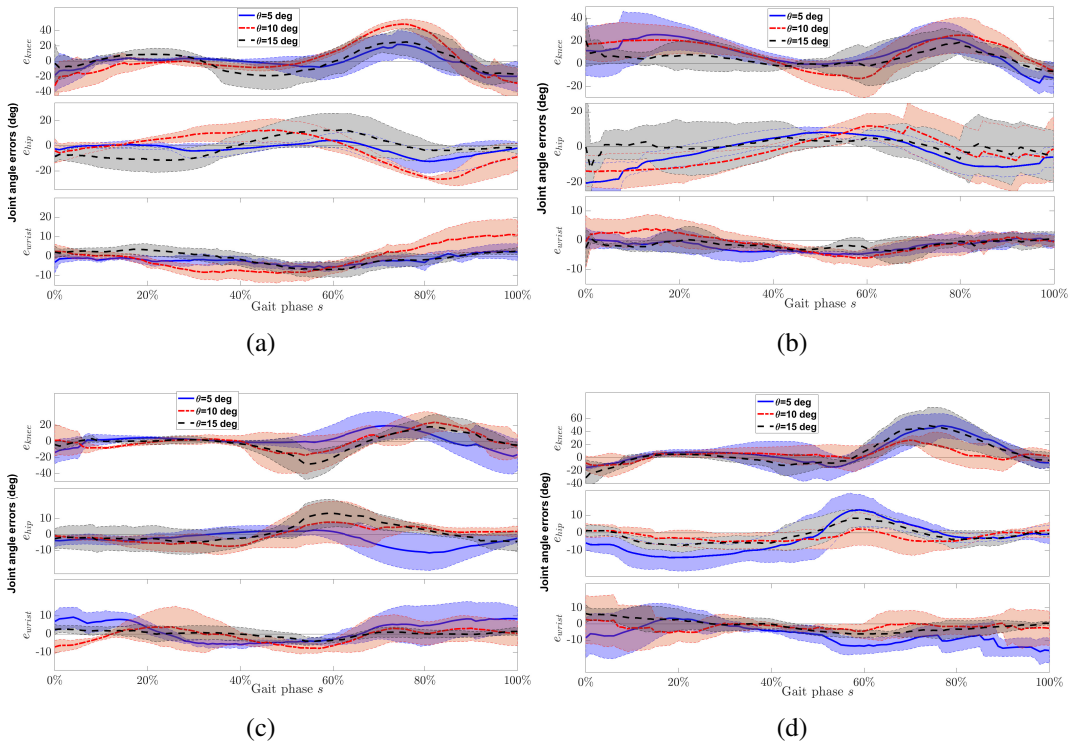

Figure 6.8: Comparison of the joint angle error profiles for variable slope angles ($\theta = 5, 10, 15$ degs) during different activities. Walking (a) on flat surface, (b) up the slope, (c) transverse the slop, and (d) down the slope. Knee (e_{knee}), hip (e_{hip}) and (e_{wrist}) wrist mean absolute joint angle error profiles are shown on the top, middle, and bottom subfigures, respectively. The thick curves are the mean error profiles, while the shaded ares show the one standard deviation around the mean values of all subject experiments.

data. The joint angle error profiles of walking on flat surface, up the slope, transverse the slope and down the slope are shown in Fig. 6.8(a) to 6.8(d), respectively. The knee and hip joint angle had larger mean errors with higher variance in certain portion that was due to the detection latency and their higher ranges of motion compared to wrist angle when the subject walked up the slope. The accuracy of the joint angle reconstruction using several IMUs for various non-walking 3D human motions in [53] was approximately 16 degs. The preliminary results in this work show that the proposed approach achieved a similar accuracy for planar human walking pose estimation using a single IMU.

We evaluated the latency of our framework for different layers of prediction by feed-

ing the pre-recorded unknown data offline to the network in real-time. The latency of activity detection was about 2.2 ms, the slope angle detection latency was about 2.58 ms, and the latency of pose estimation was about 13.82 ms. Therefore, the overall latency of the algorithm was approximately 18.6 ms. The estimation errors in the gait phase and joint angles might result from several plausible sources. First, the training data quality and size might restrict the learning model accuracy. We only considered using mean values of gait cycles for each activity for full-body pose estimation. This requires a specialized tuning of the GPDM hyperparameters. Finally, instead of using the manifold interpolation for any estimated slope angles, we might be able to further use topological constraints to enhance the GPDM model accuracy.

6.5 Discussion

In 6.4, we presented walking activity classification, slope angle estimation and human joint angle estimation for different walking activities based on machine learning methods. Comparing with the work [41], similar results in the walking activity classification and slope angle estimation were presented. In Young's paper, multiple sensors are used for prediction including IMUs, EMGs and goniometers, while in our implementation, only a single IMU is used for prediction. Neural networks were used for prediction by Young's group, while we applied our algorithms using LSTM based recurrent neural networks. LSTM based neural networks are especially good for time series data prediction where the input data spans over long sequences. This feature allows us to use only one IMU data to detect and predict human motion. Other than above mentioned estimation techniques, we further estimated the human body joint angles for full body motion based on GPDM. A gait phase variable was estimated on latent space and by using GPDM the latent space was mapped to joint angle space. This part was not discussed in Young's paper.

In Young's paper, four different types of walking (treadmill, level ground, ramps,

and stairs walking) were discussed. The accuracy of the detection was about 98% on average with higher accuracy on steady state and lower on transition state. Our method achieved similar results in the classification of activities and the overall detection accuracy of our walking activity detection algorithm was 96.73%. For the slope angle estimation, Young's paper presented lower detection error about 1.25 degrees while our results showed a 3.4 degrees error. This error might be due to the use of only one IMU data which is not as accurate as the results from sensor fusion.

The merit of the proposed method is that we utilized single IMU data for real-time gait detection and body pose estimation. With pretrained LSTM based RNN model, this method can be applied to activity classification, slope estimation and body joint angle estimation in real-time. The algorithms was running on a GPU-based desktop which can reach up to 100 Hz detection rate.

There are a few limitations of our work for the gait detection and estimation. Our estimation scheme only applies to periodical walking due to the nature of GPDM in latent space. For periodical motion, the latent space curve is a closed curve which can map the low dimensional space variables to the high dimensional space joint angles. The slope angle estimation based on one IMU data is not as accurate as in [41] which might be improved with more advanced model. The transitions between different motion activities were not considered and there was higher chance of false detection during the transitions, which results in larger errors in these activities. In this work, the model was built on the fact that subjects walk on their self-selected speed and the estimation results on varying speed is not discussed. The joint angle estimation were based on steady state walking for leveled surface and sloped surface walking. The stair walking activity was not included in this work and it might be suitable to extend to ascent and descent stair walking similar as in [119].

6.6 Summary

This chapter implemented a real-time walking gait and pose estimation framework for construction workers on flat and sloped surfaces. A combination of the LSTM-based network and GPDM was mainly used in the estimation scheme. The walking activities were predicted, and human pose was predicted with average joint angle errors of errors within 8.30 degs. The activities and slope angle were predicted first by a LSTM-based network, and the gait propagation was predicted for the corresponding activity. Another attractive property of the proposed scheme was the real-time capability with 18.6 ms latency using a single IMU attached to the distal portion of the right fibula.

Chapter 7

Conclusion and Future Work

7.1 Conclusions

This dissertation studied several common topics in physical human-robot interactions and their modeling and control system design for construction workers. We have discussed human strength estimation method using muscle synergy model, human balancing model on inclined surface, walking gait detection and prediction method using LSTM based recurrent neural networks. Based on these models, robust control systems are designed and developed for physical human-robot interactions, such as human-manipulator interactions and knee assistive device development. This dissertation takes both physical principle-based model and machine learning-based data-driven models to estimate human performance in various applications in construction site.

In this dissertation, we proposed a muscle synergy based modeling method for construction workers to reduce their WMSD risks . We presented human-robot interaction approach to estimate human physical strength capacity. We took the advantages of the muscle synergy model to estimate human upper limb strength. Multi-subject experiments were conducted to validate and demonstrate the synergy model and strength capacity estimation results. The experiments confirmed the estimated strength capacity for all subjects was mostly within 20% of the static testing results.

We also developed a muscle synergy-based force control of robotic manipulator for assist-as-needed physical human-robot interactions. The muscle synergy model and the neural network approach were used to predict the muscle activation and then estimate

human applied forces in human-robot interactions. A disturbance observer was designed to estimate the unknown external disturbance forces, and then an admittance control was applied to the manipulator to simultaneously follow human intention motion and to compensate for working load and undesired disturbances. We conducted multiple subjects experiments in both 2D and 3D workspace to demonstrate the assist-as-needed control performance and disturbance rejection.

For construction activities like standing, kneeling and walking on inclined surface, we developed several human models and designed wearable exoskeleton system to assist construction workers. We investigated the postural balance during kneeling and standing on sloped and elevated surfaces. The experimental results of center of pressure and trunk acceleration measurements showed smaller postural sway during kneeling compared to standing. These observations were held for tests on level or sloped surface as well as when subject was immersed in the low or high elevated visual environment. A postural model was developed to simulate postural sway in the anterior-posterior direction. The model and controller parameters were optimized to precisely match the experimental results. Variation of model parameters with respect to particular test conditions provided insight on relationship on human neural balance postural control and sensory system.

Furthermore, a wearable assistive system design was presented in kneeling assistance for construction workers. We developed a novel controller design to assist construction workers using an improved design of a bilateral knee exoskeleton with enhanced torque capabilities and wearable, non-tethered configuration. Several wearable and stationary sensor suites were used to measure subjects' kinetics, kinematics, and physiological parameters during kneeling tasks. The results showed reductions in muscle activation of knee and hip extensor muscles during standing from kneeling with the highest reduction under high-torque assistance on highly slopped surfaces. Measurements of ground reaction forces showed reductions in knee pressure with increased torque assistance. The human subject testing results validated the effectiveness of the

device with the goal to reduce and alleviate WMSD risk for construction workers when performing kneeling tasks on level and sloped surfaces.

Lastly, this dissertation implemented a real-time walking gait and pose estimation framework for construction workers on flat and sloped surfaces. A combination of the LSTM-based network and GPDM was mainly used in the estimation scheme. The walking activities were predicted by a LSTM-based neural network, and gait propagation and human pose was predicted. Real-time detection and estimation results are presented with minimum latency using only a single IMU attached to the distal portion of fibula.

7.2 Future Work

There are a few research directions that follow this dissertation's work. Chapters 2 and 3 have proposed a human force estimation scheme using muscle synergy model and developed a disturbance rejection controller for assisting construction workers during physical human-robot interactions. It is expected that such controller design could be extended to more dynamic environment with agile human motion. Due to the hardware limitation, the movement speed of human arm in the lateral was slower compared with the other two directions which may results in the higher errors in 3D experiments. A further study is required for interactions between human and a more agile robot in the workspace.

Chapter 5 proposed a kneeling detection algorithm which used a simplified threshold based method. The algorithm can be improved for accurate, real-time detection of complex kneeling gait events during construction tasks. The design of the assistive knee device can be also improved to avoid knee and device touching the pressure mat. A specific effort will have to be made to adjust device to each individual subject to guarantee a proper fit and comfort while wearing the device. More human subjects, especially construction workers, with various height and weight can be involved into the research, and it could generate more accurate and robust control system. It would be valuable to

test the wearable assistive devices with professional construction workers at industrial sites.

Chapter 6 discussed human gait detection based on single IMU data. Besides the motion activities mentioned in this dissertation, more common activities, such as walking on stairs and asymmetrical motions, can be added into the experimental protocol. Due to the nature of machine learning algorithms, a more detailed analysis with increased number of subjects is required to further investigate our observations. In particular, a larger sample size is required to be able to introduce the randomized sequence of trials. Randomization could help eliminate any possible adaptation effects due to the subjects experiencing same or similar visual scene observed previously. All of these research topics can be the future works of this dissertation.

References

[1] Bureau of Labor Statistics, "National Census of Fatal Occupational Injuries in 2019," Bureau of Labor Statistics, Washington, DC, Tech. Rep., 2020.

[2] X. Wang, X. S. Dong, S. D. Choi, and J. Dement, "Work-related musculoskeletal disorders among construction workers in the united states from 1992 to 2014," *Occup. Environ. Med.*, vol. 74, no. 5, pp. 374–380, 2017.

[3] X. Dong, X. Wang, and R. Katz, *The Construction Chart Book – The U.S. Construction Industry and Its Workers*, 6th. Silver Spring, MD: CPWR, 2018.

[4] G. M. Waehrer, X. S. Dong, T. Miller, E. Haile, and Y. Men, "Costs of occupational injuries in construction in the united states," *Accident Analysis and Prevention*, vol. 39, no. 6, pp. 1258–1266, 2007.

[5] K. T. Palmer, "Occupational activities and osteoarthritis of the knee," *British Med. Bull.*, vol. 102, no. 1, pp. 147–170, 2012.

[6] J. M. Inouye and F. J. Valero-Cuevas, "Muscle synergies heavily influence the neural control of arm endpoint stiffness and energy consumption," *PLoS Comput. Biol.*, vol. 12, no. 2, e1004737, 2016.

[7] K. Chen, Y. Zhang, J. Yi, and T. Liu, "An integrated physical-learning model of physical human-robot interactions with application to pose estimation in bikebot riding," *Int. J. Robot. Res.*, vol. 35, no. 12, pp. 1459–1476, 2016.

[8] M. Bergamasco and H. Herr, "Human–robot augmentation," in *Springer Handbook of Robotics*, Berlin, Germany: Springer, 2016, pp. 1875–1906.

[9] E. T. Wolbrecht, V. Chan, D. J. Reinkensmeyer, and J. E. Bobrow, "Optimizing compliant, model-based robotic assistance to promote neurorehabilitation," *IEEE Trans. Neural Syst. Rehab. Eng.*, vol. 16, no. 3, pp. 286–297, 2008.

[10] M. G. Carmichael and D. Liu, "Estimating physical assistance need using a musculoskeletal model," *IEEE Trans. Biomed. Eng.*, vol. 60, no. 7, pp. 1912–1919, 2013.

[11] J. Ueda, D. Ming, V. Krishnamoorthy, M. Shinohara, and T. Ogasawara, "Individual muscle control using an exoskeleton robot for muscle function testing," *IEEE Trans. Neural Syst. Rehab. Eng.*, vol. 18, no. 4, pp. 339–350, 2010.

[12] H. K. Kim, J. M. Carmena, S. J. Biggs, T. L. Hanson, M. A. Nicolelis, and M. A. Srinivasan, "The muscle activation method: An approach to impedance control of brain-machine interfaces through a musculoskeletal model of the arm," *IEEE Trans. Biomed. Eng.*, vol. 54, no. 8, pp. 1520–1529, 2007.

[13] G. Torres-Oviedo and L. H. Ting, "Muscle synergies characterizing human postural responses," *J. Neurophysiol.*, vol. 98, no. 4, pp. 2144–2156, 2007.

[14] M. C. Tresch and A. Jarc, "The case for and against muscle synergies," *Curr. Opin. Neurobiol.*, vol. 19, no. 6, pp. 601–607, 2009.

[15] A. d'Avella, A. Portone, L. Fernandez, and F. Lacquaniti, "Control of fast-reaching movements by muscle synergy combinations," *J. Neurosci.*, vol. 26, no. 30, pp. 7791–7810, 2006.

[16] J. L. McKay and L. H. Ting, "Functional muscle synergies constrain force production during postural tasks," *J. Biomech.*, vol. 41, no. 2, pp. 299–306, 2008.

[17] Y. Li and S. S. Ge, "Human–robot collaboration based on motion intention estimation," *IEEE/ASME Trans. Mechatronics*, vol. 19, no. 3, pp. 1007–1014, 2013.

[18] Q. Liu, L. Ma, Q. Ai, K. Chen, and W. Meng, "Knee joint angle prediction based on muscle synergy theory and generalized regression neural network," in *Proc. IEEE/ASME Int. Conf. Adv. Intelli. Mechatronics*, Auckland, New Zealand, 2018, pp. 28–32.

[19] P. H. Chang, K. Park, S. H. Kang, H. I. Krebs, and N. Hogan, "Stochastic estimation of human arm impedance using robots with nonlinear frictions: An experimental validation," *IEEE/ASME Trans. Mechatronics*, vol. 18, no. 2, pp. 775–786, 2012.

[20] F. Ficuciello, L. Villani, and B. Siciliano, "Variable impedance control of redundant manipulators for intuitive human–robot physical interaction," *IEEE Trans. Robotics*, vol. 31, no. 4, pp. 850–863, 2015.

[21] H. Modares, I. Ranatunga, F. L. Lewis, and D. O. Popa, "Optimized assistive human–robot interaction using reinforcement learning," *IEEE Trans. Cybern.*, vol. 46, no. 3, pp. 655–667, 2016.

[22] B. Yu, R. B. Gillespie, J. S. Freudenberg, and J. A. Cook, "Human control strategies in pursuit tracking with a disturbance input," in *Proc. IEEE Conf. Decision Control*, Los Angeles, CA, 2014, pp. 3795–3800.

[23] D. A. Winter, A. E. Patla, F. Prince, M. Ishac, and K. Gielo-Perczak, "Stiffness control of balance in quiet standing," *J. Neurophysiol.*, vol. 80, pp. 1211–1221, 1998.

[24] R. J. Peterka, C. F. Murchison, L. Parrington, P. C. Fino, and L. A. King, "Implementation of a central sensorimotor integration test for characterization of human balance control during stance," *Front. Neurology*, vol. 9, 2018, article 1045.

[25] R. A. Mezzarane and A. F. Kohn, "Postural control during kneeling," *Exp. Brain Res.*, vol. 187, pp. 395–405, 2008.

[26] A. Bhattacharya, P. Succop, L. Kincl, M. L. Lu, and A. Bagchee, "Postural stability during task performance on elevated and/or inclined surfaces," *Occup. Ergon.*, vol. 3, pp. 83–97, 2002.

[27] H. Hsiao, P. Simeonov, B. Dotson, D. Ammons, T.-Y. Kau, and S. Chiou, "Human responses to augmented virtual scaffolding models," *Ergonomics*, vol. 48, no. 10, pp. 1223–1242, 2005.

[28] I. Okpala, C. Nnaji, and A. A. Karakhan, "Utilizing emerging technologies for construction safety risk mitigation," *Pract. Period. Struct. Des. Constr.*, vol. 25, no. 2, 2020, article 04020002.

[29] S. Yu *et al.*, "Quasi-direct drive actuation for a lightweight hip exoskeleton with high backdrivability and high bandwidth," *IEEE/ASME Trans. Mechatronics*, vol. 25, no. 4, pp. 1794–1802, 2020.

[30] S. Chen *et al.*, "Wearable knee assistive devices for kneeling tasks in construction," *IEEE/ASME Trans. Mechatronics*, 2021.

[31] K. Hunte, S. Chen, J. Yi, and H. Su, "Assist-as-needed control of a wearable lightweight knee robotic device," in *Proc. IEEE/ASME Int. Conf. Adv. Intelli. Mechatronics*, Boston, MA, 2020, pp. 1477–1482.

[32] S. Chen, S. S. Bangaru, T. Yigit, M. Trkov, C. Wang, and J. Yi, "Real-time walking gait estimation for construction workers using a single wearable inertial measurement unit (imu)," in *Proc. IEEE/ASME Int. Conf. Adv. Intelli. Mechatronics*, Delft, Netherlands, 2021.

[33] L. B. Murphy, M. G. Cisternas, D. J. Pasta, C. G. Helmick, and E. H. Yelin, "Medical expenditures and earnings losses among us adults with arthritis in 2013," *Arthritis Care & Res.*, vol. 70, no. 6, pp. 869–876, 2018.

[34] Y. Zhang and J. M. Jordan, "Epidemiology of osteoarthritis," *Clinics in Geriat. Med.*, vol. 26, no. 3, pp. 355–369, 2010.

[35] J. Howard, V. V. Murashov, B. D. Lowe, and M.-L. Lu, "Industrial exoskeletons: Need for intervention effectiveness research," *Am. J. Ind. Med.*, vol. 63, pp. 201–208, 2019.

[36] D. Lee, B. J. Mclain, I. Kang, and A. Young, "Biomechanical comparison of assistance strategies using a bilateral robotic knee exoskeleton," *IEEE Trans. Biomed. Eng.*, 2021.

[37] T. Yan, M. Cempini, C. M. Oddo, and N. Vitiello, "Review of assistive strategies in powered lower-limb orthoses and exoskeletons," *Robot. Auton. Syst.*, vol. 64, pp. 120–136, 2015.

[38] A. J. Young and D. P. Ferris, "State of the art and future directions for lower limb robotic exoskeletons," *IEEE Trans. Neural Syst. Rehab. Eng.*, vol. 25, no. 2, pp. 171–182, 2017.

[39] S. Yu *et al.*, "Design and control of a high-torque and highly backdrivable hybrid soft exoskeleton for knee injury prevention during squatting," *IEEE Robot. Automat. Lett.*, vol. 4, no. 4, pp. 4579–4586, 2019.

[40] E. Valero, A. Sivanathan, F. Bosche, and M. Abdel-Wahab, "Musculoskeletal disorders in construction: A review and a novel system for activity tracking with body area network," *Appl. Ergon.*, vol. 54, pp. 120–130, 2016.

[41] J. Camargo, W. Flanagan, N. Csomay-Shanklin, B. Kanwar, and A. Young, "A machine learning strategy for locomotion classification and parameter estimation using fusion of wearable sensors," *IEEE Trans. Biomed. Eng.*, vol. 68, no. 5, pp. 1569–1578, 2021.

[42] S. S. Bangaru, C. Wang, and F. Aghazadeh, "Data quality and reliability assessment of wearable emg and imu sensor for construction activity recognition," *Sensors*, vol. 20, no. 18, 2020.

[43] I. Weygers, M. Kok, M. Konings, H. Hallez, H. De Vroey, and K. Claeys, "Inertial sensor-based lower limb joint kinematics: A methodological systematic review," *Sensors*, vol. 20, 2020, article 673.

[44] T. Li, L. Wang, J. Yi, Q. Li, and T. Liu, "Lower-body walking motion estimation using only two shank-mounted inertial measurement units (IMUs)," *IEEE/ASME Trans. Mechatronics*, 2021, in press.

[45] J. Lee, H. Joo, and Y. Chee, "Automatic classification of squat posture using inertial sensors: Deep learning approach," *Sensors*, vol. 20, 2020, article 361.

[46] P. F. Hendriksen, M. Korshøj, J. Skotte, and A. Holtermann, "Detection of kneeling and squatting during work using wireless triaxial accelerometers," *Ergonomics*, vol. 63, no. 5, pp. 607–617, 2020.

[47] X. Yan, H. Li, A. R. Li, and H. Zhang, "Wearable IMU-based real-time motion warning system for construction workers' musculoskeletal disorders prevention," *Automat. Constr.*, vol. 74, pp. 2–11, 2017.

[48] K. Kim and Y. K. Cho, "Effective inertial sensor quantity and locations on a body for deep learning-based worker's motion recognition," *Automat. Constr.*, vol. 113, 2020, article 103126.

[49] J. Figureiredo, P. Félix, L. Costa, J. C. Moreno, and C. P. Santos, "Gait event detection in controlled and real-life situations: Repeated measures from healthy subjects," *IEEE Trans. Neural Syst. Rehab. Eng.*, vol. 26, no. 10, pp. 1945–1956, 2018.

[50] J. Yang *et al.*, "Machine learning based adaptive gait phase estimation using inertial measurement sensors," in *Proc. ASME Design Med. Dev. Conf.*, Paper #DMD2019-3266, Minneapolis, MN, 2019.

[51] Y. Huang *et al.*, "Real-time intended knee joint motion prediction by deep-recurrent neural networks (RNNs)," *IEEE Sensors J.*, vol. 19, no. 23, pp. 11 503–11 509, 2019.

[52] I. Kang, P. Kunapuliu, and A. J. Young, "Real-time neural network-based gait phase estimation using a robotic hip exoskeleton," *IEEE Trans. Med. Robot. Bionics*, vol. 2, no. 1, pp. 28–37, 2020.

[53] Y. Huang, M. Kaufmann, E. Aksan, M. J. Black, O. Hilliges, and G. Pons-Moll, "Deep inertial poser: Learning to reconstruct human pose from sparse inertial measurements in real time," *ACM Trans. Graph.*, vol. 37, no. 6, 2018, article 185.

[54] C. Mousas, "Full-body locomotion reconstruction of virtual characters using a single inertial measurement unit," *Sensors*, vol. 17, 2017, article 2589.

[55] D. Holden, T. Komura, and J. Saito, "Phase-functioned neural networks for character control," *ACM Trans. Graph.*, vol. 36, no. 4, 2017, article 42.

[56] H. Hatze, "A myocybernetic control model of skeletal muscle," *Biol. Cybern.*, vol. 25, no. 2, pp. 103–119, 1977.

[57] A. Erdemir, S. McLean, W. Herzog, and A. J. van den Bogert, "Model-based estimation of muscle forces exerted during movements," *Clin Biomech.*, vol. 22, no. 2, pp. 131–154, 2007.

[58] B. A. Garner and M. G. Pandy, "Estimation of musculotendon properties in the human upper limb," *Ann. Biomed. Eng.*, vol. 31, no. 2, pp. 207–220, 2003.

[59] A. M. Khan, D.-w. Yun, M. A. Ali, J. Han, K. Shin, and C. Han, "Adaptive impedance control for upper limb assist exoskeleton," in *Proc. IEEE Int. Conf. Robot. Autom.*, Seattle, WA, 2015, pp. 4359–4366.

[60] P. Y. Li and R. Horowitz, "Control of smart exercise machines. ii. self-optimizing control," *IEEE/ASME Trans. Mechatronics*, vol. 2, no. 4, pp. 248–258, 1997.

[61] J. Zhang and C. C. Cheah, "Passivity and stability of human–robot interaction control for upper-limb rehabilitation robots," *IEEE Trans. Robotics*, vol. 31, no. 2, pp. 233–245, 2015.

[62] S. Chen, J. Yi, and T. Liu, "Strength capacity estimation of human upper limb in human-robot interactions with muscle synergy models," in *Proc. IEEE/ASME Int. Conf. Adv. Intelli. Mechatronics*, Auckland, New Zealand, 2018, pp. 1051–1056.

[63] A. d'Avella, P. Saltiel, and E. Bizzi, "Combinations of muscle synergies in the construction of a natural motor behavior," *Nature*, vol. 6, no. 3, pp. 300–308, 2003.

[64] R. Vinjamuri, M. Sun, C.-C. Chang, H.-N. Lee, R. J. Sclabassi, and Z.-H. Mao, "Dimensionality reduction in control and coordination of the human hand," *IEEE Trans. Biomed. Eng.*, vol. 57, no. 2, pp. 284–295, 2009.

[65] L. H. Ting and J. M. Macpherson, "A limited set of muscle synergies for force control during a postural task," *J. Neurophysiol.*, vol. 93, no. 1, pp. 609–613, 2005.

[66] F. E. Zajac, "Muscle and tendon properties models scaling and application to biomechanics and motor," *Crit Rev Biomed Eng*, vol. 17, no. 4, pp. 359–411, 1989.

[67] R. S. Razavian, N. Mehrabi, and J. McPhee, "A model-based approach to predict muscle synergies using optimization: Application to feedback control," *Front. Comput. Neurosci.*, vol. 9, p. 121, 2015.

[68] M. W. Spong, S. Hutchinson, and M. Vidyasagar, *Robot Modeling and Control*. Wiley New York, 2006.

[69] K. P. Tee, R. Yan, and H. Li, "Adaptive admittance control of a robot manipulator under task space constraint," in *Proc. IEEE Int. Conf. Robot. Autom.*, Anchorage, AK, 2010, pp. 5181–5186.

[70] M. G. Carmichael and D. Liu, "Admittance control scheme for implementing model-based assistance-as-needed on a robot," in *Proc. IEEE Int. Conf. Eng. Med. Bio. Soc.*, Osaka, Japan, 2013, pp. 870–873.

[71] P. Wang and J. Yi, "Dynamic stability of a rider-bicycle system: Analysis and experiments," in *Proc. Amer. Control Conf.*, Chicago, IL, 2015, pp. 1161–1166.

[72] J. L. Emken, R. Benitez, and D. J. Reinkensmeyer, "Human-robot cooperative movement training: Learning a novel sensory motor transformation during walking with robotic assistance-as-needed," *J. Neuroeng. Rehabil.*, vol. 4, no. 1, p. 8, 2007.

[73] A. Tran, "Robot confidence modeling and role change in physical human-robot collaboration," Ph.D. dissertation, Faculty Eng. Inform. Tech., Univ. Tech. Sydney, Sydney, Australia, 2019.

[74] S. S. Ge and C. Wang, "Adaptive neural control of uncertain mimo nonlinear systems," *IEEE Trans. Neural Networks*, vol. 15, no. 3, pp. 674–692, 2004.

[75] R. Ikeura and H. Inooka, "Variable impedance control of a robot for cooperation with a human," in *Proc. IEEE Int. Conf. Robot. Autom.*, Atlanta, GA, 1995, pp. 3097–3102.

[76] S. Calinon, I. Sardellitti, and D. G. Caldwell, "Learning-based control strategy for safe human-robot interaction exploiting task and robot redundancies," in *Proc. IEEE/RSJ Int. Conf. Intell. Robot. Syst.*, Taipei, Taiwan, 2010, pp. 249–254.

[77] E. Gribovskaya, A. Kheddar, and A. Billard, "Motion learning and adaptive impedance for robot control during physical interaction with humans," in *Proc. IEEE Int. Conf. Robot. Autom.*, Shanghai, China, 2011, pp. 4326–4332.

[78] A. Kubo, S. Hagio, B. Kibushi, T. Moritani, and M. Kouzaki, "Action direction of muscle synergies in voluntary multi-directional postural control," *Front. Hum. Neurosci.*, vol. 11, p. 434, 2017.

[79] D. G. Lloyd and T. F. Besier, "An EMG-driven musculoskeletal model to estimate muscle forces and knee joint moments in vivo," *J. Biomech.*, vol. 36, no. 6, pp. 765–776, 2003.

[80] R. Sharif Razavian, N. Mehrabi, and J. McPhee, "A model-based approach to predict muscle synergies using optimization: Application to feedback control," *Front. Comput. Neurosci.*, vol. 9, 2015, artical 121.

[81] W. J. Gallagher, "Modeling of operator action for intelligent control of haptic human-robot interfaces," Ph.D. dissertation, Georgia Institute of Technology, 2013.

[82] B. Ghannadi, N. Mehrabi, R. S. Razavian, and J. McPhee, "Nonlinear model predictive control of an upper extremity rehabilitation robot using a two-dimensional human-robot interaction model," in *Proc. IEEE/RSJ Int. Conf. Intell. Robot. Syst.*, Vancouver, Canada, 2017, pp. 502–507.

[83] K. P. Tee, E. Burdet, C.-M. Chew, and T. E. Milner, "A model of force and impedance in human arm movements," *Biol. Cybern.*, vol. 90, no. 5, pp. 368–375, 2004.

[84] C. T. Landi, F. Ferraguti, L. Sabattini, C. Secchi, M. Bonfè, and C. Fantuzzi, "Variable admittance control preventing undesired oscillating behaviors in physical human-robot interaction," in *Proc. IEEE/RSJ Int. Conf. Intell. Robot. Syst.*, Vancouver, Canada, 2017, pp. 3611–3616.

[85] G. Ganesh, A. Albu-Schäffer, M. Haruno, M. Kawato, and E. Burdet, "Biomimetic motor behavior for simultaneous adaptation of force, impedance and trajectory in interaction tasks," in *Proc. IEEE Int. Conf. Robot. Autom.*, Anchorage, AK, 2010, pp. 2705–2711.

[86] J. Han, "From PID to active disturbance rejection control," *IEEE Trans. Ind. Electron.*, vol. 56, no. 3, pp. 900–906, 2009.

[87] H. Hsiao and P. Simeonov, "Preventing falls from roofs: A critical review," *Ergonomics*, vol. 44, no. 5, pp. 537–561, 2001.

[88] P. I. Simeonov, H. Hsiao, B. W. Dotson, and D. E. Ammons, "Control and perception of balance at elevated and sloped surfaces," *Human Factors*, vol. 45, no. 1, pp. 136–147, 2003.

[89] T. W. Cleworth, B. C. Horslen, and M. G. Carpenter, "Influence of real and virtual heights on standing balance," *Gait Posture*, vol. 36, pp. 172–176, 2012.

[90] F. Bosché, M. Abdel-Wahab, and L. Carozza, "Towards a mixed reality system for construction trade training," *J. Comput. Civ. Eng.*, vol. 30, no. 2, 2016, article 04015016.

[91] X. Li and W. Yi and H.-L. Chi and X. Wang and A. P. C. Chan, "A critical review of virtual and augmented reality (VR/AR) applications in construction safety," *Automat. Constr.*, vol. 86, pp. 150–162, 2018.

[92] J. M. D. Delgado, L. Oyedele, T. Beach, and P. Demian, "Augmented and virtual reality in construction: Drivers and limitations for industry adoption," *J. Constr. Eng. Manage.*, vol. 146, no. 7, 2020, article 04020079.

[93] Y. Shi, J. Du, C. R. Ahn, and E. Ragan, "Impact assessment of reinforced learning methods on construction workers' fall risk behavior using virtual reality," *Automat. Constr.*, vol. 104, pp. 197–214, 2019.

[94] A. J. Solomon, J. V. Jacobs, K. V. Lomond, and S. M. Henry, "Detection of postural sway abnormalities by wireless inertial sensors in minimally disabled patients with multiple sclerosis: A case–control study," *J. Neuroeng. Rehab*, vol. 12, no. 1, pp. 1–9, 2015.

[95] S. Kim *et al.*, "Potential of exoskeleton technologies to enhance safety, health, and performance in construction: Industry perspectives and future research directions," *IISE Trans. Occup. Erg. Human Factors*, vol. 7, pp. 185–191, 2019.

[96] http://www.suitx.com.

[97] J. K. Hofer, R. Gejo, M. H. McGarry, and T. Q. Lee, "Effects on tibiofemoral biomechanics from kneeling," *Curr. Biol.*, vol. 26, no. 6, pp. 605–611, 2011.

[98] T. Kajaks and P. Costigan, "The effect of sustained static kneeling on kinetic and kinematic knee joint gait parameters," *Appl. Ergon.*, vol. 46, pp. 224–230, 2015.

[99] S. P. Breloff *et al.*, "Are knee savers and knee pads a viable intervention to reduce lower extremity musculoskeletal disorder risk in residential roofers?" *Int. J. Ind. Ergonom.*, vol. 74, p. 102 868, 2019.

[100] H. Xu, S. Jampala, D. Bloswick, J. Zhao, and A. Merryweather, "Evaluation of knee joint forces during kneeling work with different kneepads," *Appl. Ergon.*, vol. 58, pp. 308–313, 2017.

[101] T. Kurayama *et al.*, "A comparison of the movement characteristics between the kneeling gait and the normal gait in healthy adults," *Gait Posture*, vol. 37, no. 3, pp. 402–407, 2013.

[102] I. Awolusi, E. Marks, and M. Hallowell, "Wearable technology for personalized construction safety monitoring and trending: Review of applicable devices," *Automat. Constr.*, vol. 85, pp. 96–106, 2018.

[103] Y. Ma, X. Wu, J. Yi, C. Wang, and C. Chen, "A review on human-exoskeleton coordination towards lower limb robotic exoskeleton systems," *Int. J. Robot. Automat.*, vol. 34, no. 4, pp. 431–451, 2019.

[104] M. K. Shepherd and E. J. Rouse, "Design and validation of a torque-controllable knee exoskeleton for sit-to-stand assistance," *IEEE/ASME Trans. Mechatronics*, vol. 22, no. 4, pp. 1695–1704, 2017.

[105] P. M. Wensing, A. Wang, S. Seok, D. Otten, J. Lang, and S. Kim, "Proprioceptive actuator design in the MIT cheetah: Impact mitigation and high-bandwidth physical interaction for dynamic legged robots," *IEEE Trans. Robotics*, vol. 33, no. 3, pp. 509–522, 2017.

[106] W. Johnson, *Roofers Handbook*. Carlsbad, CA: Craftsman Book Company, 1976.

[107] U. S. Bureau of Labor Statistics (BLS) 2019, *Labor force statistics from the current population survey*, https://www.bls.gov/cps/cpsaat11.htm.

[108] M. Trkov, K. Chen, and J. Yi, "Bipedal model and extended hybrid zero dynamics of human walking with foot slips," *ASME J. Computat. Nonlinear Dyn.*, vol. 14, no. 10, 2019, article 101002.

[109] D. A. Winter, *Biomechanics and Motor Control of Human Movement*, 2nd. New York, NY: John Wiley & Sons, 2009.

[110] C. R. Ahn, S. Lee, C. Sun, H. Jebelli, K. Yang, and B. Choi, "Wearable sensing technology applications in construction safety and health," *J. Constr. Eng. Manage.*, vol. 145, no. 11, 2019, article 03119007.

[111] E. Valero and A. Sivanathan and F. Bosche and M. Abdel-Wahab, "Analysis of construction trade worker body motions using a wearable and wireless motion sensor network," *Automat. Constr.*, vol. 83, pp. 48–55, 2017.

[112] A. Alwasel and A. Sabet and M. Nahangi and C. T. Haas and E. Abdel-Rahman, "Identifying poses of safe and productive masons using machine learning," *Automat. Constr.*, vol. 84, pp. 345–355, 2017.

[113] G. P. Panebianco, M. C. Bisi, R. Stagni, and S. Fantozzi, "Analysis of the performance of 17 algorithms from a systematic review: Influence of sensor position, analysed variable and computational approach in gait timing estimation from IMU measurements," *Gait Posture*, vol. 66, pp. 76–82, 2018.

[114] Q. Mascret, M. Bielmann, C.-L. Fall, L. J. Bouyer, and B. Gosselin, "Real-time human physical activity recognition with low latency prediction feedback using raw IMU data," in *Proc. IEEE Int. Conf. Eng. Med. Bio. Soc.*, Honolulu, HI, 2018, pp. 239–242.

[115] A. S. Alharthi, S. U. Yunas, and K. B. Ozanyan, "Deep learning for monitoring of human gait: A review," *IEEE Sensors J.*, vol. 19, no. 21, pp. 9575–9591, 2019.

[116] J. Wang, Y. Chen, S. Hao, X. Peng, and L. Hu, "Deep learning for sensor-based activity recognition: A survey," *Pattern Recog. Lett.*, vol. 119, pp. 3–11, 2019.

[117] J. M. Wang, D. J. Fleet, and A. Hertmann, "Gaussian process dynamical models for human motion," *IEEE Trans. Pattern Anal. Machine Intell.*, vol. 30, no. 2, pp. 283–298, 2008.

[118] N. D. Lawrence and J. Quiñonero-Candela, "Local distance preservation in the GP-LVM through back constraints," in *Proc. of 23rd Int. Conf. Machine Learning*, Pittsburgh, PA, 2006, pp. 513–520.

[119] D. Lee, I. Kang, D. D. Molinaro, A. Yu, and A. J. Young, "Real-time user-independent slope prediction using deep learning for modulation of robotic knee exoskeleton assistance," *IEEE Robot. Autom. Lett.*, vol. 6, no. 2, pp. 3995–4000, 2021.

Appendices

Appendix A. Matrices of Manipulator Dynamic Equations

The robotic manipulator is considered by a multi link (rotational) rigid body and the dynamics model is expressed as in 3.10. Here we rewrite it into a more general form as

$$\boldsymbol{M}\ddot{\boldsymbol{q}} + \boldsymbol{D}\dot{\boldsymbol{q}} + \boldsymbol{G} = \boldsymbol{u}, \tag{1}$$

where $\boldsymbol{q} = [\theta_1 \cdots \theta_n]^T$ is the joint angle vector, $\boldsymbol{M}$, $\boldsymbol{D}$, and $\boldsymbol{G}$ are the manipulator's inertia, Coriolis, and gravity matrices, respectively.

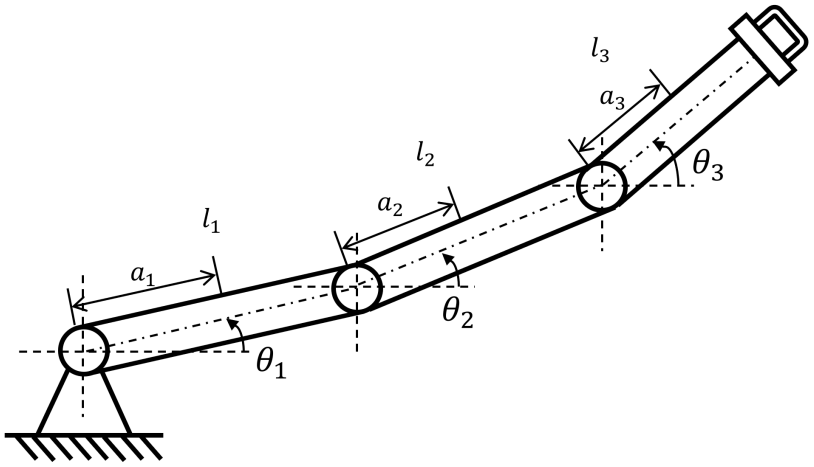

Figure A.1: The schematic of the three links robotic manipulator.

We assume the length of each link are $l_1 \cdots l_n$ and the distance from link to the center of mass are $a_1 \cdots a_n$. The angles of the rotational joints are $\theta_1 \cdots \theta_n$. For example, the three links of the manipulator in the planar motion is shown in 7.2. We can derive the matrices $\boldsymbol{M}$, $\boldsymbol{D}$ and $\boldsymbol{G}$ as follows

$$\boldsymbol{M} = \begin{bmatrix} m_{11} & m_{12} & m_{13} \\ m_{21} & m_{22} & m_{23} \\ m_{31} & m_{32} & m_{33} \end{bmatrix}, \quad \boldsymbol{D} = \begin{bmatrix} d_1 \\ d_2 \\ d_3 \end{bmatrix}, \quad \boldsymbol{G} = \begin{bmatrix} g_1 \\ g_2 \\ g_3 \end{bmatrix}, \tag{2}$$

where each terms in the matrices are listed below

$$\begin{aligned}
m_{11} =& J_1 + J_2 + J_3 + m_1 a_1^2 + m_2(l_1^2 + a_2^2 + 2a_2 l_1 \cos q_2) \\
&+ m_3(l_1^2 + l_2^2 + a_3^2 + 2l_1 l_2 \cos q_2 + 2l_2 a_3 \cos q_3 + 2l_1 a_3 \cos(q_2 + q_3), \\
m_{12} =& J_2 + J_3 + m_2(a_2^2 + a_2 l_1 \cos q_2), \\
&+ m_3(l_2^2 + a_3^2 + l_1 l_2 \cos q_2 + 2l_2 a_3 \cos q_3 + l_1 a_3 \cos(q_2 + q_3)) \\
m_{13} =& J_3 + m_3(a_3^2 + l_2 a_3 \cos q_3 + l_1 a_3 \cos(q_2 + q_3)), \\
m_{22} =& J_2 + J_3 + m_2 a_2^2 + m_3(l_2^2 + a_3^2 + 2l_2 a_3 \cos q_3), \\
m_{23} =& J_3 + m_3(a_3^2 + l_2 a_3 \cos q_3), \\
m_{33} =& J_3 + m_3 a_3^2, \\
d_1 =& - m_2 l_1 a_2(2\dot{q_1} + \dot{q_2})\dot{q_2} \sin q_2 - m_3(l_1 l_2(2\dot{q_1} + \dot{q_2})\dot{q_2} \sin q_2 \\
&+ l_1 a_3(2\dot{q_1} + \dot{q_2} + \dot{q_3})(\dot{q_2} + \dot{q_3}) \sin(q_2 + q_3) + l_2 a_3(2\dot{q_1} + 2\dot{q_2} + \dot{q_3})\dot{q_3} \sin q_3), \\
d_2 =& m_2 l_1 a_2 \dot{q_1}^2 \sin(q_2 + q_3) + m_3(l_1 l_2 \dot{q_1}^2 \sin(q_2 + q_3) \\
&+ l_1 a_3 \dot{q_1}^2 \sin(q_2 + q_3) - l_2 a_3(2\dot{q_1} + 2\dot{q_2} + \dot{q_3})\dot{q_3} \sin q_3), \\
d_3 =& m_3(l_1 a_3 \dot{q_1}^2 \sin(q_2 + q_3) + l_2 a_3(\dot{q_1} + \dot{q_2})^2 \sin q_3), \\
g_1 =& - (m_1 a_1 + m_2 l_1 + m_3 l_1) g \cos q_1 - (m2a_2 + m_3 l_2) g \cos(q_1 + q_2), \\
&- m_3 a_3 g \cos(q_1 + q_2 + q_3) \\
g_2 =& - (m2a_2 + m_3 l_2) g \cos(q_1 + q_2) - m_3 a_3 g \cos(q_1 + q_2 + q_3), \\
g_3 =& - m_3 a_3 g \cos(q_1 + q_2 + q_3).
\end{aligned}$$